THERMAL-MECHANICAL ANALYSIS OF A LOW-ENRICHED URANIUM FOIL BASED ANNULAR TARGET FOR THE PRODUCTION OF MOLYBDENUM-99

A Thesis presented to the Faculty of the Graduate School

University of Missouri

In Partial Fulfillment

Of the Requirements for the Degree

Master of Science

---

by

SRISHARAN GARG GOVINDARAJAN

Dr.Gary Solbrekken, Thesis Supervisor

DECEMBER 2011

The undersigned, appointed by the Dean of the Graduate School, have examined the thesis entitled

THERMAL-MECHANICAL ANALYSIS
OF A LOW-ENRICHED URANIUM FOIL
BASED ANNULAR TARGET FOR THE
PRODUCTION OF MOLYBDENUM-99

Presented by Srisharan Garg Govindarajan

A candidate for the degree of Master of Science

And hereby certify that in their opinion it is worthy of acceptance.

Professor Gary Solbrekken

Professor Yuwen Zhang

Professor Stephen Montgomery-Smith

ACKNOWLEDGEMENTS

I am grateful to my supervisor Dr.Gary Solbrekken for having guided me through this thesis with his patience and knowledge while giving me the independence to work in my own way. I would like to thank my family for their unwavering support and for having made this possible. I would also like to thank Charlie Allen from the Missouri University Research Reactor and my colleagues Kyler Turner, Philip Makarewicz and John Kennedy for offering their perspectives on various issues during the course of this thesis.

TABLE OF CONTENTS

LIST OF FIGURES

LIST OF TABLES

NOMENCLATURE

C Celsius

E modulus of elasticity

GPa Giga Pascal

σ rms roughness

H microhardness

h heat transfer coefficient

K Kelvin

k thermal conductivity

keV kilo electron volt

m meters

P pressure

q'' heat flux

R thermal contact resistance

r radius

T temperature

U overall interference

u_A interference due to heat flow

u_B interference due to contact resistance

u_C initial degree of fit

Greek

α thermal expansion coefficient

σ_r radial stress

σ_θ hoop stress

Δ difference

θ slope of the asperity

Subscripts

cond conduction

conv convection

foil refers to the LEU foil

in inner

out outer

Abbreviations

ANL Argonne national lab

DOE Department of energy

FEA finite element analysis

GTRI global threat reduction initiative

KAERI Korean atomic energy research institute

LEU low enriched uranium

RERTR Reduced enrichment for research and test reactors

ABSTRACT

One of the US department of Energy's global threat reduction initiative goals is to eliminate the use of high-enriched uranium from the production of the radio-isotope Molybdenum-99. One strategy to achieve this goal is to use a target that utilizes a low-enriched uranium (LEU) foil. This thesis considers an annular target, where an LEU foil of open cross section is sandwiched between two concentric aluminum tubes. A recess is cut on the inner tube to hold the LEU foil and facilitate assembly. The target must contain the fission products until it can be opened and the LEU foil removed for further processing. The thermal contact resistance between the LEU foil and the aluminum tube cladding needs to be low enough to ensure that the LEU temperature doesn't exceed the operating temperature specified by the reactor safety case.

The commercial finite element code Abaqus was used to perform a fully coupled thermal stress analysis on the annular target with a recess to analyze the conditions under which the target could potentially fail. A parallel numerical model for an annular target with uniform heating was developed in Abaqus and an analytic model to predict the thermal stresses in a composite structure was derived. This analytic model, along with existing analytic models was used to validate the uniform heating numerical model. The uniform heating model was then used to validate the annular target with a recess. It is found that the magnitude of separation between the foil and the tubes can be controlled by controlling the ratio of heat transfer coefficients between the inner and the outer tube. Also, based on the thickness ratio studies, it is found that the current annular target design is safe at high heat fluxes.

Chapter 1: Introduction

A significant milestone in nuclear medicine was the discovery of artificially produced radio-nuclides by Mary and Pierre Curie in February 1934. They reported the first artificial production of radioactive material, after discovering radioactivity in aluminum foil that was irradiated with a polonium preparation. Their work was built upon earlier discoveries by Wilhelm Konrad Roentgen (X-ray), Marie Curie (radioactive thorium and coining the term "radioactivity ") and Henri Becquerel (radioactive uranium salts). On December 7th 1946, an article published by Seidlin et al (1946) in the Journal of the American Medical Association described the successful application of Iodine-131, a radioisotope, to treat a patient with thyroid cancer metastases. By the 1960s nuclear medicine had gained prominence and the next 20 years involved vigorous research and development of non-invasive medical procedures to diagnose illness and treat patients. Some of the non-invasive medical procedures are single-photon emission computed tomography (SPECT), computed X-ray tomography (CT), positron emission tomography (PET), magnetic resonance imaging (MRI) and X-rays. The non-invasive medical procedures involving nuclear medicine employ the use of radioactive tracers which emit gamma rays from within the body. These tracers are short lived isotopes linked to chemical compounds which permit specific physiological processes to be scrutinized. Positron emission tomography uses radio nuclides that are isotopes with short half-lives such as fluorine-18 (~110 min), carbon-11 (~20 min), nitrogen-13 (~10 min) andoxygen-15 (~2 min). These radio nuclides are either injected into the patient's bloodstream or given orally so that they interact with the compounds normally used by the body such as glucose, water, or ammonia. The positron emitting radionuclide accumulates in the area of concern and emits a positron as it decays. This positron combines with an electron to emit

gamma rays in opposite directions which are picked up by the extremely precise PET cameras. Apart from being helpful in cardiac and brain imaging, the PET has been found to be very accurate in detecting and evaluating cancers. Though a lot of radio nuclides are being used in various medical procedures, Technetium-99m is the most commonly used diagnostic radioactive tracer element. The following section provides a detailed insight into its discovery, development and production.

1.1 Technetium-99m

Technetium-99m, the short lived daughter isotope of Molybdenum-99, is well suited to being used as a radio-active tracer that medical equipment can detect in the human body as it readily emits 140 keV gamma rays and has a short half-life of 6 hours. It was first discovered, as an artificial element, in 1937 by Carlo Perrier (an Italian mineralogist) and Emilio Gino Segre (a Nobel laureate in physics) to fill space number 43 in the Periodic Table. Consequently generator systems were developed in the 1960s to produce technetium-99m, with Brookhaven National Lab producing the first molybdenum-99/technetium-99m generator. Due to its 6 hour half-life, technetium-99m cannot be transported over large distances. Hence the molybdenum-99 is directly shipped to hospitals and radio-pharmacies in these technetium generators which are radiation shielded. Molybdenum-99 decays to technetium-99m by emitting a beta particle and an antineutrino. The decay process resulting in technetium-99m is:

$$^{99}\mathrm{Mo} \rightarrow {}^{99m}\mathrm{Tc} + e^{-} + \nu_e \qquad (1)$$

where the e^- denotes the beta particle emitted from the nucleus and ν_e represents the electron antineutrino. The column chromatography technique is used by most molybdenum-99/technetium-99m generators to separate the isotopes. During this process, ^{99}Mo in the form of

molybdate, MoO_4^{2-} is adsorbed onto acid alumina (Al_2O_3). When the ^{99}Mo decays, it forms pertechnetate TcO_4^-, which is less tightly bound to the alumina due to its single charge. Application of salt water over^{99}Mocolumn removes the soluble ^{99m}Tc, resulting in a saline solution containing the ^{99m}Tc as the dissolved sodium salt of the pertechnetate. Further, the technetium-99m undergoes isomeric transition to yield technetium-99 and emits gamma rays.

$$^{99m}Tc \rightarrow {}^{99}Tc + \gamma \qquad (2)$$

When a patient has been injected with technetium-99m, the above reaction takes place inside the body and the emission of the gamma rays is picked up by the gamma camera thus paving the way for accurate diagnosis of ailments.

1.2 Target Development and Purpose of Work

Molybdenum-99 production begins with neutron irradiation of fissionable U-235 contained in HEU or LEU targets in a nuclear reactor. This initiates a nuclear fission reaction which produces a large amount of heat and fission products. The purpose of the target is to contain the fission products by withstanding the thermal stresses induced in the target material due to high temperatures and to effectively dissipate the heat to the reactor coolant pool.

Currently the molybdenum-99 in the United States primarily comes from foreign reactors in Canada (MDS-Nordion) and Netherlands (Covidien).Molybdenum-99 is an important radio isotope from a medical perspective as it is the parent isotope of the widely used radioactive tracer technetium-99m. When the reactors that supply molybdenum-99 to the United States were shutdown in 2006 for routine maintenance there was widespread shortage of technetium-99m.

All the molybdenum-99 currently being produced is from HEU (greater than 20 % of U-235 or U-233) using a powder dispersion target. In this process a mixture of HEU powder and aluminum powder is heated and compressed between two plates to form a monolithic structure that ensures no gas gaps exist between the uranium and the aluminum. To recover the molybdenum-99 the entire plate is dissolved, resulting in expensive liquid waste. Due to the high concentration of uranium in HEU, it can be used to make nuclear weapons apart from being beneficial to high volume production of molybdenum-99.

In accordance with the US Department of Energy's (DOE) Global Threat Reduction Initiative (GTRI), all the Mo-99 production must switch from using HEU to LEU (low enriched uranium). While this switch from HEU to LEU will increase safety, it is also the motivating factor behind the switch from the dispersion target to the foil target. Since LEU has only a fraction of the uranium-235 content that HEU has per unit weight, more LEU is required to achieve the same output of molybdenum-99. Hence, if LEU were to be used in a dispersion target, the volume of the target would increase dramatically. But, by switching to a uranium foil and eliminating the aluminum used in the dispersion target, the mean uranium-235 density of the foil target is much higher than that of a comparable dispersion target. As a result, the volume and the amount of uranium-235 in an LEU foil target will approximately match the volume and the amount of uranium-235 in a HEU dispersion target. Specifically, the dispersion targets from Petten in Netherlands use 5.2 g uranium and an enrichment of 91% for a total of 4.7 g of uranium-235 (Allen et al., 2007). The foil targets designed by Argonne National Laboratory consist of 20 g of LEU, enriched to 19.8% (Allen et al., 2007). This means that the foil target contains about 4 g uranium-235, which is about 14.9% less than the 4.7 g present in the dispersion targets.

The alternative to HEU is to use a LEU foil based target, where the LEU foil is wrapped in a nickel foil and sandwiched between two concentric aluminum tubes. The role of the nickel foil is to act as a recoil barrier and prevent any bonding between the aluminum cladding and the LEU foil during irradiation. After irradiation the aluminum cladding is cut open to retrieve the LEU foil alone, which is then dissolved to retrieve the molybdenum-99. This is known as the modified process and it reduces the amount of liquid waste. The composite structure of the target brings into question the thermal contact resistance at the interface of the uranium, nickel and aluminum cladding layers. The thermal contact resistance at the interface of the LEU foil and the aluminum tube cladding must be low enough to ensure that the LEU temperature doesn't exceed the operating temperature specified by the reactor safety case.

Until now there has been no documented study on LEU foil based annular targets to support the fact that they would perform well during irradiation without compromising on the reactor safety. The target can fail if the LEU foil begins to overheat due to an increase in the interfacial contact resistance or if the stresses induced in the material due to temperature gradients exceed the ultimate tensile strength of the material. Hence, the objective of this thesis is to address the thermal mechanical aspects of the LEU foil based annular target under various operating conditions and prove that these targets can be safely irradiated. The results from this study can be used as a reference tool for future analysis of LEU foil based annular targets.

Presented in this thesis is a numerical analysis, using the commercial finite element code Abaqus FEA , to address the thermal-mechanical behavior of the LEU foil based annular target under various conditions and provide an envelope under which the target could potentially fail. Analytic models are used to validate the numerical results and an experimental method to further validate these results has been identified.

Chapter 2: Literature Review

This chapter consists of three sections that provide a literature review of past research in the field of thermal contact resistance, LEU foil based target development and thermal stresses in cylinders. These sections are independent of each other and the idea is to provide an insight into previous literature on these important aspects which will be addressed in this thesis.

2.1 Thermal Contact Resistance

A proper understanding of the interface integrity is an important aspect in high heat flux applications as the presence of surface irregularities and its improper evaluation will result in overheating and subsequent failure of components. Typically in thermal contact resistance studies involving flat joints the contact pressure is known and can be taken as the independent variable. In cylindrical joints, the flow of heat causes the expansion of the tubes which results in the contact pressure (Madhusudhana, 1996). Hence the heat flux is the independent variable in cylindrical joints.

Madhusudhana and Fletcher (1981) conducted tests on cylindrical joints with varying interface heat fluxes. They showed that the thermal contact resistance is dependent upon the initial interference, the differential expansion due to temperature drop at the interface and the differential expansion due to the temperature gradients. Also, due to the contact resistance being dependent on the initial interference, their results illustrate that joints with an interference fit will have negligible thermal contact resistance. This is true as with an interference fit , the interface temperature discontinuity will be negligible.

A review of thermal contact conductance studies was provided by Madhusudhana et.al (1990). They report that the there is a dearth of literature based on contact conductance studies of

cylindrical joints and often the effects of differential expansion are neglected assuming the thermal contact resistance to be constant.

Experiments on composite cylinders were performed by Hsu and Tam (1979). They varied the heat flux , microscopic surface properties only on one side of the interface and compared their results with those based on the modified flat contact models of Ross and Stoute (1962). They found these experimental results to be much lower than the calculated values and attributed it to the increase in micro-contact area due to the lateral expansion of the flat contacts and thermally induced strain at the interface.

An iterative procedure, based on a plane stress and interference fit assumption, to predict the contact conductance of cylindrical joints based on flat contact conductance models was provided by Lemczyk et.al (1987). Their iterative procedure takes into account the surface roughness, microhardness and the contact pressure at the interface. The thermal contact conductance is presented as a function of the contact pressure, thus recommending that accounting for the difference between the circumferential and axial roughness is important. Their model was in good agreement with that of Hsu and Tam (1976) and the modified flat contact models of Ross and Stoute (1962).

A study on the coaxial cylindrical casings in a vacuum environment was performed by Novikov, et al. (1972), taking into account the mechanical and thermo physical properties of the tubes. The investigators report a dependency between the contact pressure, thermal load, initial interference of the tubes and the ratio of thermal expansion coefficients of the tubes without considering the microscopic or macroscopic surface irregularities. They concluded that for a case of radially outward heat flow, if the thermal expansion coefficient of the inner tube is lesser than

that of the outer tube then the thermal contact resistance at the interface will increase due to a decrease in the interfacial contact pressure.

A laser flash technique along with a Gaussian parameter estimation procedure was employed by Milosevic et.al (2002) to estimate the thermal contact resistance at the interface of a double layer sample. They provide the analysis of sensitivity coefficients for each parameter of the double-layer sample which can be extended for use in designing experiments. Based on their numerical simulations they concluded that their method could estimate the thermal contact resistance between the layers with high accuracy if any one of the sample materials is a good conductor of heat or if a thin layer assumption is used. They also found that the energy absorbed by the sample from the laser pulse can be estimated with ease if a high signal to noise ratio exists.

Madhusudhana and Fletcher (1983) obtained power law correlations based on previous experimental work, to predict the solid spot thermal conductance at the interface of Zircaloy-2 and Uranium Dioxide. They concluded that more work is required to determine the effect of mean junction temperature on the thermal contact conductance and surface parameters other than the roughness must be accounted for future analysis.

Turner et al (Turner, 2009) identified an experimental methodology to predict the thermal contact resistance based on the interfacial stresses in a pair of concentric aluminum tubes. They showed that for a couple of aluminum tubes in perfect contact, external heating of the outer tube would result in tensile stresses being generated on both the tubes. This opens up a gap between the tubes and increases the thermal contact resistance. Internal heating of the inner tube would result in compressive stresses being generated on the tubes, thus reducing the thermal contact

resistance. Thus by controlling the direction of heat flow, contact is either reinforced or relaxed due to the compressive and tensile stresses respectively.

2.2 Target Design and Development

LEU foil based annular target design and developmental studies were carried out by Conner et al (Conner, 1999) from the Argonne National Lab. Their design consisted of an LEU foil sandwiched between concentric cylindrical tubes. The LEU foil is wrapped around the inner cylindrical tube with a recess. Their analysis was focused on developing a cost effective annular target design that would minimize the thermal contact resistance between the LEU foil and the target tubes. They performed thermal cycling tests on the assembled annular targets and confirmed that these targets would perform well during irradiation.

The above mentioned design concept developed by Conner et al (Conner, 1999) was successfully demonstrated by irradiating the targets at BATAN in Indonesia at 15 MW reactor power for 120 hours (Mutalib,1999). They reported no heat transfer problems and good overall irradiation performance of the targets. During disassembly the targets were easily removed from the irradiation jigs and this proved that no significant mechanical distortions existed during irradiation. Based on the disassembly they concluded that the nickel fission recoil barriers perform the best while aluminum and zirconium as target tubes work well.

Aareva-Cerca evaluated the thermal-mechanical behavior of the LEU foil based annular target developed by Conner et.al. Their thermal analysis was carried out using the numeric code CFX and they used experiments to determine the thermal contact resistance (Yeoh, 2004). However they considered a perfectly flat LEU foil and did not account for the macroscopic and

microscopic variations on the foil surface which is important in thermal contact resistance prediction.

Thermal hydraulic and neutronic analysis was performed by Mushtaq et al (2008) on LEU foil based annular targets for the production of molybdenum-99 at the Pakistan research reactor-1 (PARR-1). They reported that the reactor safety will not be compromised in adopting the proposed annular target and holder designs for the molybdenum-99 production.

Mushtaq et al (2009) performed neutronic and thermal hydraulic analysis for the production of molybdenum-99 at the Pakistan research reactor-1 (PARR-1) using LEU foil based flat plate targets. Their analysis demonstrated adequate safety margins and proved that LEU foil based flat plate targets can be safely irradiated.

Turner et al (2010) performed studies on LEU foil based flat plate targets by varying the boundary conditions applied to the aluminum plates. The focus of their analysis was to evaluate the impact of changing boundary conditions on the thermal mechanical behavior of these plates. They reported that the variation of stresses and strains induced in the plates was related to the manner in which the plate was constrained. They also showed that the magnitude of deflection through the thickness of the plate was greatest when the plate was fully constrained as opposed to being partially constrained with free edges.

2.3 Thermal Stresses in Cylinders

Poritsky (1934) studied the effect of thermal stresses in sealed cylinders and the effect of viscous flow during the annealing process. The author used an elastic assumption to derive the thermal stress equations for long sealed cylinders with varying coefficient of thermal expansion

values and concluded that the optical retardation due to the existing thermal stress distribution depends on the axial stress alone.

Matsumura et.al provides an analytical approach to investigate the effect of variable coefficient of thermal expansion and modulus of elasticity on the thermal stress in a long hollow cylinder. They considered the cylindrical wall to be composed of a number of thin coaxial cylinders and determined the radial, tangential and axial stresses by assuming that the coefficient of thermal expansion and the elastic modulus in any one layer to be a constant. To arrive at an exact solution they considered an infinite number of layers.

The effect of a time dependent temperature boundary condition on the thermal stresses in an infinitely long hollow cylinder was investigated by Yang et al (2001).They used a Laplace transform to obtain the general governing equations in the transformation domain while the time dependent temperature increments and the stresses in the real domain were numerically represented. Based on their investigations they reported that the thermo mechanical coupling parameter would lead to a lagging effect in the stress and temperature distributions.

Jane et al (1999) considered the thermo elasticity of multilayered cylinders with traction free boundaries and used a matrix similarity transformation along with an inverse Laplace transform to obtain the solution for the temperature and thermal stresses in a transient state. They also report that their computational method can be used to perform a thermo-mechanical analysis of multilayered composite cylinders with non-homogeneous materials.

A steady state heat transfer analysis of pre-stressed duplex tubes was performed by Srinivasan and France (1985). The motivation behind their study was the erratic performance in the steam generator of an experimental nuclear reactor. Using analytical models they showed that

low pre-stresses at the interface of the duplex tubes would result in non-unique solutions. They reasoned that the low pre-stresses were caused due to a non-contact region, which resulted in separation of the tubes and hence an increase in the heat flux and temperatures.

Swindeman (1962) based on his theoretical and practical considerations of the thermal stresses in beryllium oxide cylinders suggested that the appropriate experimental approach should involve external heating of the cylinder. This is an acceptable approach since the internal heating of a cylinder will result in compressive stresses being generated in the tube, thus putting it in an overly optimistic state.

Zimmerman and Lutz (1999) provided an exact solution for the thermal stresses developed in a functionally graded cylinder based on uniform heating and the elastic modulus and the thermal expansion coefficient as a function of the radius of the cylinder. Their analysis helped them conclude that the radial and tangential stresses are maximum at the center of the tube and the volumetric average of the thermal expansion coefficient to be representative of the effective thermal expansion coefficient.

Xue et al (2006) used a 3-D finite element method to study the thermal stresses in sandwich structures with reinforcement. They used a theoretical result to validate their analysis and report that the presence of reinforcement will induce significant transverse thermal stresses due to the mismatch in thermal expansion coefficients of different materials. While this is a drawback, the reinforcement can be used to reduce the in-plane stresses.

Barber et al (1980) used a one dimensional model to describe the existence of a non-unique solution due to thermo elastic contact conditions. They used a perturbation method to investigate the stability of a variety of steady state solutions and expressed the results in terms of

an energy function. However they do not provide the reason behind using such a function due to the non-conservative nature of the system.

Comninou (1980) showed that when two semi-infinite solids in contact exchange heat through conduction, local separation can occur if heat flows into a higher distortivitymaterial. They attributed the lack of uniqueness to the non-existence of heat transfer in the separation zones and no resistance being offered to the flow of heat in the solid to solid contact regions. However they were unable to validate these effects due to the general complexity of their mathematical model.

Having presented the past literature on the thermal contact conductance ,target development and thermal stresses in cylinders, the following chapter will dwell more on the design concepts that are important to this thesis.

Chapter 3: Target Design Techniques

3.1 Plate Target Approach

A plate target analysis was successfully completed by Turner et.al (Turner,2009).Their design consisted of a nickel recoil barrier wrapped around a LEU foil, placed between two aluminum plates and pressed together .The edges were assumed to be welded to provide a completely sealed environment for the fission products. From a mechanical standpoint, the edge welds prevent the plate from moving apart from one another. They reported pillowing of the plates, the magnitude of which depends on the boundary condition applied to the edges of the plates and the amount of heat dissipated through the aluminum cladding. The magnitude of plate deflection is in the micro meter range and may be tolerable. Their analysis consisted of analytical and numerical models.

3.2 Annular Target Approach

The annular target geometry primarily consists of two concentric aluminum tubes within which an LEU foil of open cross section is sandwiched by wrapping thin layers of aluminum or nickel around it. The nickel acts as a fission recoil barrier to prevent the LEU foil from bonding with the aluminum cladding during irradiation. To facilitate easy assembly of the foil on the inner tube, a recess is cut in the inner tube. The ends of the cylinder are welded together to ensure that the fission components are contained inside the assembled target. The composite structure of the target requires that the thermal contact resistance at the LEU foil and cladding interface be low enough. For the flow of heat between surfaces in contact to be continuous, the resistance offered to it should be minimum. Due to manufacturing limitations not all surfaces are

machined to be perfectly smooth and there exists macroscopic and microscopic irregularities on the surfaces. These surface irregularities result in solid spots and air gaps being formed at the interface of the bodies in contact. When heat flows through the joint formed by the surfaces in contact, it tends to favor the solid contact spots as they are regions of higher conductance (since the effective conductivity of the solid will be much greater than that of the air gap). As a result, the heat flow lines begin to cluster in these regions and there exists a constriction to the flow of heat across the interface. This resistance to heat flow manifests itself as a temperature drop at the interface. This phenomenon is illustrated in Figure 1.

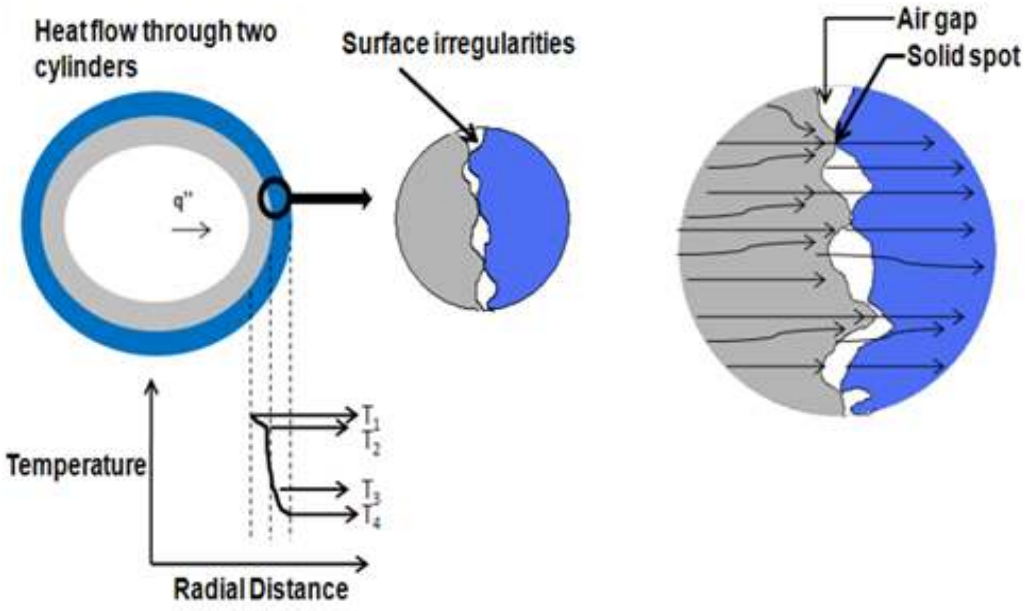

Figure 1. Heat Flow through a joint and temperature drop at the interface

The thermal contact conductance is the reciprocal of thermal contact resistance and is defined as the ratio of the heat flux to the temperature drop at the joint interface due to imperfections.

Mathematically it is given by

$$h = \frac{q''}{\Delta T} \tag{3}$$

where h is the thermal contact conductance,q'' represents the heat flux per unit area leaving the surface and ΔT is the temperature drop at the interface.

Typically the heat transfer through a joint consists of conduction through the contact spots or the solid spots, conduction through the interstitial medium and radiation. Since the gap thickness is usually very small (of the order of μm) the convection effects are not considered and the radiation effects can be neglected if the joint temperature is below 300˚C (Madhusudhana, 1996). Thus, the total conductance (h) can be obtained by solving the solid spot conductance (h_{solid}) and the gas gap conductance (h_{gap}) in a parallel resistance network. The contribution from the gap conductance is usually negligible when compared to the conductance through the solid spots. However, the gap conductance must be taken into account if the interface medium is a good conductor or the bodies in contact are made up of materials that are relatively poor conductors of heat (e.g. Stainless steel). Though a high value of thermal contact conductance is desirable in nuclear reactors, gas turbine blades there exist applications involving storing and transportation of cryogenic fluids (Mikesell,1956), thermal isolation of space craft components (Fletcher, 1973) that require a low value of thermal conductance or higher thermal resistance. In the case of nuclear reactors, a higher thermal conductance is desirable to effectively transfer the heat to the coolant thus preventing overheating which could be potentially catastrophic.

During irradiation the LEU fission generates heat that needs to be dissipated to the reactor coolant pool. The generated heat increases the target temperature and the increase in temperature causes thermal expansion. Since the LEU and the aluminum have different thermal

expansion coefficients, the magnitude of thermal expansion will differ. This thermal expansion mismatch causes pillowing and stresses in the target.

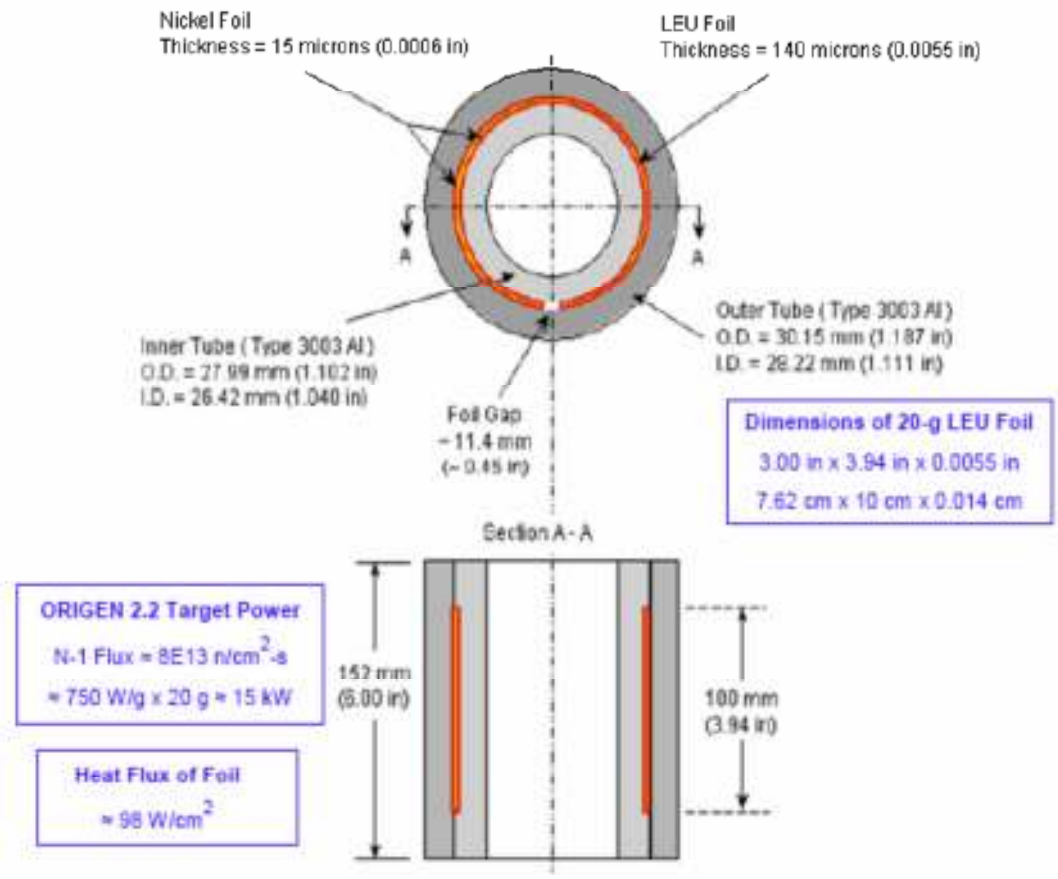

Figure 2. Dimensions of the ANL annular target (Solbrekken, 2008)

After the target is irradiated the aluminum cladding, the sandwiched foil are mechanically separated and the LEU foil is chemically processed. The separation of the LEU from the cladding before processing reduces the mass of the material to be chemically dissolved in alkaline or acidic solutions. The advantage of using an annular target is to improve the structural integrity of the target and the heat transfer rate. The LEU foils to be used have been produced by

the Korean Atomic Energy Research Institute (KAERI, South Korea) using the casting method (where the metal is melted and poured into a mold) and by Argonne National Lab using the hot and cold rolling technique.

In the hot rolling process the metal is heated above its re-crystallization temperature and the foil is then rolled to form sheets while in the cold rolling process the crystalline structure of the foil is retained and the process is carried out at room temperature .The drawback of using the KAERI foils is that they have a lot of surface irregularities and waviness. These microscopic and macroscopic irregularities will make it difficult to justify the use of these targets as a significant amount of surface irregularities will affect the heat transfer rates due to an increase in the thermal contact resistance at the interfaces.

The cold rolling technique used by the Argonne National Lab, though an expensive and labor intensive method can eliminate the surface irregularities. The annular target design developed by Argonne National Lab through the RERTR program (Solbrekken, 2008) is illustrated in Figure 2. Turner et.al (Turner, 2011) showed that the Argonne National Lab annular target is reliable relative to the potential of a gap opening during irradiation and that the interference can be managed by controlling the surface heat transfer coefficients of the inner and outer tubes.

Chapter 4: Annular Target Numerical Modeling

The commercial finite element code Abaqus FEA (formerly Abaqus), version 6.10, was used to perform a thermal-mechanical analysis on the annular foil based target. Originally released in the year 1978, Abaqus FEA is a set of software applications meant for finite element analysis and computer aided engineering. A numerical simulation in Abaqus FEA typically consists of 3 separate stages namely the pre-processing stage, simulation evaluation stage and the post processing stage. The pre-processing stage involves creation of an input file which contains all the constraints under which the model is to be numerically evaluated. In the second stage the numerical analysis is evaluated based on the constraints specified in the pre-processing stage or the Abaqus FEA input file. The post-processing stage involves visualizing the results and extracting data.

4.1 Numerical Model Setup

The annular target was modeled as a 2-D plane strain problem that consists of a low enriched uranium foil of open cross section sandwiched between two aluminum tubes (Al-6061 T6). The residual stresses from the assembly of the target were not considered in the numerical model. While the outer aluminum tube has a uniform circular cross section, the inner tube has a recess cut on its surface (Fig. 3), to a depth equal to the foil thickness, to accommodate the LEU foil. This LEU foil generates heat when irradiated and coolant flows through the inner tube and along the outer tube. The physical configuration of the annular target in a reactor with coolant flow is illustrated in Fig 4 (Scott, 2009). Since the current analysis predominantly involves the thermal-mechanical response of the annular target under consideration, the modeling strategy

explained in this section will focus more on the development of a coupled thermal-mechanical analysis in Abaqus FEA.

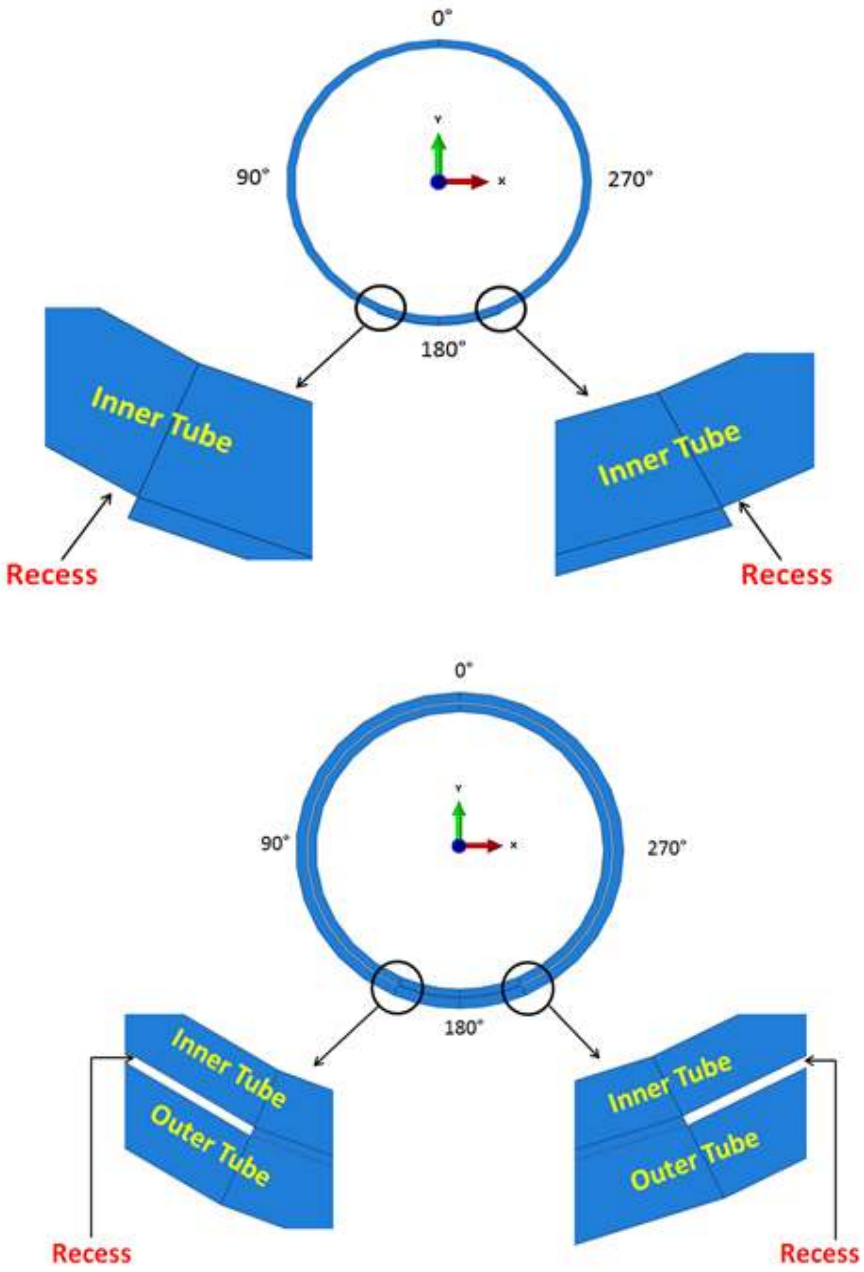

Figure 3. Numerical model setup showing the inner tube and outer tube assembly

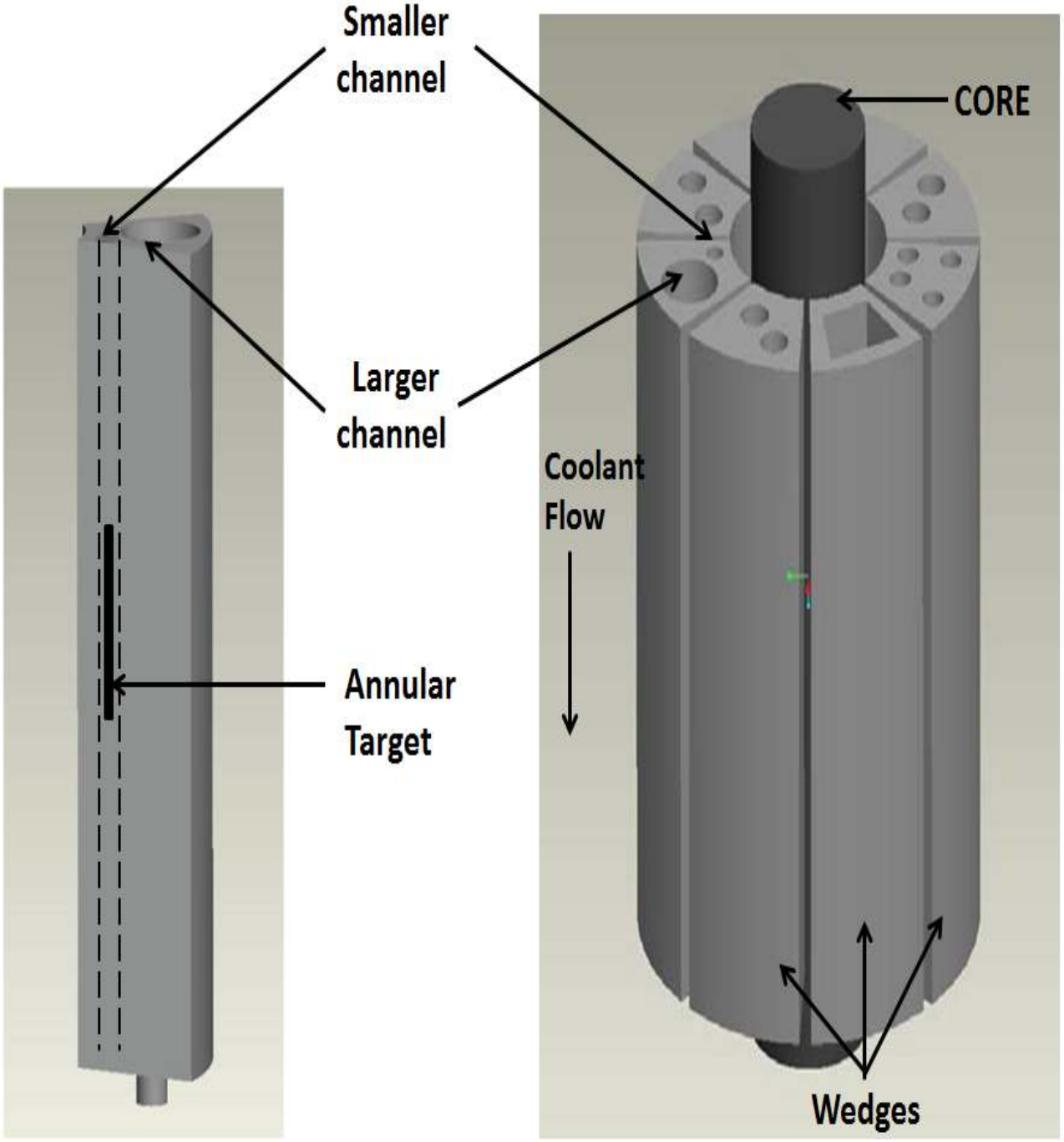

Figure 4. Graphic of the reactor core and annular target location (Scott, 2009)

The basic steps involved in creating and setting up the model in Abaqus FEA will be explained here briefly while a complete thermal-stress analysis tutorial can be found in the appendix. The first step involves creating the individual parts: the inner tube, foil and the outer tube. Once this has been done, the material properties (Table 1) of the parts have to be defined followed by assigning these material properties to the created parts by using sections and sectional assignments.

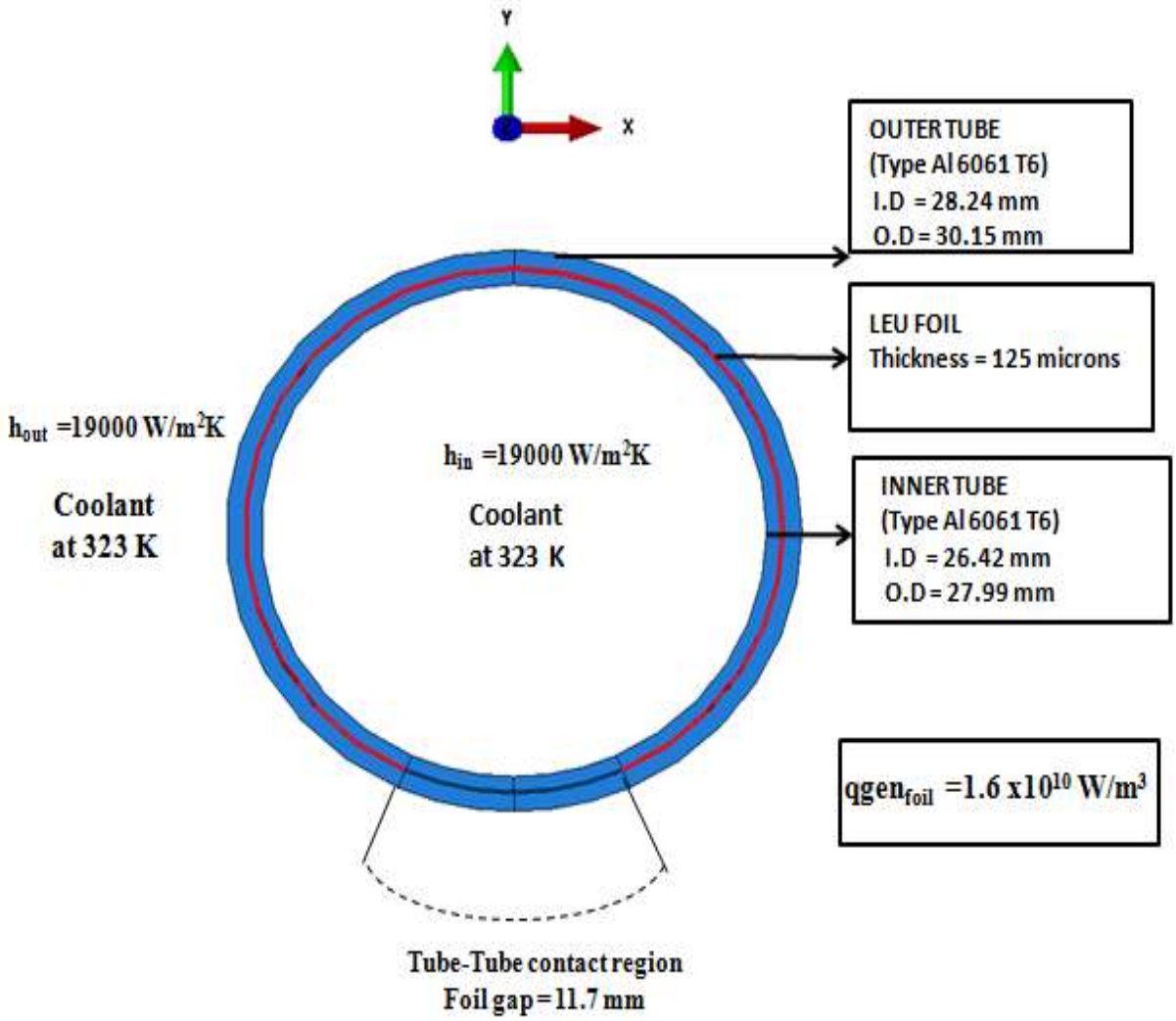

Figure 5. Numerical model setup in Abaqus FEA

Table 1. Material properties of the cladding and foil.

Material Property	Aluminum 6061-T6	Uranium
Modulus of Elasticity, E (GPa)	69	208
Poisson's ratio , v	0.33	0.23
Thermal Expansion Coefficient ,α (K^{-1})	2.34×10^{-5}	1.39×10^{-5}
Thermal Conductivity, K (W/mK)	167	27.5

Once the parts have been created using the dimensions specified in Fig 5, they need to be assembled together. The assembly module in Abaqus FEA provides various options, constraints under which the model can be assembled. The easiest assembly procedure is the 'translation' option which can be found under the 'Instance' toolbar. It requires the user to input the start point for translation, which is usually on the movable part and the end point for the translation, which is on the immovable part. The annular target assembly procedure is outlined in Fig 6. The first step is to select the inner tube 'instance'. After this, the LEU foil is assembled on the recess cut in the inner tube. The final step is to assemble the outer tube over the inner tube and the foil. Once the model has been assembled, it is always good to check if the parts are located in the position they are supposed to be in. Abaqus FEA carries out the simulation based on analysis steps. Hence it is required to create the appropriate analysis step based on the type of analysis to be carried out (e.g. heat transfer, static, fully coupled thermal stress).

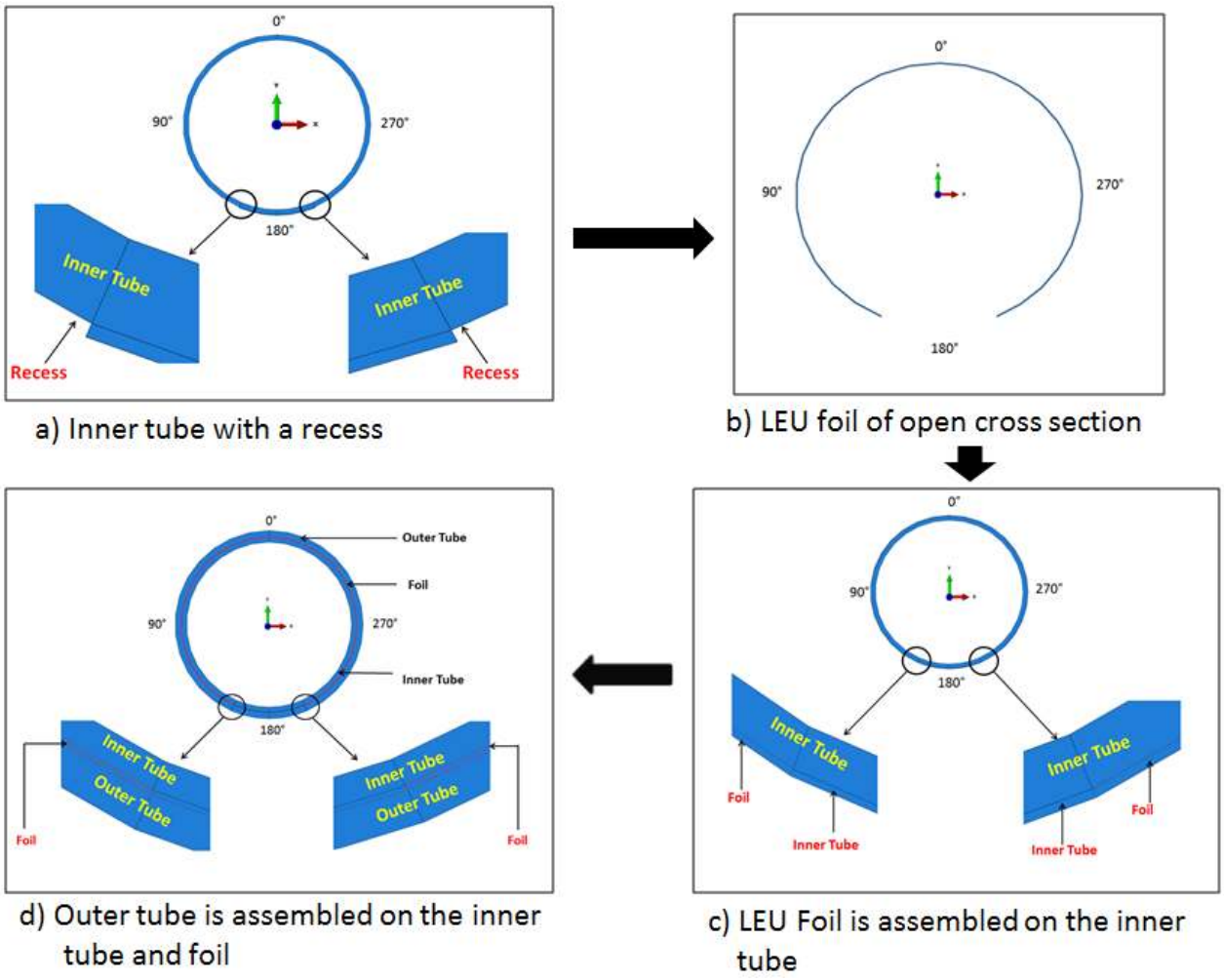

Figure 6. Annular target assembly procedure in Abaqus FEA

To numerically evaluate the assembly in Abaqus FEA, the contact conditions have to be enforced through the interaction properties. The thermal and mechanical interactions properties are specified in this fully coupled thermal stress analysis. The mechanical contact conditions allow the user to specify the normal behavior and tangential behavior of the surfaces that come into contact. A 'frictionless' tangential behavior is chosen while the normal behavior is based on a 'hard contact' formulation where the constraints are enforced by the Lagrange multiplier

method. The option of surface separation after contact is selected as this closely represents the behavior in the target during irradiation. The thermal contact conditions require the specification of the thermal conductance, thermal radiation or heat generation due to frictional effects. For this analysis the thermal conductance option is selected and a high value of thermal conductance (10^9 W/m^{2}K) is specified for perfect contact (zero gap).

The thermal stress analysis can be performed in Abaqus FEA in a couple of ways – a fully coupled thermal stress analysis and a sequentially coupled thermal stress analysis. In a fully coupled thermal stress analysis the thermal and the mechanical parts are solved simultaneously. This procedure can be used when the user expects the thermal behavior to affect the mechanical behavior and vice versa. On the other hand a sequentially coupled thermal stress analysis is used when the thermal part influences the mechanical solution and there is no reverse dependence. To execute a sequentially coupled thermal stress analysis, the thermal part is solved first and its values are fed into the stress model after replacing the 'heat transfer' step with a 'static-general' step and using the corresponding meshing elements.

The specification of mechanical boundary conditions plays an important role in the behavior of the model. Since the LEU foil based annular target under consideration is symmetric about the x-axis, an x-symmetric boundary condition is applied to the nodes as illustrated in Fig 7. The x-symmetric boundary condition restricts the translation in the horizontal direction and does not allow any tangential rotation as well. Hence by making use of the geometry of the model, the boundary conditions are enforced without significantly affect the setup. From a thermal standpoint, it is required to specify the heat transfer coefficient at the inner and the outer regions to effectively dissipate the heat generated by the LEU foil. To simulate water cooling in the reactor, a heat transfer coefficient of 19000 W/m^2 K was used on the inner and outer regions.

Subsequently parametric studies were performed by varying the heat transfer coefficient ratios, the tube thickness ratios and the heat generation rate of the LEU foil and are presented in chapter 7. This would provide an insight into the behavior of the target under various conditions and could serve as a useful reference tool for future analysis.

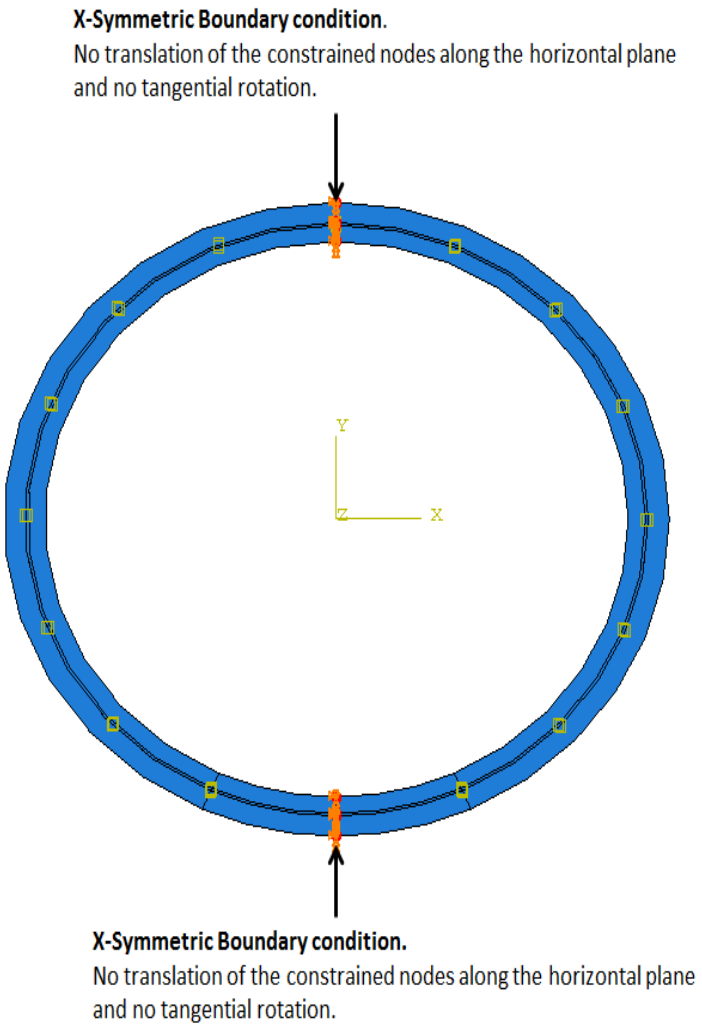

Figure 7. Boundary conditions for the 2-D non-uniform heating numerical model.

The loading source for this problem is the heat generation of the foil. This value can be specified under the 'Load' module. In any finite element analysis, the choice of the elements that make up the mesh plays a significant role in the solution convergence process. Abaqus FEA has a particular set of elements for its different analysis steps and care should be taken to select the appropriate element. The nature of the element chosen (i.e. linear, quadratic or tetrahedral) entirely depends on the analysis type, geometry of the parts that make up the assembly.

Table 2. Mesh configuration for the numerical analysis in Abaqus FEA

Part	Element Type	Thickness elements	Number of Nodes	Number of Elements
Inner Tube	Quadratic reduced integration (CPE8RT)	10	12800	4000
Foil	Quadratic reduced integration (CPE8RT)	10	12800	4000
Outer Tube	Quadratic reduced integration (CPE8RT)	10	12800	4000

Generally for problems involving contact it is recommended to use a fine mesh of linear elements. However, a huge number of linear elements are required to closely model curved surfaces. Hence in this analysis the quadratic reduced integration elements of type CPE8RT were used. The use of these quadratic elements also helps to model the edges on curved surfaces accurately. A lot can be written about the choice of element types in Abaqus FEA, but have only been briefly mentioned in this section as it covers the broader picture of the model setup. The

criteria for element selection and more on meshing elements can be found in the appendix. Table 2 shows the mesh configuration used in the numerical analysis.

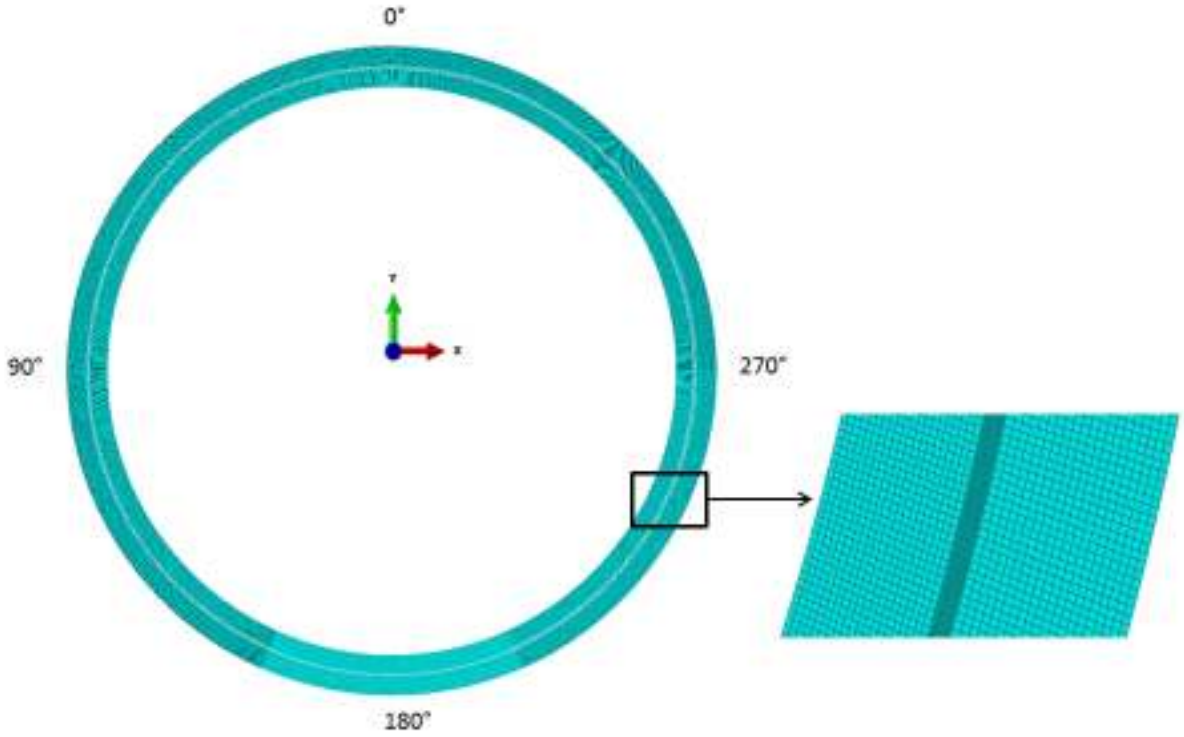

Figure 8. Finite element mesh used in the numerical model

Due to the open cross of the foil only a portion of the tubes are uniformly heated and the tube to tube contact region will not receive as much heat as compared to the uniformly heated regions. As a result a cold spot will be formed in this region due to the existence of comparatively lower temperature gradients. In essence, the LEU foil based annular target modeled with an open cross section foil and a recess on the inner tube is a case of non-uniform heating. The finite element mesh used in the numerical model is shown in Fig 8. A 'matched'

mesh was used to facilitate convergence and easier extraction of radial data across the annular target assembly.

4.2 Need for a Uniform Heating Model

The unique geometry of the inner tube, open cross section of the foil and the non-uniform heating as a result, means that a complex analytic model will be required to validate the non-uniform heating results. Simple analytical models can be developed to validate a uniform heating model where the foil is modeled as a completely circular tube as illustrated in Fig 9.

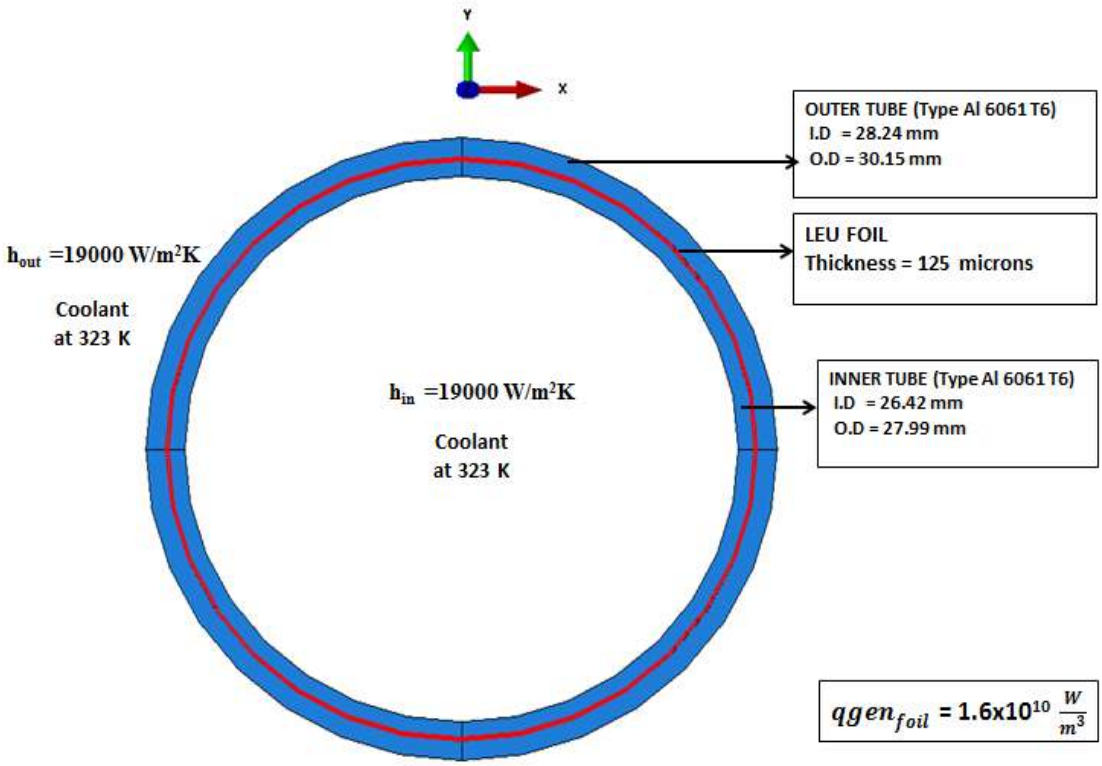

Figure 9. 2-D Uniform heating model of the LEU foil based annular target

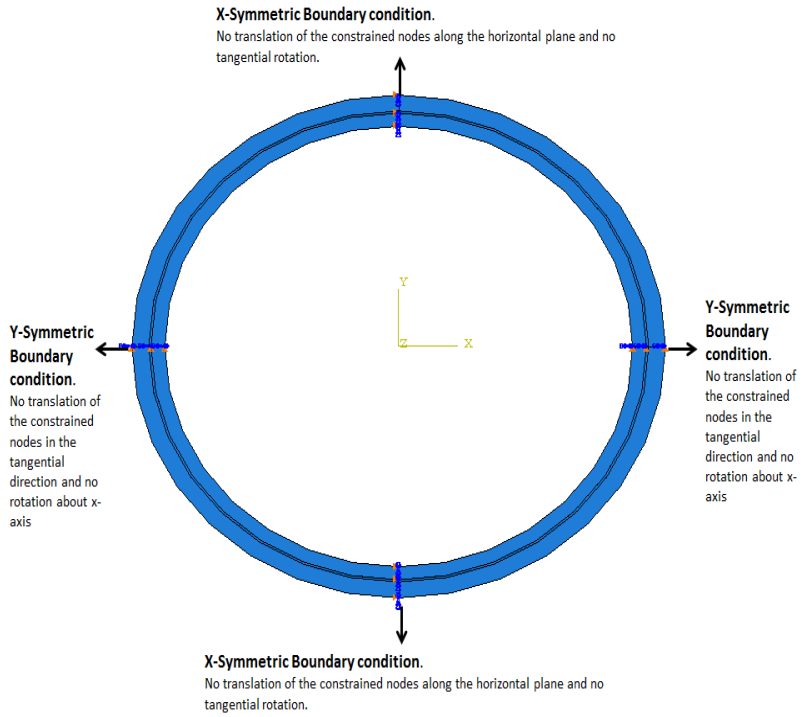

Figure 10. Boundary conditions for the 2-D uniform heating numerical model.

Once the uniform heating model has been validated, it can be used to validate the non-uniform heating model by comparing the relative order of magnitudes in the uniformly heated portion of the non-uniform heating model (i.e. in the uniformly heated portion of the annular target with a recess).In addition to the x-symmetric boundary condition, a y-symmetric boundary condition can be applied to the nodes as shown in Figure 10.A similar mesh is used on the uniform and non-uniform heating models to facilitate easier comparison of results at the nodal locations. Except for the foil being modeled as a full circular cylinder and the non-existence of a recess on the inner tube, the model is setup for analysis in a similar way as explained in section 4.1. Having developed a uniform heating model, it is necessary to support it with an analytic model to lend credibility to the results. The following section details the analytic models used.

Chapter 5 – Analytical Modeling

Since the foil generates heat, the heat fluxes entering the inner and outer tubes will differ due to different surface areas and heat transfer coefficients. Hence an analytic model using a simple thermal resistance network (Figure 11) was developed to determine the uranium temperature and the individual heat flow rates q''_{in} and q''_{out} into the inner and outer tubes respectively. The uranium temperature can be determined by solving the thermal resistance network in Fig 11. The effective resistance in series in the radially outward direction is given by

$$R_{eff\ out} = R_{cond\ out} + R_{conv\ out} \tag{4}$$

The effective resistance in series for radially inward heat flow is given by

$$R_{eff\ in} = R_{cond\ in} + R_{conv\ in} \tag{5}$$

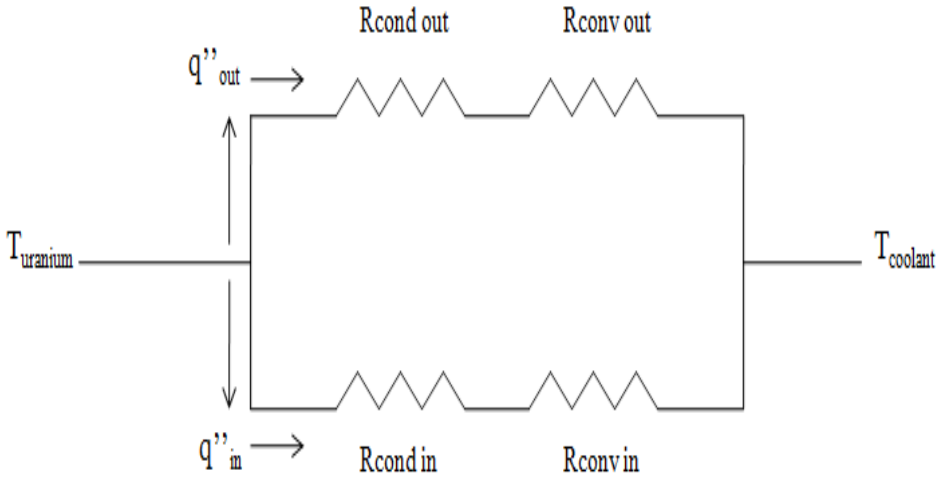

Figure 11. Thermal resistance network for the annular target.

R_{effout} and R_{effin} form a parallel resistance network and the resulting effective parallel resistance is given by

$$R_{eff} = \left(\frac{1}{R_{eff\,out}} + \frac{1}{R_{eff\,in}}\right)^{-1} \quad (6)$$

Knowledge of the heat generation rate of the foil and its dimensions, the heat transfer rate 'q' can be calculated. Since the coolant temperature, effective resistance and the heat transfer rate 'q' are known, the uranium temperature can be calculated using the formula

$$R_{eff} = \frac{T_{uranium} - T_{coolant}}{q} \quad (7)$$

Having determined the uranium temperature, the heat transfer rate in the radially outward direction can be determined by using the equation below

$$q_{out} = \frac{T_{uranium} - T_{coolant}}{R_{eff\,out}} \quad (8)$$

Similarly the heat transfer rate in the radially inward direction can be determined using

$$q_{in} = \frac{T_{uranium} - T_{coolant}}{R_{eff\,in}} \quad (9)$$

The heat fluxes in the radially inward (q''_{in}) and outward directions (q''_{out}) can be determined by dividing the heat transfer rates by the curved surface area ($2 \pi r L$).

The symbolic dimensions of the assembly are illustrated in Fig 12 to provide a better understanding of the resistance networks and the equations. Having obtained the uranium temperature and the individual heat flow rates, a thermal resistance network was used to determine the temperature distribution on the inner and the outer tubes. For radially outward heat

flow through the outer tube cladding the temperature distribution, based on the thermal resistance network in Fig 11, is represented by Eq. (10).

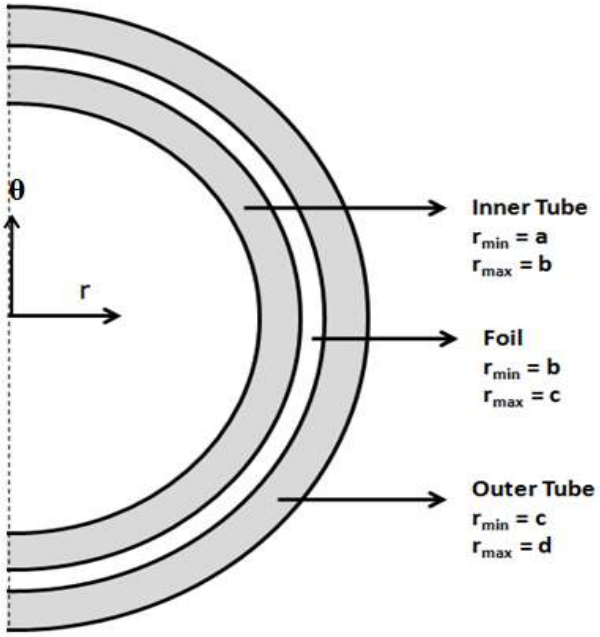

Figure 12. Annular target assembly setup in Abaqus FEA.

$$T(r)_{out} = T_{\infty} + \left(\frac{q''_{out}}{k_{out}} * c\right) * \left[Log\left(\frac{d}{r}\right) + \left(\frac{k_{out}}{d * h_d}\right)\right] \quad (10)$$

where,

'c' is the inner radius of the outer tube , 'd' is the outer radius of the outer tube , 'r' is the radius at any location, 'h_d' is the outer heat transfer coefficient , 'T_{∞}' is the coolant temperature and ' q''_{out}' is the radially outward heat flux.

For radially inward heat flow through the outer tube cladding the temperature distribution, based on the thermal resistance network in Fig 11, is represented by Eq. (11).

$$T(r)_{in} = T_{\infty} + \left(\frac{q''_{in}}{k_{in}} * b\right) * \left[Log\left(\frac{r}{a}\right) + \left(\frac{k_{in}}{a * h_a}\right)\right] \quad (11)$$

where,

'a' is the inner radius of the inner tube , 'b' is the outer radius of the inner tube , 'r' is the radius at any location, 'h_a' is the inner heat transfer coefficient , 'T_{∞}' is the coolant temperature and ' q''_{in}' is the radially inward heat flux.

With the knowledge of the temperature distribution through the inner and the outer tubes, the stresses can be easily obtained. Since the outer tube separates from the foil due to the difference in thermal expansion coefficients and heat flow direction, it can be treated as a single tube subject to radially outward heat flow. The expression for radial and hoop stresses in a long cylinder with a central circular hole from Timoshenko and Goodier (1951) is given by

$$\sigma_{r_{out}} = \frac{\alpha * E}{(1-v)r^2} \left[\frac{r^2-c^2}{d^2-c^2} \int_c^d T(r)_{out}\ r\, dr - \int_c^r T(r)_{out}\, r\, dr \right] \quad (12)$$

$$\sigma_{\theta_{out}} = \frac{\alpha * E}{(1-v)r^2} \left[\frac{r^2+c^2}{d^2-c^2} \int_c^d T(r)_{out}\, r\, dr + \int_c^r T(r)_{out}\, r\, dr - T(r)_{out} r^2 \right] \quad (13)$$

Using T_{out} from Eq. (10) along with the knowledge of 'r', tube dimensions and the material properties, the radial and hoop stresses on the outer tube can be determined. The displacement of the surface due to thermal gradients at any location along the radius of the tube can be obtained from Boley (1960) as

$$u_{out} = \frac{\alpha}{r(1-v)} \left[(1+v) \int_c^r T(r)_{out}\, r\, dr + \frac{(1-3v)r^2 + c^2(1+v)}{d^2-c^2} \int_c^d T(r)_{out}\, r\, dr \right] \quad (14)$$

In Eqs (12-14) ,'σ_r'is the radial stress , 'σ_Θ' represents the hoop stress , 'c' is the inner radius of the outer tube , 'd' is the outer radius of the outer tube, 'r' is the radius at any location, '$T(r)_{out}$' represents the temperature at any radius 'r' along the outer tube, 'u_{out}' represents the displacement in the outer tube.

The formulation for thermal stresses in a single tube subject to a heat flux can be applied to the outer tube as it separates from the foil. Hence the properties of the outer tube alone need to be accounted for in calculating the stresses and displacement. However, the inner tube bonds with the foil and as a result the composite structure of the foil and the inner tube cladding should be considered in predicting the thermal stresses in the inner tube and the displacement of the surfaces. The symbolic dimensions of the inner tube- foil composite is illustrated below in Fig 13.

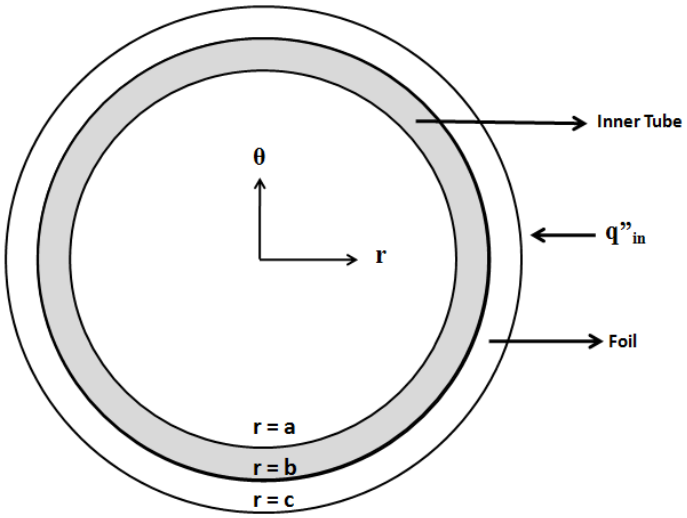

Figure 13. Heat flow through the inner tube-foil composite.

To solve for the stresses and displacement on the inner tube, two boundary conditions and two compatibility conditions at the interface are required. Due to the absence of any

externally applied load, the radial stress at the inner surface of the inner tube and outer surface of the foil will be zero. For perfect contact to exist at the interface of the LEU foil and the inner tube, the interface condition dictates that the stresses should be equal and the displacement of the surfaces in contact should be equal. For a long circular cylinder, from Timoshenko and Goodier (1951), the displacement, hoop and radial stresses on the inner tube are given by

$$u_{in} = \frac{1+v_{in}}{1-v_{in}} \cdot \frac{\alpha_{in}}{r} \int_a^r T(r)_{in}\, r\, dr + C_1 r + \frac{C_2}{r} \tag{15}$$

$$\sigma_{r\,in} = \frac{-\alpha_{in} E_{in}}{(1-v_{in}) r^2} \int_a^r T(r)_{in} r\, dr + \frac{E_{in}}{(1+v_{in})} \left[\frac{C_1}{1-2v_{in}} - \frac{C_2}{r^2}\right] \tag{16}$$

$$\sigma_{\theta\,in} = \frac{\alpha_{in} E_{in}}{(1-v_{in}) r^2} \int_a^r T(r)_{in} r\, dr - \frac{\alpha_{in} E_{in} T(r)_{in}}{1-v_{in}} + \frac{E_{in}}{(1+v_{in})} \left[\frac{C_1}{1-2v} + \frac{C_2}{r^2}\right] \tag{17}$$

Similarly, from Timoshenko and Goodier (1951), the displacement, hoop and radial stresses on the foil are given by

$$u_{foil} = \frac{1+v_{foil}}{1-v_{foil}} \cdot \frac{\alpha_{foil}}{r} \int_a^r T(r)_{foil}\, r\, dr + C_3 r + \frac{C_4}{r} \tag{18}$$

$$\sigma_{r\,foil} = \frac{-\alpha_{foil} E_{foil}}{(1-v_{foil}) r^2} \int_a^r T(r)_{foil} r\, dr + \frac{E_{foil}}{(1+v_{foil})} \left[\frac{C_3}{1-2v_{foil}} - \frac{C_4}{r^2}\right] \tag{19}$$

$$\sigma_{\theta\,foil} = \frac{\alpha_{foil} E_{foil}}{(1-v_{foil}) r^2} \int_a^r T(r)_{foil} r\, dr - \frac{\alpha_{foil} E_{foil} T(r)_{in}}{1-v_{foil}} + \frac{E_{foil}}{(1+v_{foil})} \left[\frac{C_3}{1-2v} + \frac{C_4}{r^2}\right] \tag{20}$$

The boundary conditions are:

1. $\sigma_r|_{r=a} = 0$ (21)
2. $\sigma_r|_{r=c} = 0$ (22)

The compatibility conditions at the interface of the LEU foil and inner tube are:

1. $\sigma_{r_{in}}|_{r=b} = \sigma_{r_{foil}}|_{r=b}$ (23)

2. $r_{b_{in}} + u_{b_{in}} = r_{b_{foil}} + u_{b_{foil}}$ (24)

In Eqs.(15-34), 'a','b' and 'c' are as represented in Fig 13. 'u' is the radial displacement , 'σ_r' represents the radial stress, 'σ_Θ' represents the hoop stress, '$T(r)_{in}$' is the radial temperature distribution in the inner tube.

Using Eq.(21) in Eq. (16) , Eq. (22) in Eq. (19) , Eq. (24)in Eq. (15) and Eq.(18) , a system of four simultaneous linear equations are obtained and are solved to determine the four constants C_1, C_2, C_3, C_4. Hence the stresses and displacement on the inner tube are given by

$$\sigma_{r_{in}} = \frac{\alpha_{in}E_{in}(a^2 - r^2)(T(r)_{in} - T_\infty)(1 + \frac{\nu_{in}}{1-\nu_{in}})}{2r^2(1-\nu_{in}^2)} + \frac{E_{in}[-\frac{c_2\left(1-\frac{\nu_{in}}{1-\nu_{in}}\right)}{r^2} + c_1\left(1+\frac{\nu_{in}}{1-\nu_{in}}\right)]}{(1-\nu_{in}^2)(1-\frac{\nu_{in}^2}{(1-\nu_{in})^2})} \quad (25)$$

$$\sigma_{\theta_{in}} = \frac{-\alpha_{in}E_{in}(T_{in} - T_\infty)(1 + \frac{\nu_{in}}{1-\nu_{in}})}{1-\nu_{in}^2} - \frac{\alpha_{in}E_{in}(a^2 - r^2)(T_{in} - T_\infty)\left(1+\frac{\nu_{in}}{1-\nu_{in}}\right)}{2r^2(1-\nu_{in}^2)} + \frac{E_{in}[\frac{c_2\left(1-\frac{\nu_{in}}{1-\nu_{in}}\right)}{r^2} + c_1\left(1+\frac{\nu_{in}}{1-\nu_{in}}\right)]}{(1-\nu_{in}^2)(1-\frac{\nu_{in}^2}{(1-\nu_{in})^2})} \quad (26)$$

$$u_{in} = \frac{c_2}{r} + c_1 r - \frac{\alpha_{in}(a^2-r^2)(T_{in}-T_\infty)(1+\frac{\nu_{in}}{1-\nu_{in}})^2}{2r(1-\frac{\nu_{in}}{1-\nu_{in}})} \quad (27)$$

In Eqs. (25-27), the constants C_1 and C_2 are given by

$$C_1 = \left(\frac{\begin{array}{c}[(-1+2\nu_{in})(a^2\alpha_{in}\Delta T_{in}(b^2(E_{in}+E_{foil}+E_{foil}\nu_{in}-E_{in}\nu_{foil}-2E_{in}\nu_{foil}^2) \\ +E_{in}(1+\nu_{foil}))+ b^2(2\alpha_{foil}(b^2-c^2)E_{foil}\Delta T_{foil}(-1+\nu_{in})^2(1+\nu_{in})(1+\nu_{foil}) \\ +\alpha_{in}\Delta T_{in}(c^2(E_{foil}(1+\nu_{in})-E_{in}(1+\nu_{foil})) \\ +b^2(-E_{foil}(1+\nu_{in})+E_{in}(-1+\nu_{foil}+2\nu_{foil}^2))))]\end{array}}{\begin{array}{c}[2(-1+\nu_{in})^2(b^2(c^2(E_{in}+E_{foil}-E_{foil}\nu_{in}-2E_{foil}\nu_{in}^2+E_{in}\nu_{foil}) \\ +b^2(E_{foil}(-1+\nu_{in}+2\nu_{in}^2)-E_{in}(-1+\nu_{in}+2\nu_{foil}^2)))+a^2(c^2(E_{foil}(1+\nu_{in}) \\ -E_{in}(1+\nu_{foil}))+ b^2(-E_{foil}(1+\nu_{in})+E_{in}(-1+\nu_{foil}+2\nu_{foil}^2)))))]\end{array}} \right) \quad (28)$$

$$C_2 = \left(\frac{\begin{array}{c}[a^2(a^2\alpha_{in}\,\Delta T_{in}(c^2(E_{foil}(1+\nu_{in})-E_{in}(1+\nu_{in}))+b^2(-E_{foil}(1+\nu_{in}) \\ +E_{in}(-1+\nu_{foil}+2\nu_{foil}^2)))+b^2(-2\alpha_{foil}(b^2-c^2)E_{foil}\Delta T_{foil}(-1+\nu_{in})^2 \\ (1+\nu_{in})(1+\nu_{foil}) + \alpha_{in}\Delta T_{in}(b^2(E_{in}+E_{foil}+E_{foil}\nu_{in}-E_{in}\nu_{foil} \\ -2\nu_{foil}^2E_{in})+c^2(-E_{foil}(1+\nu_{in})+E_{in}(1+\nu_{foil})))))]\end{array}}{\begin{array}{c}[\,2\,(-1+\nu_{in})^2(b^2(c^2(E_{in}+E_{foil}-E_{foil}\nu_{in}-2E_{foil}\nu_{in}^2+E_{in}\nu_{foil}) \\ +b^2(E_{foil}(-1+\nu_{in}+2\nu_{in}^2)-E_{in}(-1+\nu_{foil}+2\nu_{foil}^2)))+a^2(c^2(E_{foil} \\ (1+\nu_{in})-E_{in}(1+\nu_{foil}))+ b^2(-E_{foil}(1+\nu_{in})+E_{in}(-1+\nu_{foil}+2\nu_{foil}^2))))]\end{array}} \right) \quad (29)$$

$$C_3 = \left(\frac{\begin{array}{c}-[(-1+\nu_{foil}+2\nu_{foil}^2)(b^2(-2\alpha_{in}b^2E_{in}\Delta T_{in}(-1+\nu_{foil})+\alpha_{foil}(b^2-c^2) \\ \Delta T_{foil}(1+\nu_{in})(E_{in}+E_{foil}-E_{foil}\nu_{in}-2E_{foil}\nu_{in}^2+E_{in}\nu_{foil}))+a^2(2\alpha_{in}b^2E_{in} \\ \Delta T_{in}(-1+\nu_{in})\alpha_{foil}(b^2-c^2)\Delta T_{foil}(-1+\nu_{in})(E_{foil}(1+\nu_{in})-E_{in}(1+\nu_{foil})))]\end{array}}{\begin{array}{c}[\,2(-1+\nu_{in})(-1+\nu_{foil})(b^2(c^2(E_{in}+E_{foil}-E_{foil}\nu_{in}-2E_{foil}\nu_{in}^2+E_{in}\nu_{foil}) \\ +b^2(E_{foil}(-1+\nu_{in}+2\nu_{in}^2)-E_{in}(-1+\nu_{foil}+2\nu_{foil}^2)))+ a^2(c^2(E_{foil}(1+\nu_{in}) \\ -E_{in}(1+\nu_{foil}))+b^2(-E_{foil}(1+\nu_{in})+E_{in}(-1+\nu_{foil}+2\nu_{foil}^2))))]\end{array}} \right) \quad (30)$$

$$C_4 = \left(\frac{\begin{array}{c}(b^2(1+\nu_{foil})(a^2(2\alpha_{in}c^2E_{in}\Delta T_{in}(-1+\nu_{foil})+\alpha_{foil}(b^2-c^2)\Delta T_{foil}(-1+\nu_{in}) \\ (E_{in}+E_{foil}+E_{foil}\nu_{in}-E_{in}\nu_{foil}-2E_{in}\nu_{foil}^2))+ b^2(-2\alpha_{in}c^2E_{in}\Delta T_{in}(-1+\nu_{in}) \\ \alpha_{foil}(b^2-c^2)\Delta T_{foil}(-1+\nu_{in})(-E_{foil}(-1+\nu_{in}+2\nu_{in}^2)+E_{in}(-1+\nu_{foil}+2\nu_{foil}^2))))]\end{array}}{\begin{array}{c}[\,2(-1+\nu_{in})(-1+\nu_{foil})(b^2(c^2(E_{in}+E_{foil}-E_{foil}\nu_{in}-2E_{foil}\nu_{in}^2+E_{in}\nu_{foil}) \\ +\,b^2(E_{foil}(-1+\nu_{in}+2\nu_{in}^2)-E_{in}(-1+\nu_{foil}+2\nu_{foil}^2)))+\,a^2(c^2(E_{foil}(1+\nu_{in}) \\ -E_{in}(1+\nu_{foil}))+b^2(-E_{foil}(1+\nu_{in})+E_{in}(-1+\nu_{foil}+2\nu_{foil}^2))))]\end{array}} \right) \quad (31)$$

The constants C_3 and C_4 along with Eqs. (18-20), after substituting the appropriate material properties and temperature distribution across the foil, can be used to determine the stresses and displacement on the foil. The contact pressure at the interface of the uranium foil and the inner tube aluminum cladding can be obtained by using Madhusudhana's model (Madhusudhana, 1998). He postulated that the contact pressure depends on the total interference between the cylinders in contact. This total interference consists of the interference due to temperature gradients, u_A, interference due to contact resistance u_B and the initial interference u_C . Hence the contact pressure due to the total interference, U, between the cylinders is given by Ugural and Fenster (1975) as

$$\frac{U}{b} = \frac{P_{contact}}{E_{in}}\left\{\frac{E_{in}}{E_{foil}}\left[\frac{c^2+b^2}{c^2-b^2} + \nu_{foil}\right] + \left[\frac{b^2+a^2}{b^2-a^2} + \nu_{in}\right]\right\} \qquad (32)$$

where,

$U = u_A + u_B + u_C$ is the total interference.

'a' is the inner radius of the inner tube, 'b' is the outer radius of the inner tube and inner radius of the foil and 'c' is the outer radius of the foil.

The net interference due to heat flow is given by

$$\frac{u_A}{b} = \frac{\alpha_{in}\Delta T_{in}}{2\log\frac{b}{a}}\left\{\left[1 - \frac{2a^2\log\frac{b}{a}}{b^2-a^2}\right] - \left(\frac{\alpha_{foil}k_{in}}{\alpha_{in}k_{foil}}\right)\left[1 - \frac{2c^2\log\frac{c}{b}}{c^2-b^2}\right]\right\} \qquad (33)$$

The interference due to contact resistance is given by

$$\frac{u_B}{b} = (\alpha_{in} - \alpha_{foil})(T_a - \Delta T_{in}) + \frac{\alpha_{foil} k_{in} \Delta T_{in}}{b \log \frac{b}{a}} \left[\frac{1}{h_s + \left(\frac{k_{gas}}{3\sigma} \right)} \right] \quad (34)$$

where ,

h_s is the solid spot conductance given by Mikic (1974) as

$$h_s = 1.13 \tan\theta \frac{K_{eff}}{\sigma} \left(\frac{P_{contact}}{H} \right)^{0.94} \quad (35)$$

where ,

'h_s' is the solid spot conductance , 'Θ' represents the asperity slope , 'K_{eff}' is the effective thermal conductivity, 'σ' is the root mean square value of surface roughness, '$P_{contact}$' is the contact pressure and 'H' is the micro-hardness of the softer material.

The denominator of the second term in Eq. (34) represents the total conductance which is the sum of the solid spot conductance and gas gap conductance. If Eq. (35) is to be considered, an iterative procedure is required to determine the contact pressure. Since the uranium foil and the inner tube cladding are in perfect contact in the model under consideration, an infinite total conductance (a high value of total conductance, h) was used in the calculations for this analysis. Using Eqs. (33 and 34) in Eq. (32) and taking the initial interference, u_C, as zero due to perfect contact , the contact pressure can be calculated.

Chapter 6: Results

The uniform heating results and validation will be presented first, followed by the non-uniform heating results. Then, a comparison between the uniform and non-uniform heating results will be presented in an attempt to validate the results of the uniformly heated region in the non-uniform heating model.

6.1 Uniform Heating Results

The uniform heating numeric model developed using Abaqus FEA was validated using the thermal stress equations, as explained in chapter 5. The inner and outer tube heat transfer coefficients, inner and outer tube thickness and the heat generation rate were the parameters that were varied to determine how the target would behave under various conditions. Also, the conditions under which the target could potential fail have been identified and presented. Figure 14 shows the temperature distribution contour of the assembly.

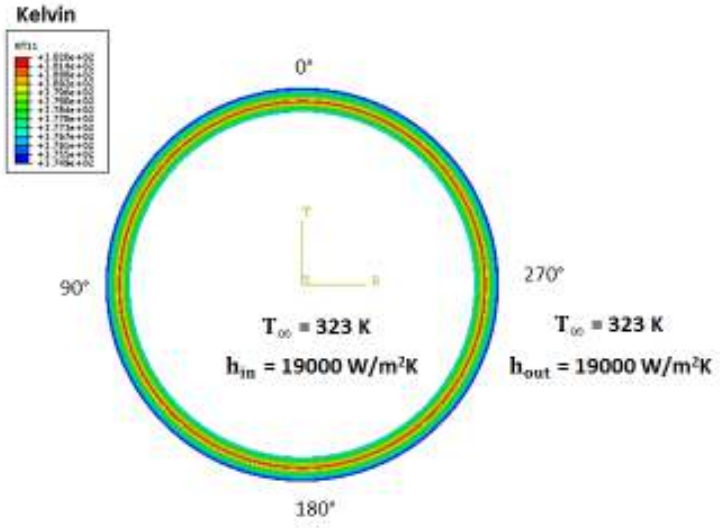

Figure 14. Assembly temperature distribution contour with q''' = 1.6 x 10^{10} W/m^3 for the case of uniform heating.

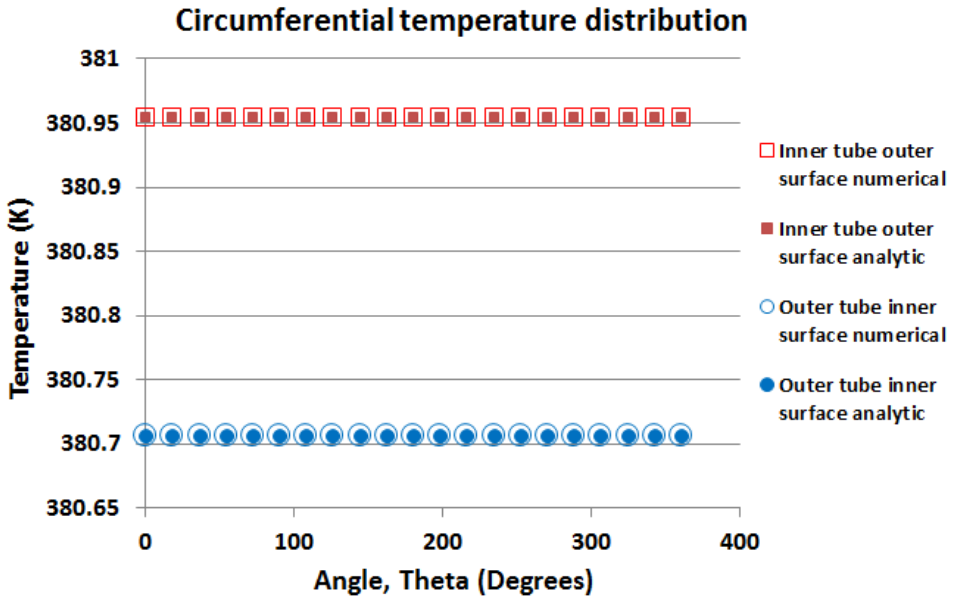

Figure 15. Circumferential temperature distribution on the inner and outer tubes with q''' = 1.6 x 10^{10} W/m^3 for the case of uniform heating.

For the uniform heating case, where the foil is modeled as a complete cylinder, the temperature distribution along the circumference of the inner and outer tubes at their respective interfaces is a constant as illustrated in Fig 15. This is expected due to uniform heating along the circumference of the tubes and no circumferential variation in temperature exists. The analytic temperature distribution through the outer tube was obtained using Eq. (10) and the analytic temperature distribution through the inner tube was obtained using Eq. (11). The radial temperature drop due to radially inward heat flow into the inner tube cladding and radially outward heat flow into the outer tube cladding is illustrated in Fig 16 in the following page. The coolant flowing along the inner surface of the inner tube and over the outer surface of the outer tube creates the required temperature gradient for effective heat dissipation. The analytical and numerical temperature values are in good agreement with each other.

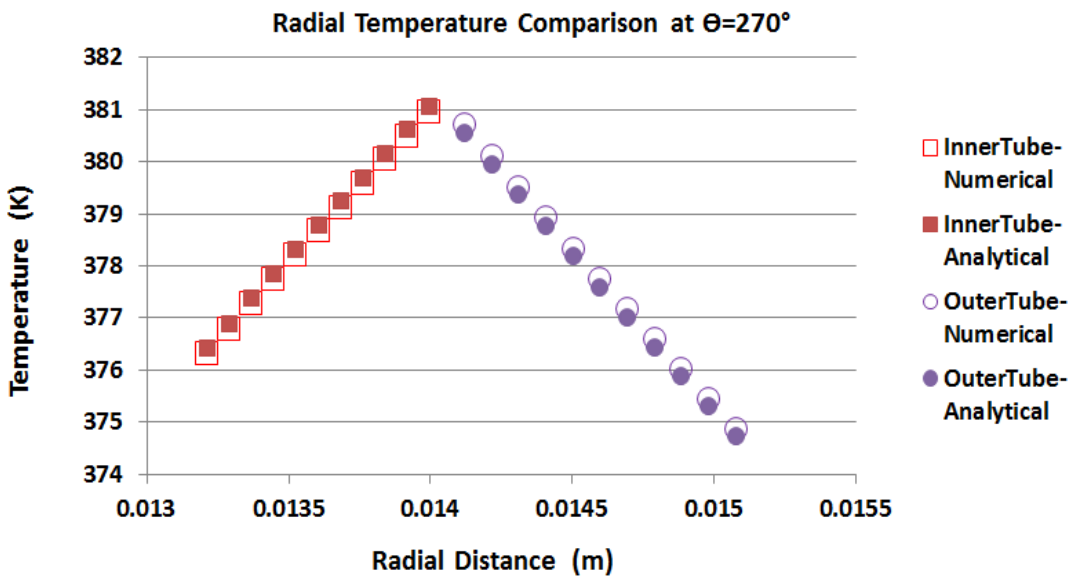

Figure 16.Temperature drop across the inner and outer aluminum cladding with q''' = 1.6 x 10^{10} W/m^3 for the case of uniform heating.

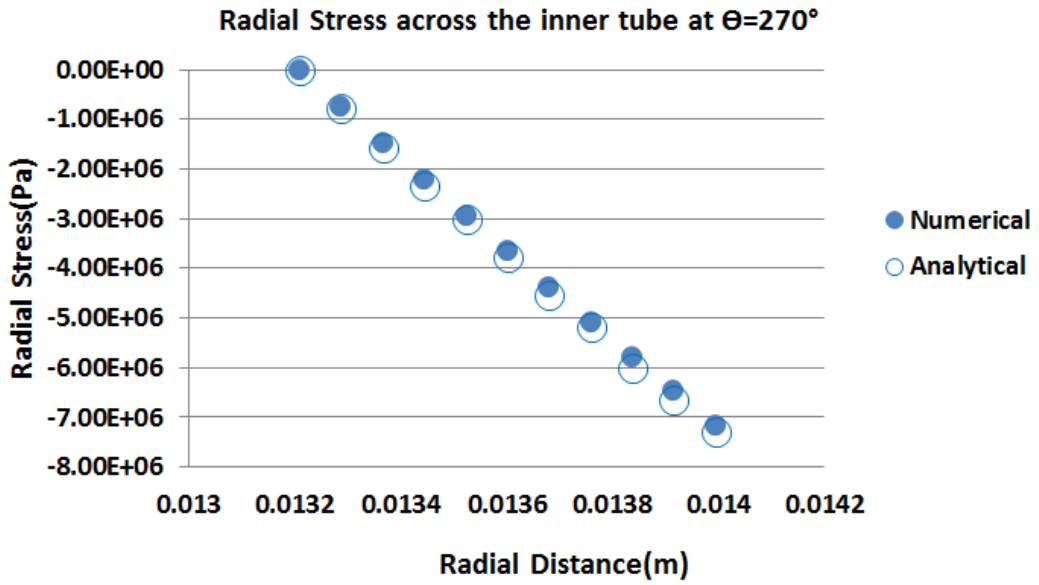

Figure 17. Inner tube radial stress distribution with q''' = 1.6 x 10^{10} W/m^3 for the case of uniform heating.

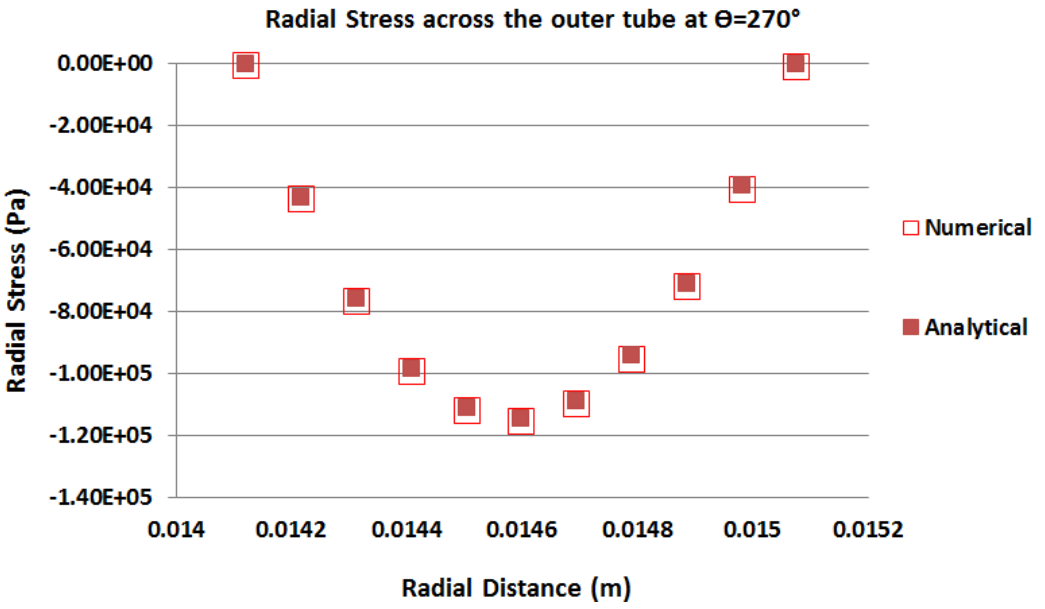

Figure 18. Outer tube radial stress comparison with q''' = 1.6 x 10^{10} W/m^3 for the case of uniform heating.

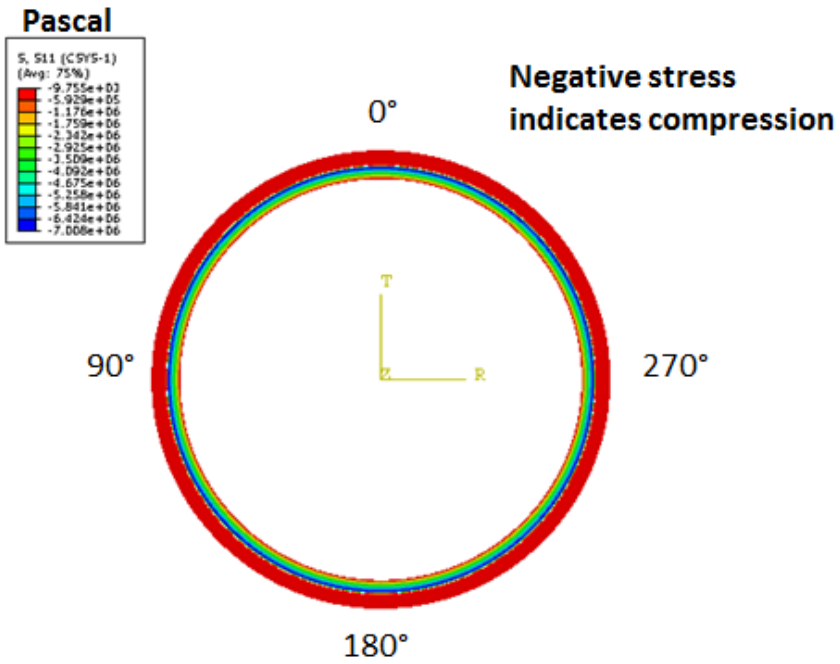

Figure 19. Assembly radial stress contour with q''' = 1.6 x 10^{10} W/m^3 for the case of uniform heating.

Figure 17 and Fig 18 show that the radial stresses on the inner and outer tubes are compressive in nature. It is to be noted here that the thermal expansion coefficient of the Uranium foil ($\alpha = 1.39 \times 10^{-5}\ K^{-1}$) is lesser than that of Aluminum ($\alpha = 2.34 \times 10^{-5}\ K^{-1}$). Hence, for radially inward heat flow into the inner tube, due to a higher thermal expansion coefficient, the outer surface of the inner tube tends to expand a lot more than the inner surface of the foil. As a result, the foil acts as a barrier to the expansion of the inner tube, resulting in compressive stresses being generated. Similarly the stresses in the outer tube are compressive in nature as the temperature gradient at the outer tube-foil interface is greater than at its outer surface. Hence the inner surface of the outer tube tends to move outward by expanding, but the outer surface doesn't expand as much due to a comparatively lower temperature gradient. Hence, compressive stresses are generated in the outer tube with radially outward heat flow from a material of lower thermal expansion coefficient (Uranium) to a material of higher thermal expansion coefficient (Aluminum).

The magnitudes of compressive stresses on the outer tube are comparatively lower as compared to that of the inner tube. This is because contact is relaxed between the outer tube and the foil while it is reinforced between the inner tube and the foil (due to heat flow direction and thermal expansion coefficient of the materials under consideration). Hence the stresses in the outer tube can be determined by considering the material properties of the outer tube alone. However for the inner tube the composite structure of the inner tube and the foil must be considered due to reinforced contact.

If an attempt is made to come up with an analytic model that considers the properties of the inner tube alone, then the stresses predicted by that model will be tensile in nature. The reason compressive stresses are being induced in the inner tube is because the foil acts as a

barrier to the expansion of the outer surface of the inner tube. Hence this important aspect needs to be considered in developing an analytic model. More information on the development of the analytic model to predict the stresses on the inner tube can be found in chapter 5.

Figures 20-22 shows the hoop stress distribution across the inner tube, assembly and the outer tube respectively. The hoop stresses across the radius of the inner tube are predominantly compressive in nature. This can be attributed to the radially inward heat flow into the inner tube and the foil, which acts as a barrier to the free expansion of the inner tube. A lower temperature gradient on the inner surface of the inner tube and the fact that the free expansion of the outer surface of the inner tube is restricted by the foil results in compressive hoop stresses across the inner tube. The hoop stresses on the outer tube move from being compressive to tensile across the radius. This can be attributed to radially outward heat flow through the outer tube and the outer surface of the outer tube is free to expand. The free expansion of the outer surface of the outer tube results in tensile stresses being generated across the outer half of the tube. Now the expansion of the inner surface is resisted by the elements across the thickness of the tube. This is why the hoop stress moves from being compressive to tensile across the radius of the outer tube.

The analytical hoop stress values obtained using Eq.13 for the outer tube and using Eq. (17) for the inner tube are in good agreement with the numerical values as illustrated by Fig 20 and Fig 22.It is important to accurately predict the hoop stresses as these stresses dictate the failure of the material. To analyze this particular target, it will be sufficient to analyze the point of failure of the inner and outer surfaces of the inner tube

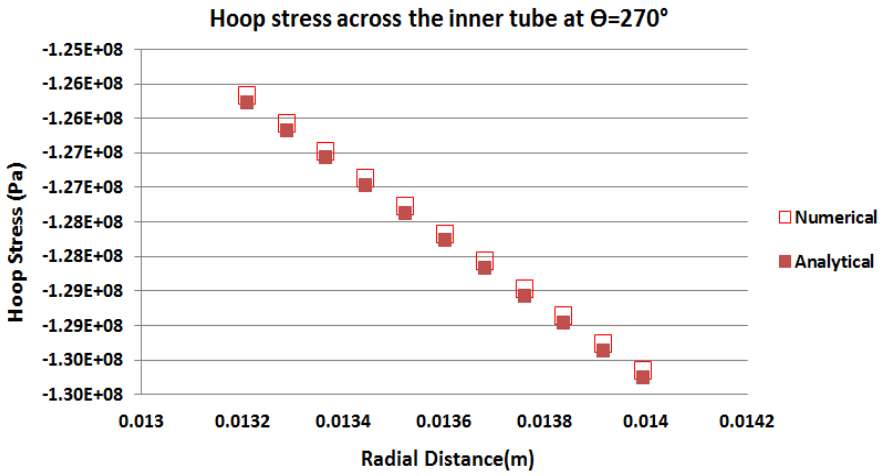

Figure 20. Hoop stress distribution across the radius of the inner tube with q''' = 1.6 x 10^{10} W/m^3 for the case of uniform heating.

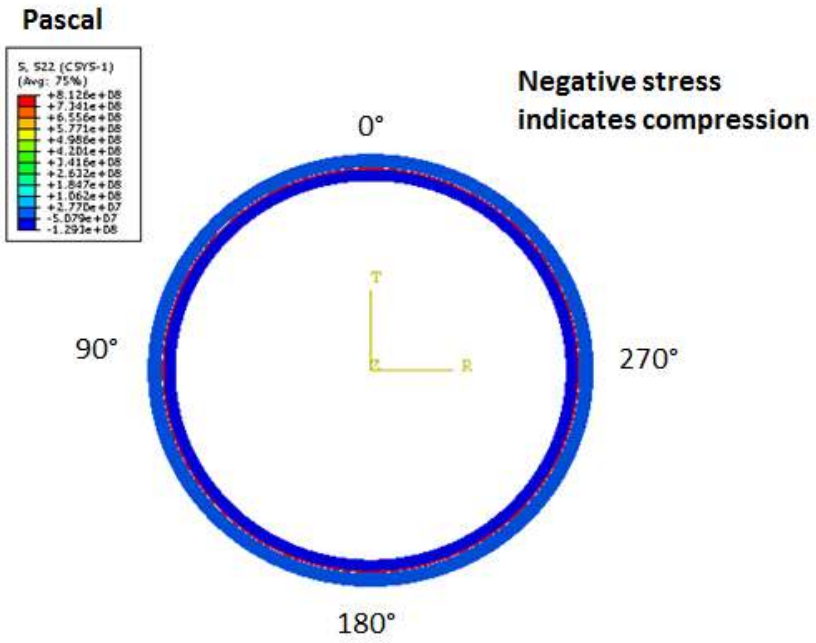

Figure 21. Assembly hoop stress distribution contour with q''' = 1.6 x 10^{10} W/$m^3$for the case of uniform heating.

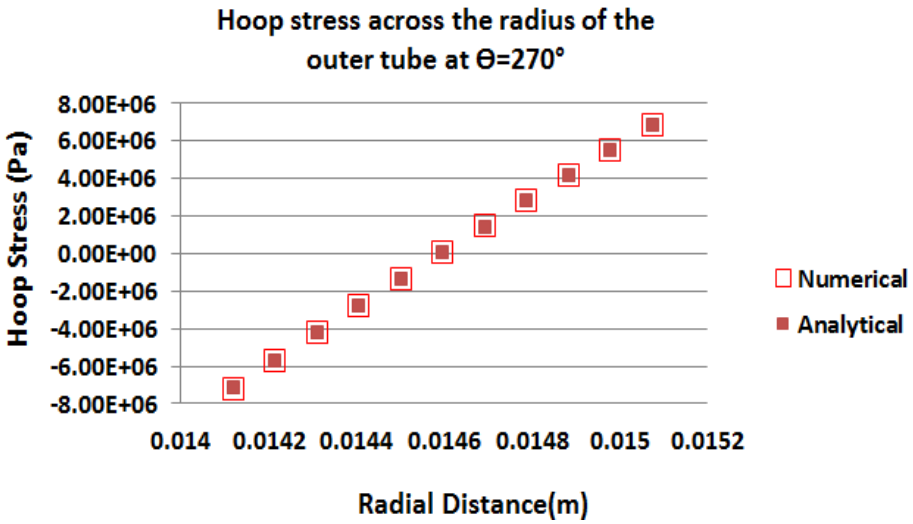

Figure 22. Outer tube hoop stress distribution with q''' = 1.6 x 10^{10} W/m^3 for the case of uniform heating.

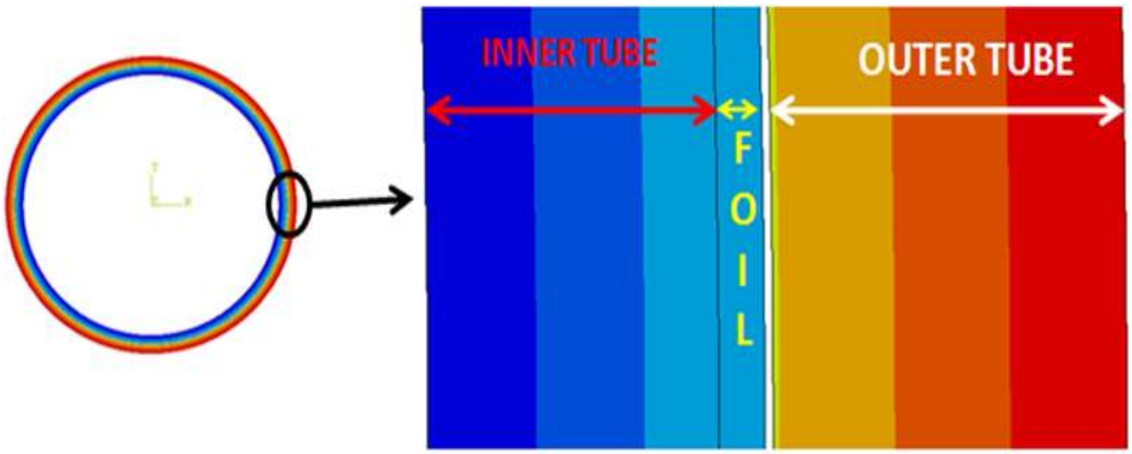

Figure 23. Graphic showing the separation between the foil and the outer tube with q''' = 1.6 x 10^{10} W/m^3 for the case of uniform heating.

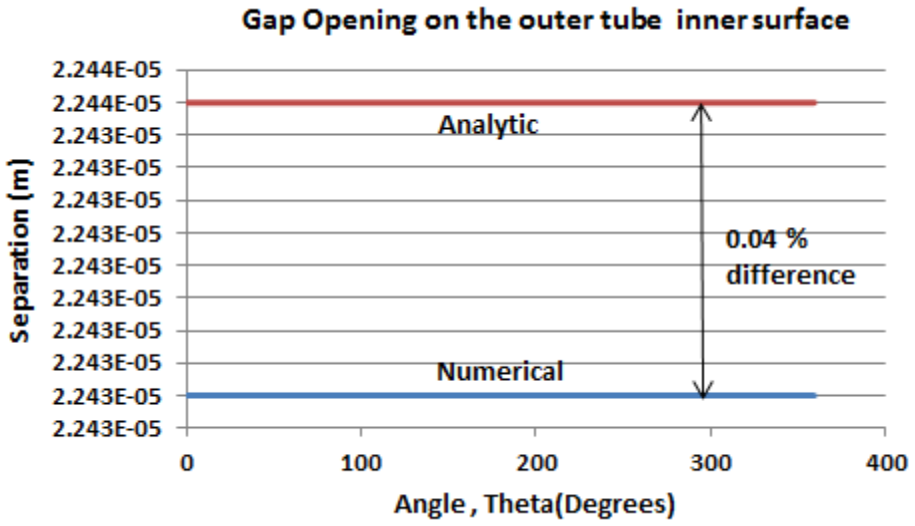

Figure 24.Separation between the foil and the outer tube cladding with q''' = 1.6 x 10^{10} W/m^3 for the case of uniform heating.

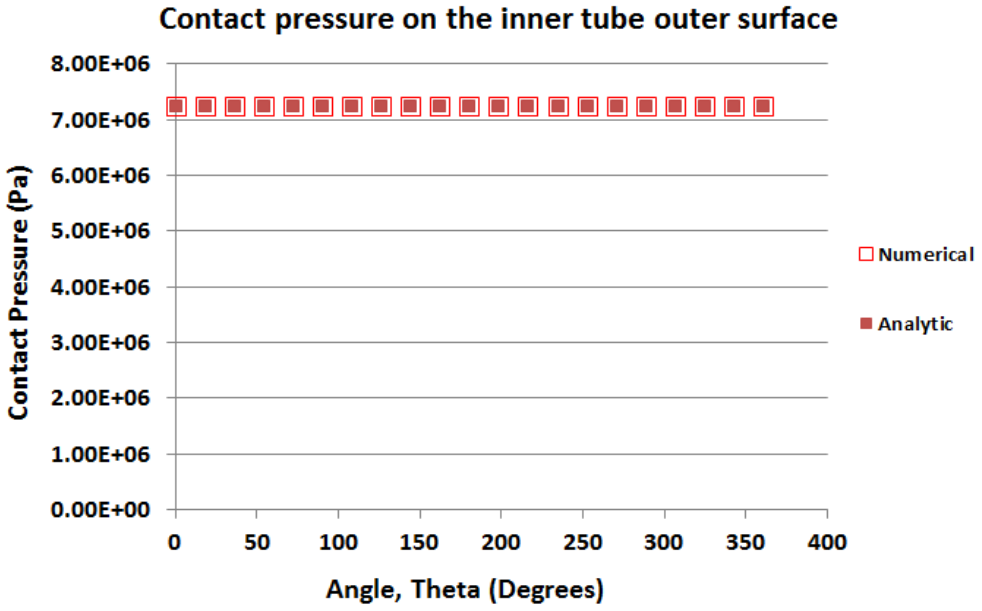

Figure 25. Contact pressure distribution on the inner tube with q''' = 1.6 x 10^{10} W/m^3 for the case of uniform heating.

Figures 23-25 illustrates the interface contact conditions. Figures 23 and 24 show that a uniform gap opens up between the foil and the outer tube due to difference in thermal expansion coefficients and radially outward heat flow. The analytical value for separation between the foil and the outer tube was obtained by subtracting the displacement of the foil outer surface (Eq. (18)) from that of the outer tube inner surface (Eq. (14)). The contact pressure on the inner tube due to contact between the foil and the inner cladding is shown in Fig 25. The numerical values were validated using Madhusudhana's model (Madhusudhana, 1998) and were found to be within 0.70 % of each other. A summary of the percent difference comparison on the inner tube and outer tube are presented in Table 3 and Table 4 respectively.

Table 3. Percent difference comparison between the analytic and numerical model across the inner tube radius

Radial Distance ($\times 10^{-3}$ m)	Temperature (% difference)	Radial Stress (% difference)	Hoop Stress (% difference)
13.210	0.028	-------	1.643
13.289	0.029	3.618	1.638
13.367	0.029	3.104	1.862
13.446	0.030	2.954	1.928
13.524	0.030	2.488	2.378
13.603	0.031	1.134	2.370
13.681	0.030	1.572	2.852
13.759	0.031	1.922	1.078
13.838	0.031	2.134	3.083
13.917	0.032	2.782	2.599
13.995	0.030	1.654	3.065

Table 4. Percent difference comparison between the analytic and numerical model across the outer tube radius

Radial Distance (x 10^{-3} m)	Temperature (% difference)	Radial Stress (% difference)	Hoop Stress (% difference)
14.120	0.039	------	0.235
14.216	0.040	1.005	0.442
14.311	0.039	1.038	0.321
14.407	0.039	0.823	0.354
14.502	0.038	0.893	0.452
14.598	0.039	0.934	0.893
14.693	0.038	1.013	0.089
14.789	0.038	1.573	0.172
14.884	0.037	1.191	0.216
14.979	0.037	2.743	0.201
15.075	0.036	------	0.387

Table 3 presents the comparison between the analytic and the numerical models for the temperature, radial stress and hoop stress across the radius of the inner tube. The difference between the numerical temperatures obtained from Abaqus and the analytic temperature values obtained using Eq. (11) is within 0.05 %. Table 3 also shows that the analytical model that was derived (Eqs. (21-31)) to obtain the stresses on the inner tube is able to predict the radial and hoop stresses to within 4%. Also, the radial and hoop stress trends on the inner tube represented by Fig 17 and Fig 20 respectively show good agreement between the analytical and numerical values.

Table 4 presents the comparison between the analytical and numerical models for the temperature, radial and hoop stresses across the radius of the outer tube. The difference between the numerical temperatures obtained from Abaqus and the analytic temperature values obtained

using Eq. (10) is within 0.04 %. The analytical radial stresses were obtained using Eq. (12) while the analytic hoop stresses were determined using Eq. (13). Both these stresses were found to be within 3 %.Also, the radial and hoop stress trends on the outer tube represented by Fig 18 and Fig 22 respectively show good agreement between the analytical and numerical values.

From Figs 17,18,20 and 22 it is observed that the magnitude of hoop stress is greater than that of the radial stress and the magnitude of hoop stress on the inner tube is much higher than on the outer tube. Hence to assess the risk of failure of the target it will be sufficient to analyze the hoop stresses on the inner tube and compare them to the yield strength of the aluminum cladding. The yield strength of Al-6061-T6 is 250 MPa (2.50×10^8 Pa). From Fig 20, the maximum hoop stress on the inner tube in a compressive state is 1.30×10^8 Pa and this is well within the yield strength of the aluminum cladding. Hence for the current heat generation rate of the LEU (1.6×10^{10} W/m^3) the stresses induced in the target tubes are in the safe zone. A more detailed analysis of the performance of the target at higher LEU heat generation rates will be presented in the parametric studies chapter (chapter 7).

6.2 Non-Uniform Heating Results

Having validated the uniform heating model, the non-uniform heating results will be presented in this section which will be followed by the comparison between the uniform and non-uniform heating model. Figure 26 illustrates the assembly temperature distribution contour. The region on either side of 180° represents the tube-tube contact region. There is a temperature drop in this region due to absence of the heat generating LEU foil.

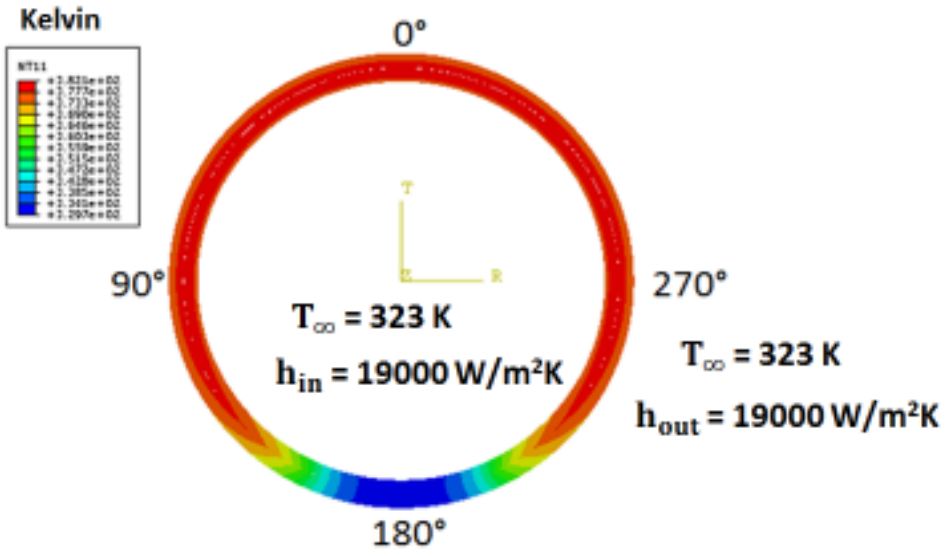

Figure 26. Assembly temperature distribution contour for non-uniform heating.

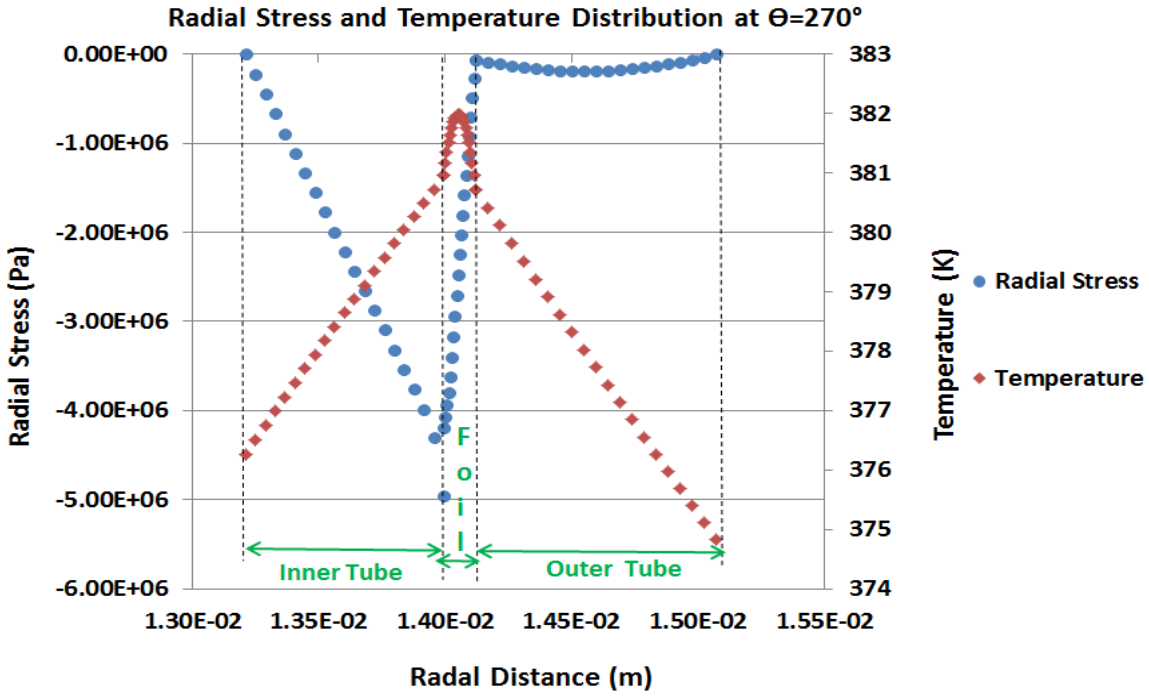

Figure 27. Radial stress and temperature distribution across the thickness for non-uniform heating (negative stress indicates compression)

Figure 27 illustrates the radial stress and temperature distribution across the thickness of the assembly. It is to be noted here that the thermal expansion coefficient of the Uranium foil ($\alpha = 1.39 \times 10^{-5} K^{-1}$) is lesser than that of Aluminum ($\alpha = 2.34 \times 10^{-5} K^{-1}$).Hence, for radially inward heat flow into the inner tube, due to a higher thermal expansion coefficient, the outer surface of the inner tube tends to expand more than the inner surface of the LEU foil. As a result, the foil acts as a barrier to the expansion of the inner tube, resulting in compressive stresses being generated. Similarly the radial stresses in the outer tube are compressive in nature as the temperature gradient at the outer tube-foil interface is greater than at its outer surface. Hence the inner surface of the outer tube tends to move outward by expanding, but the outer surface doesn't expand as much due to a comparatively lower temperature. Compressive stresses are generated in the outer tube with radially outward heat flow from a material of lower thermal expansion coefficient (Uranium) to a material of higher thermal expansion coefficient (Aluminum).

The radial displacement contour of the target is shown in Fig28. Beginning at 0°, there is no separation between the foil and the inner tube. A gap between the outer tube and the foil exists due to thermal expansion coefficient mismatch and radially outward heat flow through the outer tube. At 90 ° there is no separation between the foil and the inner tube. However , the magnitude of separation between the foil and the outer tube is lesser than at 0°. This shows that the maximum displacement occurs at the 0° location in Fig 28. Between 90° and 180° a separation transition region exists. This transition region is formed because the ends of the foil move away from the recess (Fig 37) and flap out as they expand. This causes the foil to pull away from the inner tube and make contact with the outer tube. This opens up a gap between the foil and the inner tube.

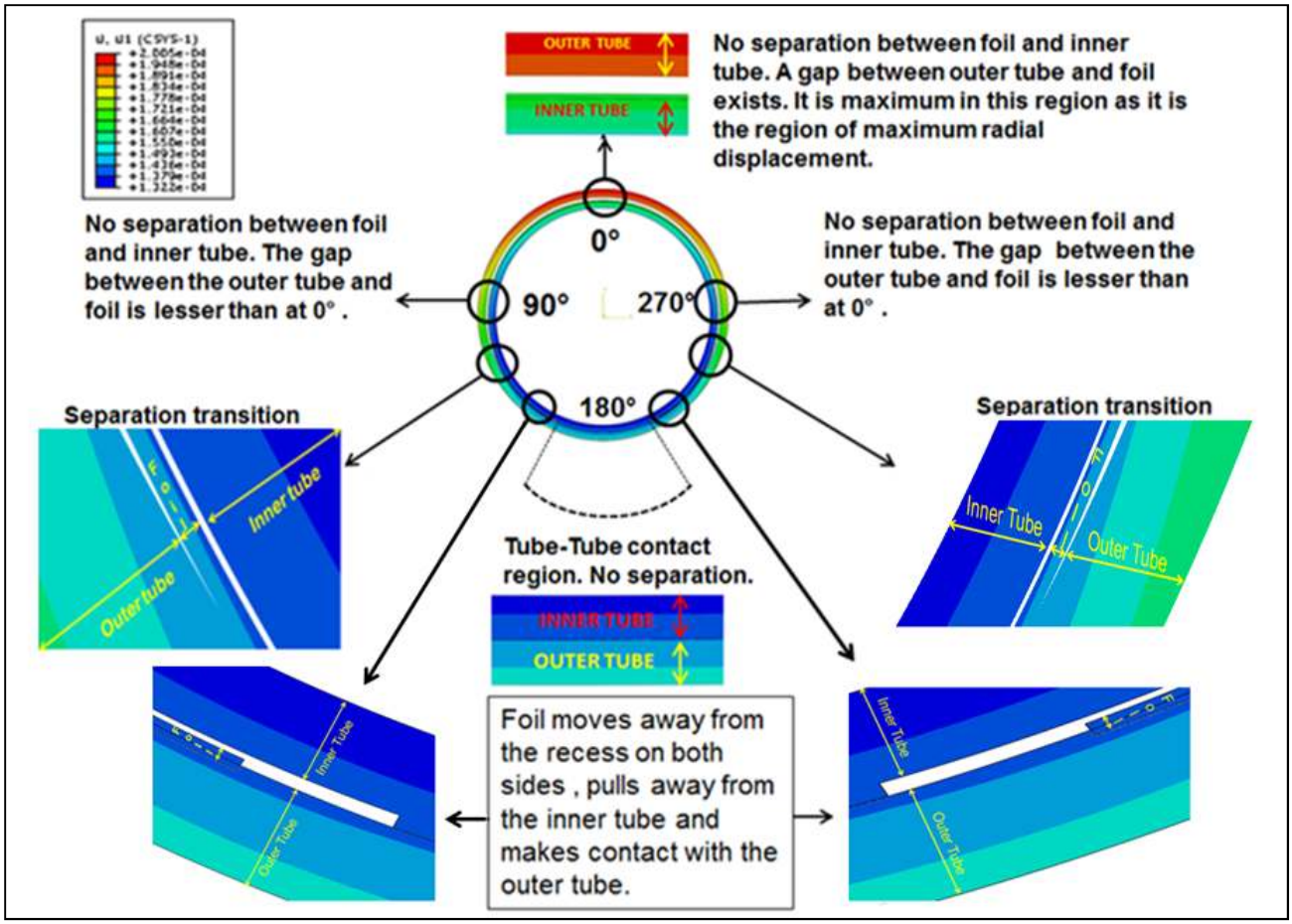

Figure 28.Radial displacement contour illustrating the separation between the foil and the cladding for non-uniform heating.

After the separation transition region, the foil separates from the outer tube and gradually moves closer to the inner tube and eventually makes contact. Now a gap opens up between the outer tube and the foil. This behavior is symmetric about the X-axis and hence the pattern repeats itself from 180° to 360°.

The separation explained in Fig 28 is illustrated by plotting the separation along the circumference of the outer tube –LEU foil interface (Fig 29). As explained previously, the magnitude of separation between the foil and the outer tube gradually begins to decrease from 0°

towards the tube-tube region at 180°. Figure 29 shows that zero separation exists to the left of 150° and a little after 200°. This implies that the LEU foil is in contact with the outer tube and a gap has opened up between the foil and the inner tube. Also, looking closely at the separation plot, a finite separation exists just after 150° and 200°. This is because the foil pulls away from the recess region resulting in finite separation.

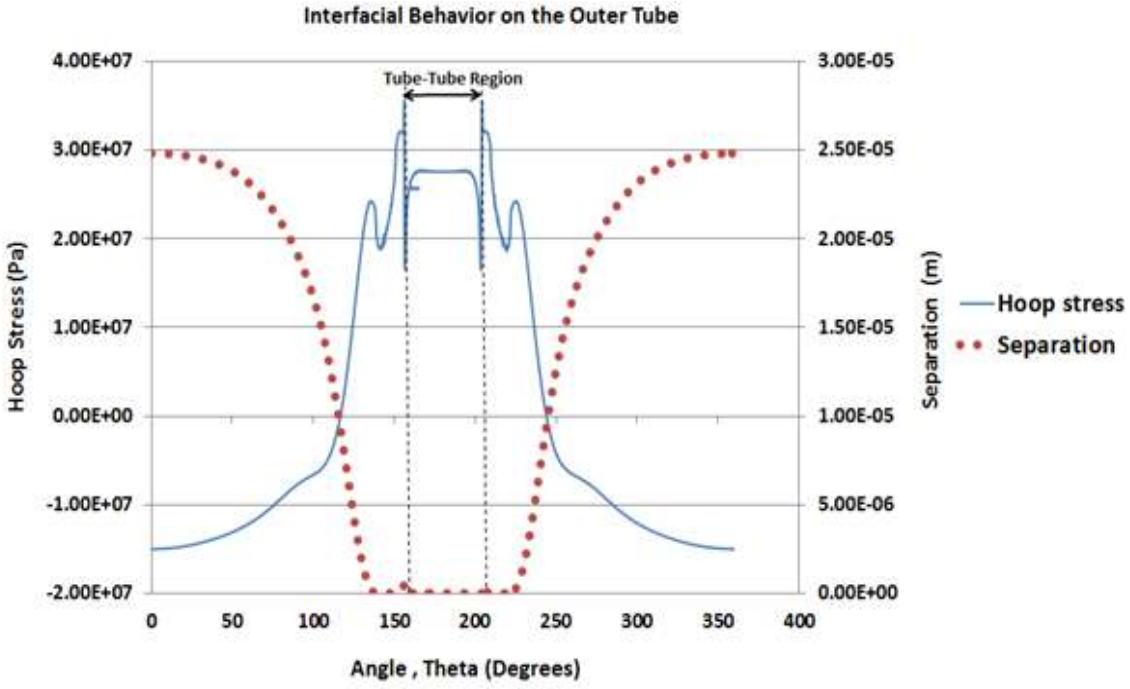

Figure 29. Hoop stress and separation on the outer tube inner surface.

Figure 29 also illustrates the circumferential variation of hoop stress along the inner surface of the outer tube. Between 0° and 120° the hoop stresses are compressive in nature. This is because the elements across the thickness of the outer tube resist the expansion of the inner surface due to radially outward heat flow inducing compressive stresses. Between 120° and 140° the hoop stresses move from being compressive to tensile. This can be attributed to the separation transition region and the foil making contact with the outer tube. The expansion of the

foil due to radially outward heat flow pushes the inner surface of the outer tube causing tensile hoop stresses to form in this region. Between 140° and 160° the tensile hoop stresses fluctuates as the foil pulls away from the recess. This behavior is symmetric from 200°-360°. The assembly hoop stress distribution contour is shown below in Fig 30.

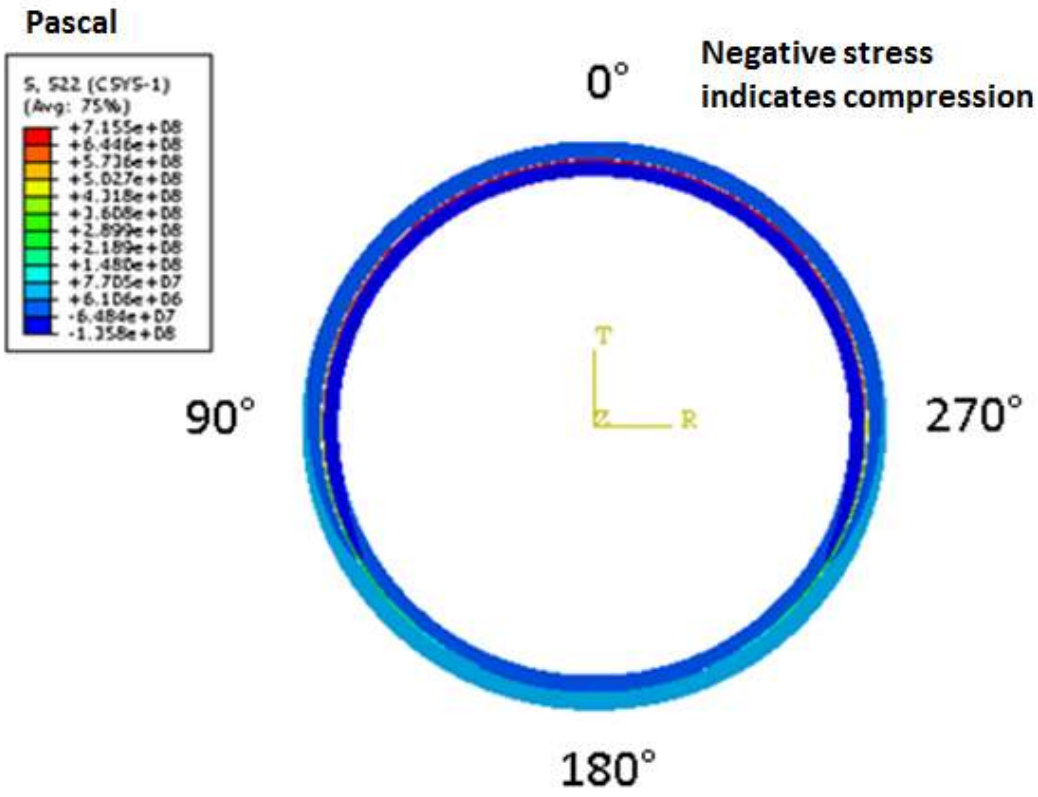

Figure 30. Assembly hoop stress contour for the non-uniform heating case

Figure 31 shows the temperature distribution along the circumference of the inner surface of the outer tube. From 0°-120° the temperature remains a constant in the uniformly heated region and begins to drop closer to the tube-tube location. The behavior is symmetric from 200°-

360°. Though the temperature drives the thermal stresses, Fig 29 illustrates that the separation at the interface influences the magnitude and behavior of the hoop stresses.

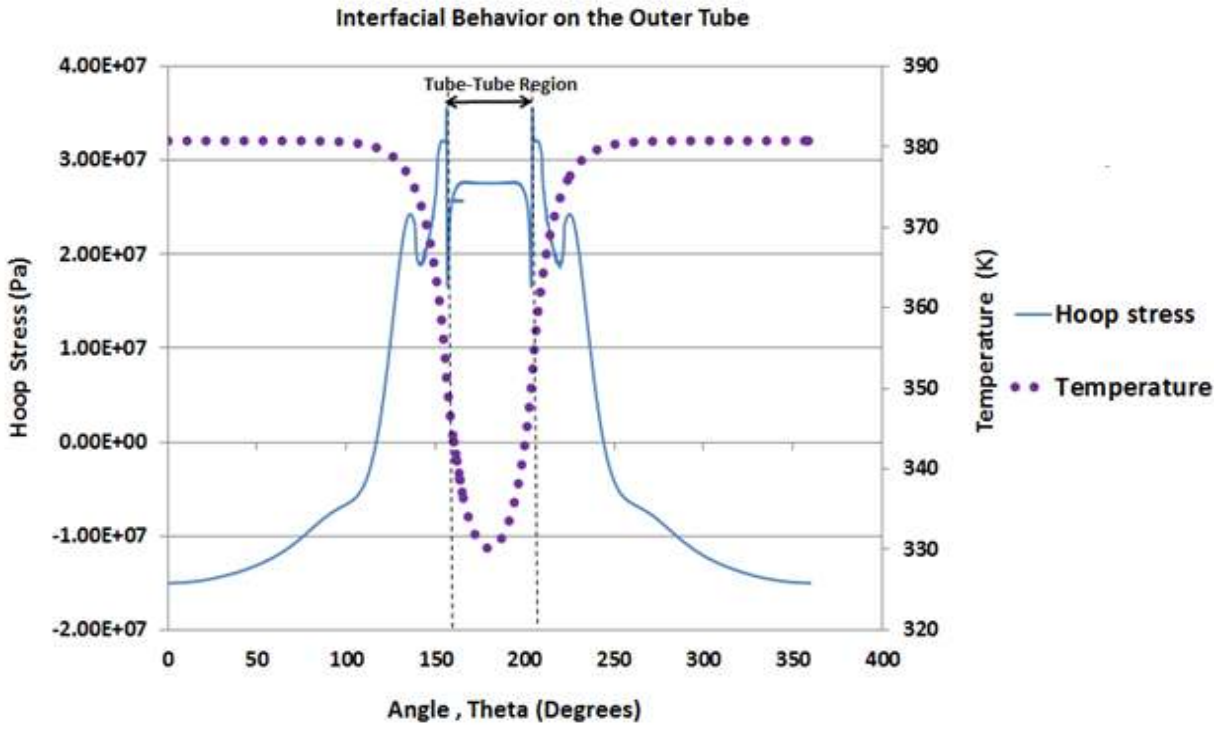

Figure 31.Hoop stress and temperature on the outer tube inner surface.

Figure 32 illustrates the contact pressure and separation along the circumference of the inner surface of the outer tube. From 0 ° onwards the contact pressure is zero when the separation is finite as shown in Fig 32. A finite contact pressure exists just before 150° as this is the region where the foil makes contact with the outer tube. There is a small region after 150° and 200° where the contact pressure is zero. This is because the foil completely pulls away from the recess on either side (Fig 28) and results in zero contact pressure. The huge spikes in contact

pressure are due to the edges of the recess which are regions of high stress concentration and hence result in high contact pressures. The behavior is symmetric from 200°-360°.

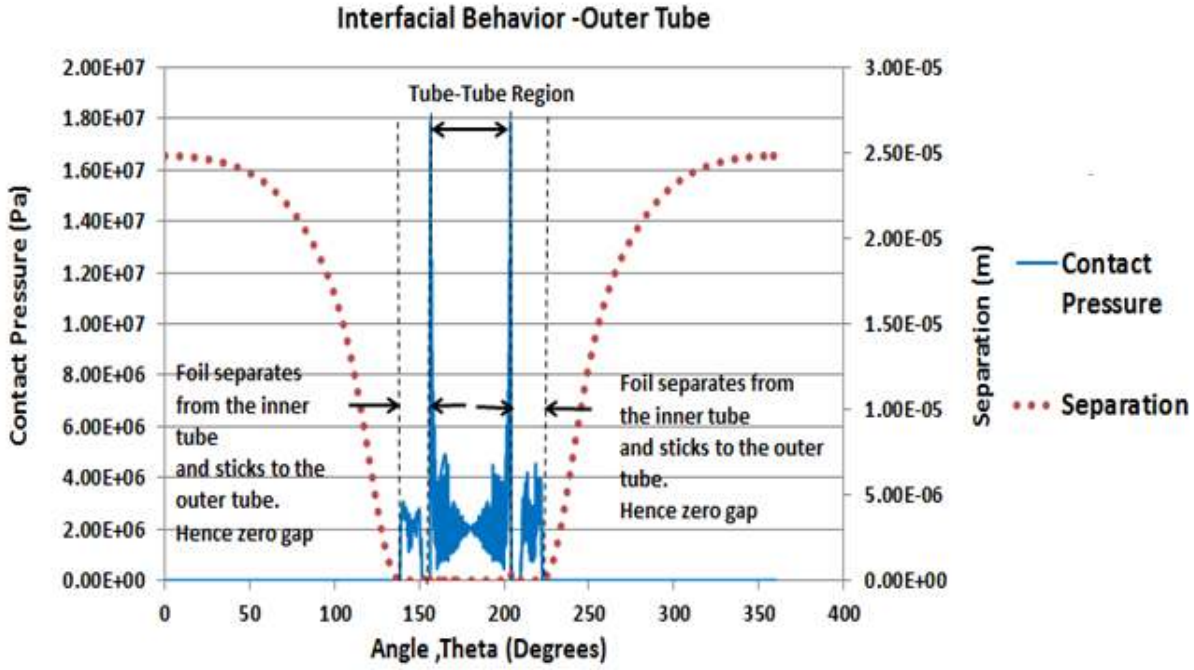

Figure 32. Contact pressure and separation on the outer tube inner surface

Figure 33 illustrates the hoop stress and temperature variation along the circumference of the outer surface of the inner tube. From 0°-120° the temperature remains a constant in the uniformly heated region and begins to drop closer to the tube-tube location. The behavior is symmetric from 200°-360°. The hoop stresses on the outer surface of the inner tube are compressive in nature due to radially inward heat flow and because the foil acts as a barrier to the free expansion of the outer surface of the inner tube. The magnitude of compressive hoop stress decreases from 0° towards the tube-tube region and this behavior is symmetric. This decrease in compressive stress results from the contact between the LEU foil and the inner tube

being reinforced and relaxed. Hence the magnitude of compressive hoop stress is maximum at 0° and 360° and decreases by an order of magnitude beyond the separation transition region.

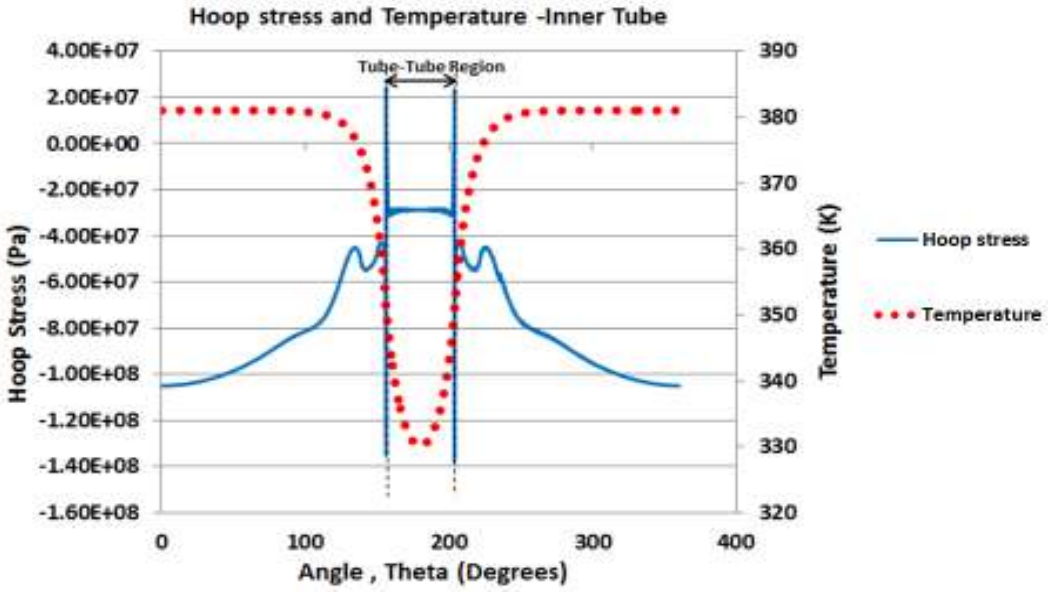

Figure 33.Hoop stress and temperature on the inner tube outer surface.

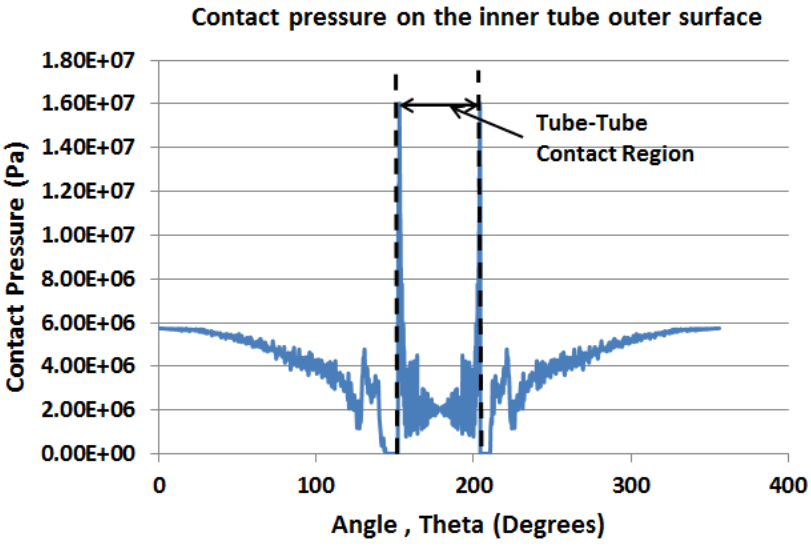

Figure 34. Contact pressure distribution on the inner tube for non-uniform heating.

The contact pressure at the interface of the inner tube and the LEU foil is illustrated in Fig. 34. There is a lot of noise in the contact pressure distribution on either side of the tube to tube region and this is due to the foil separating from the inner tube as illustrated in Fig. 28 and this results in nodal mismatch at the interface in the numerical model.

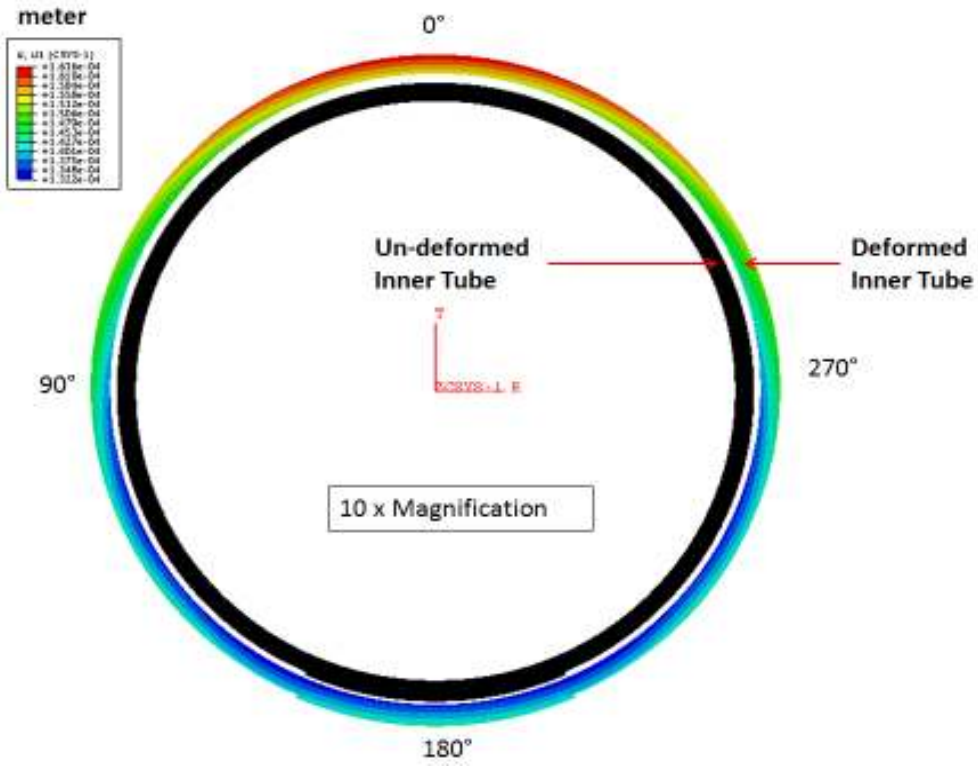

Figure 35. Deformed and un-deformed radial displacement contours of the inner tube

Figure 35 compares the radial displacement contours of the deformed inner tube with the un-deformed inner tube. The maximum radial displacement occurs at 0° on the inner tube. Comparing the deformed inner tube contour with a 10 x magnification to that of the un-deformed inner tube shows that the inner tube thermally expands and hence the inner and outer surfaces of the inner tube are radially displaced as illustrated in Fig 35.

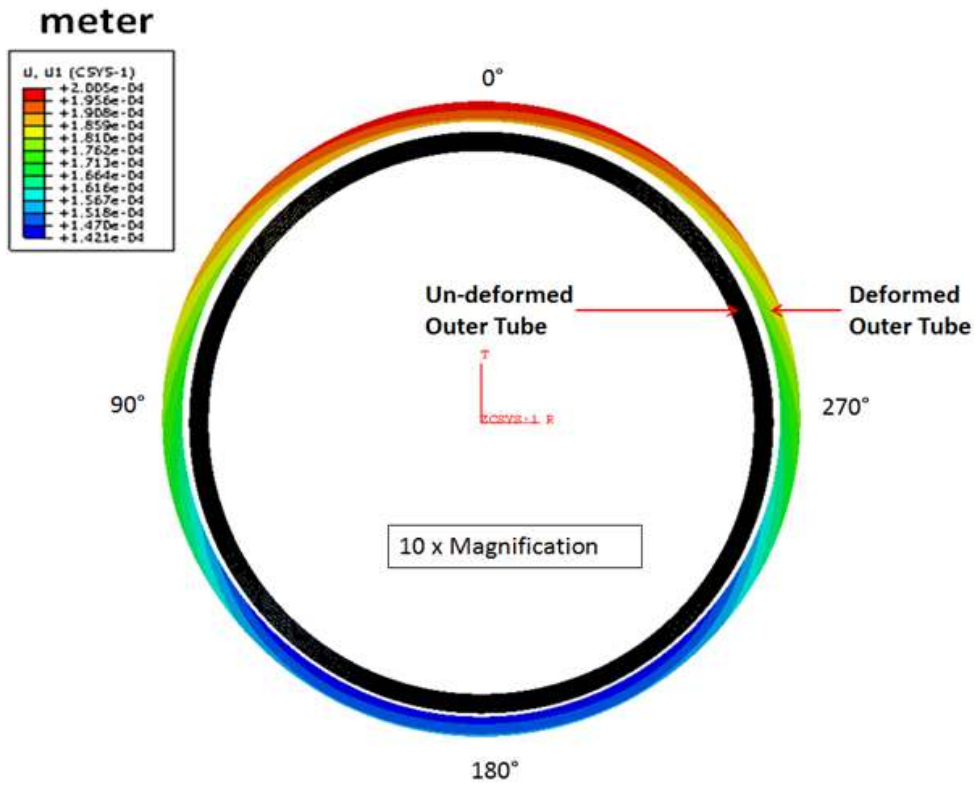

Figure 36. Deformed and un-deformed radial displacement contours of the outer tube

Figure 36 compares the radial displacement contours of the deformed outer tube to that of the original un-deformed shape. The maximum radial displacement occurs at 0° on the outer tube. At 0° the magnitude of radial displacement of the outer tube is greater than the inner tube. This is because the LEU foil is in perfect contact with the inner tube at this location (Fig.28 and Fig.29). Hence the foil acts as a barrier to the radial displacement of the inner tube at this location. Comparing the deformed outer tube contour with a 10 x magnification to that of the un-deformed outer tube shows that the outer tube thermally expands and hence the inner and outer surfaces of the outer tube are radially displaced as illustrated in Fig 36.

Figure 37 illustrates how the foil gets radially displaced. This deformed contour of the LEU foil clearly shows that the open ends of the foil are pulled inwards by ‘δ’ and this will result

in zero contact pressure on the inner and outer tubes in the regions where the foil exhibits this behavior. This is why the contact pressure on the edges of the recess is zero.

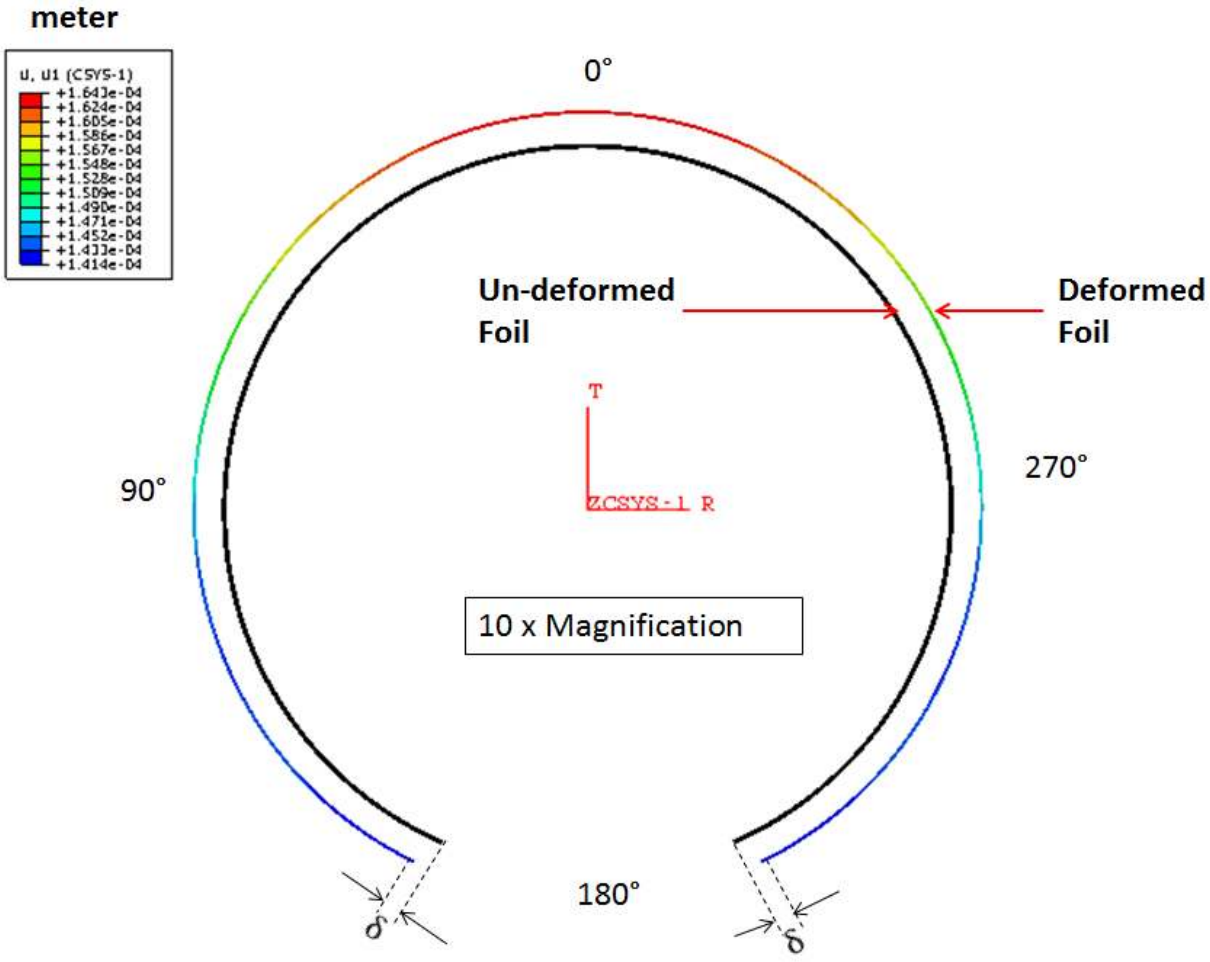

Figure 37. Deformed and un-deformed radial displacement contours of the LEU foil

The final deformed shape of the annular target assembly is illustrated in Fig 38 as a radial displacement contour plot with a 40 x magnification. A higher magnification was used to provide a clear picture of how the target would look after irradiation. The gap that opens up between the foil and the outer tube and the foil and the inner tube closer to the tube-tube contact region can be seen. From Fig 29 the maximum magnitude of this gap between the LEU foil and the outer tube is in the micrometer range. Experiments need to be performed to check if the thermal

contact resistance is significant for this magnitude of separation. Also, perfect contact is maintained in the tube-tube region at 180°. This coupled with the fact that the maximum magnitude of displacement of the outer tube at 0° is greater than that of the inner tube, the final shape of the target will be oval and not circular.

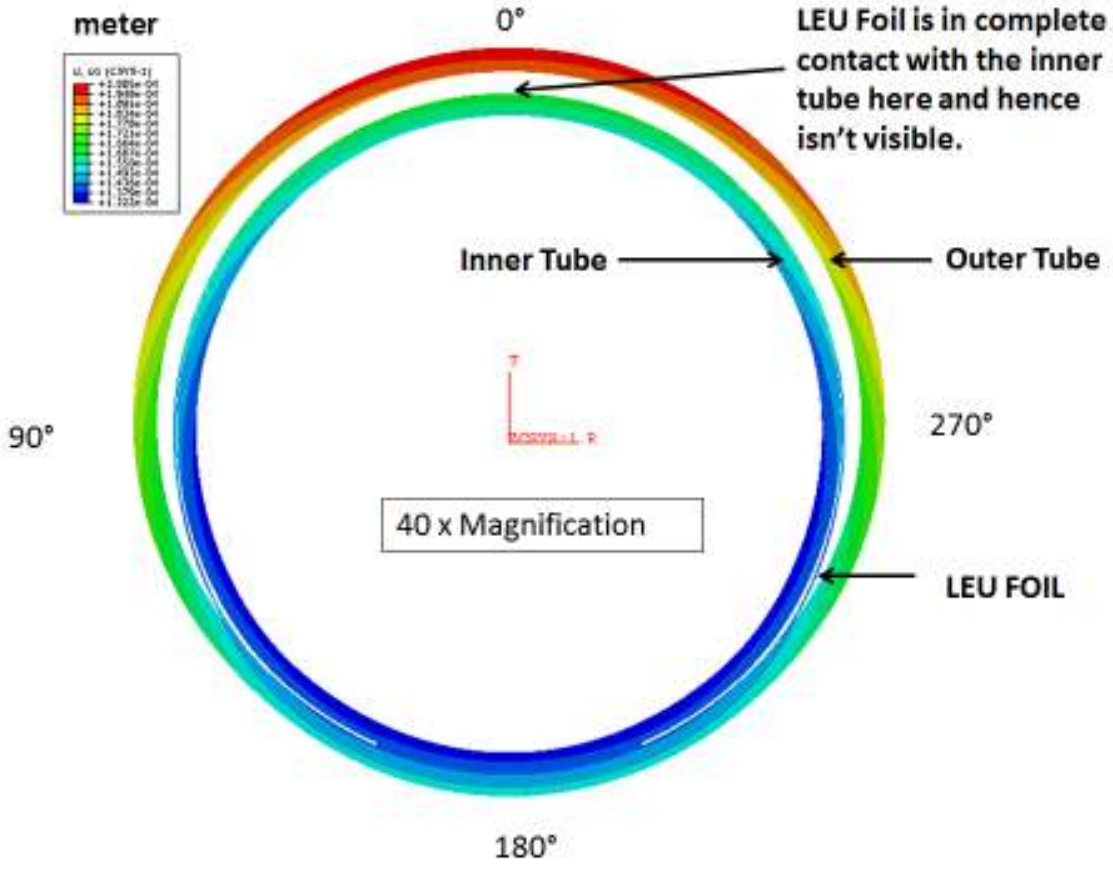

Figure 38. Final shape of the deformed annular target after irradiation (presented in terms of radial displacement contours of the assembly)

6.3 Uniform and Non-Uniform Heating Results Comparison

Recall that one goal behind developing a uniform heating model is to validate the non-uniform heating model (annular target with a recess and a foil of open cross section) by comparing the results of the uniformly heated region in the non-uniform heating model with that of the uniform heating model developed in Abaqus FEA and validated using analytical expressions as explained in section 6.2. It is expected that the values will be of the same order of magnitude.

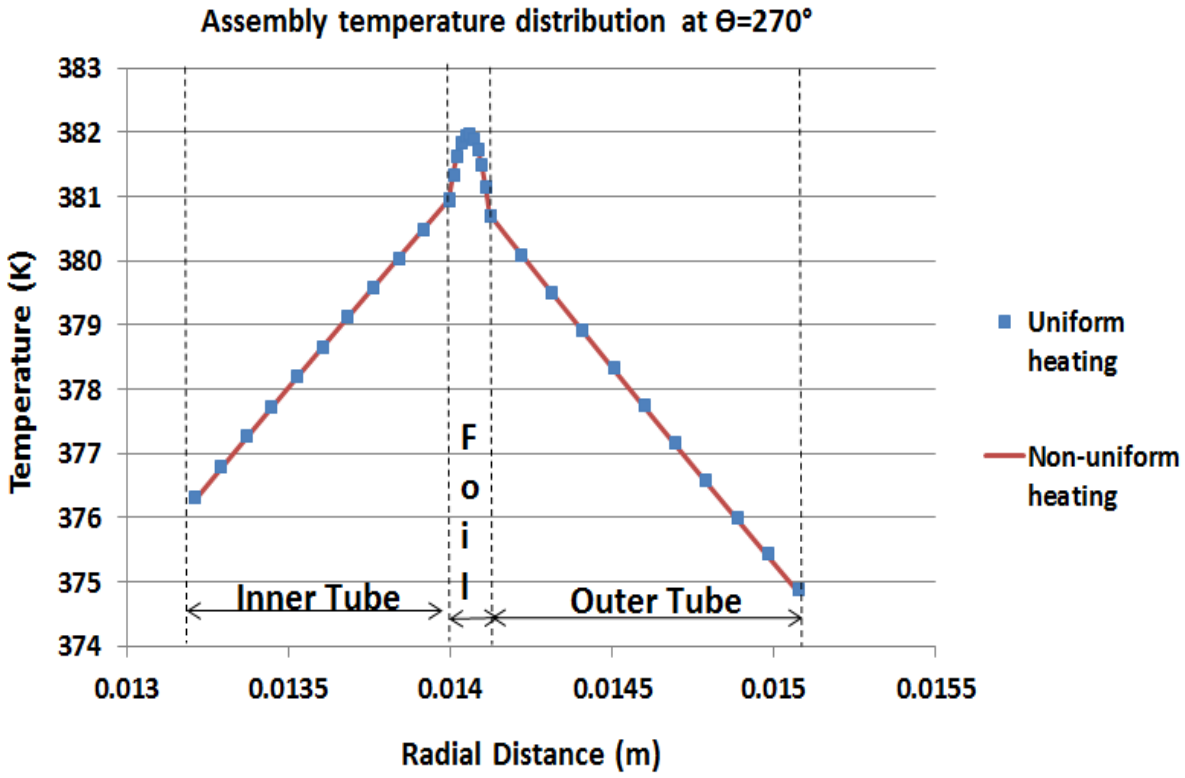

Figure 39. Comparison of the temperature distribution across the radius of the annular target assembly for the uniform and non-uniform heating conditions.

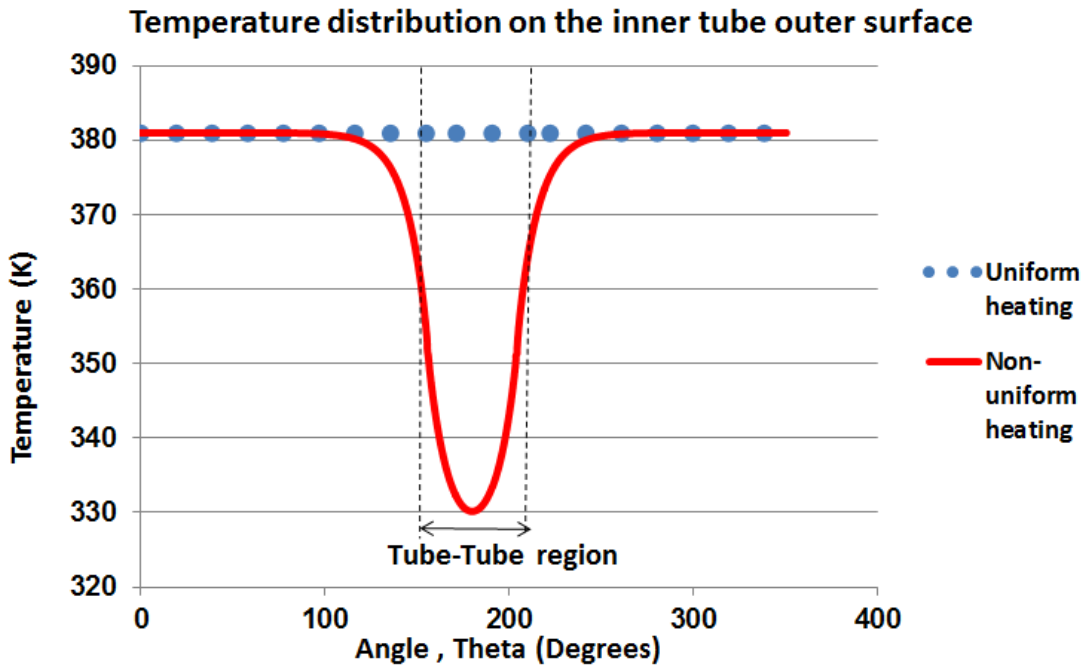

Figure 40. Comparison of the circumferential temperature distribution along the outer surface of the inner tube for uniform and non-uniform heating.

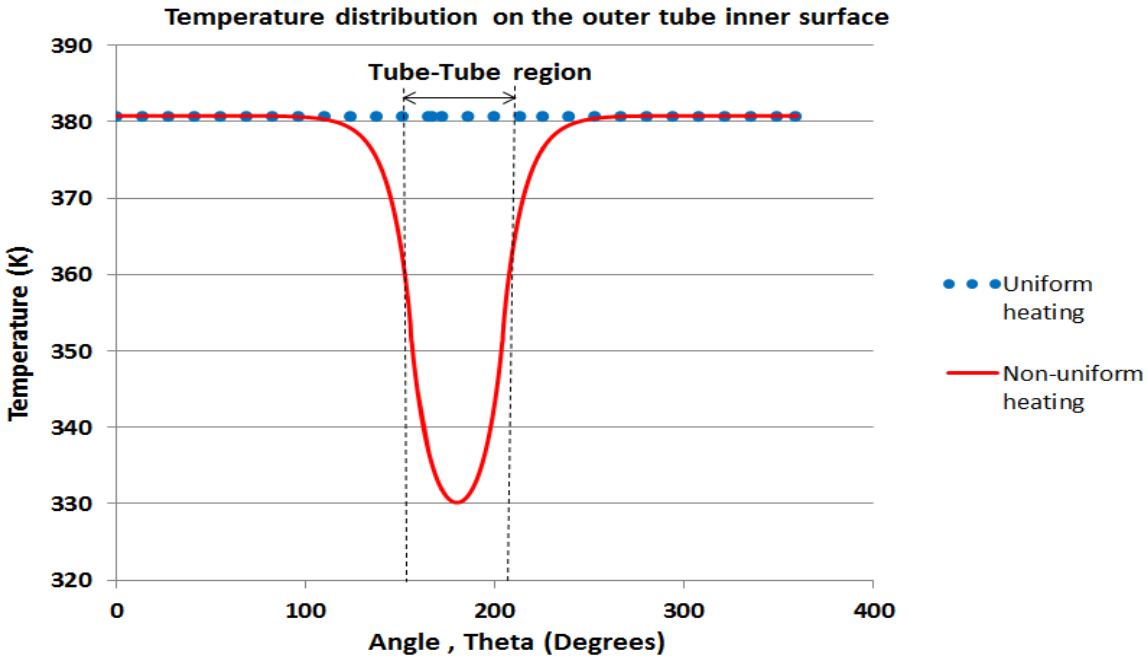

Figure 41. Comparison of the circumferential temperature distribution along the inner surface of the outer tube for uniform and non-uniform heating.

.

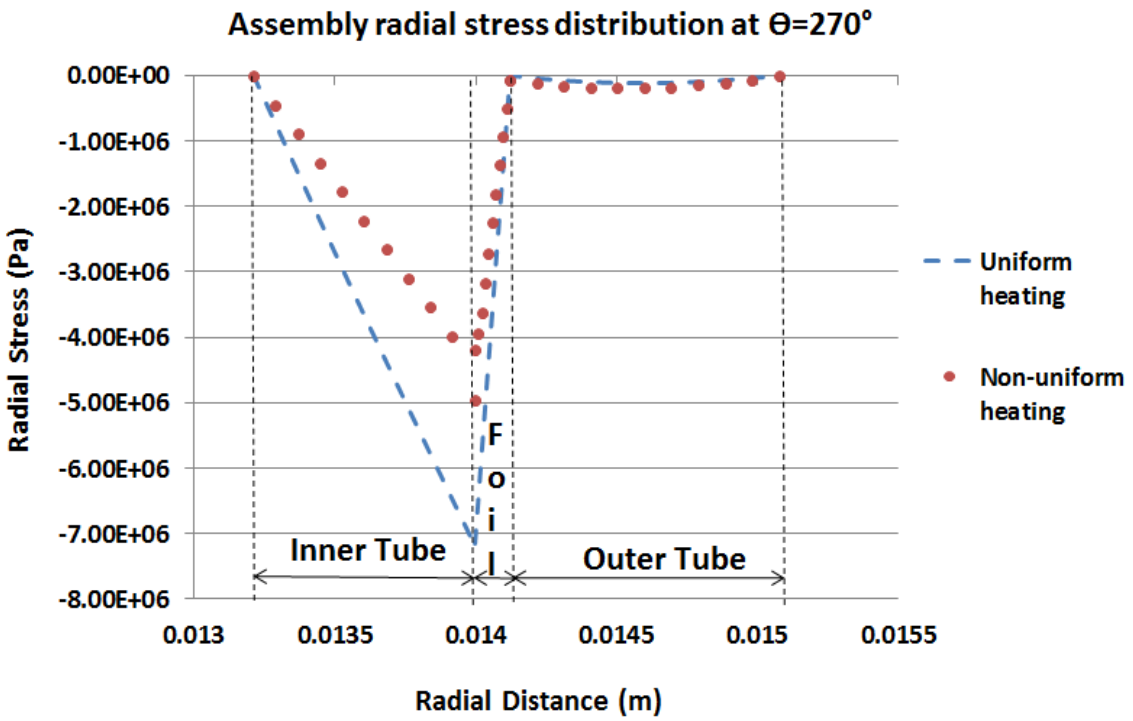

Figure 42. Comparison of the assembly radial stress distribution for the uniform and non-uniform heating conditions.

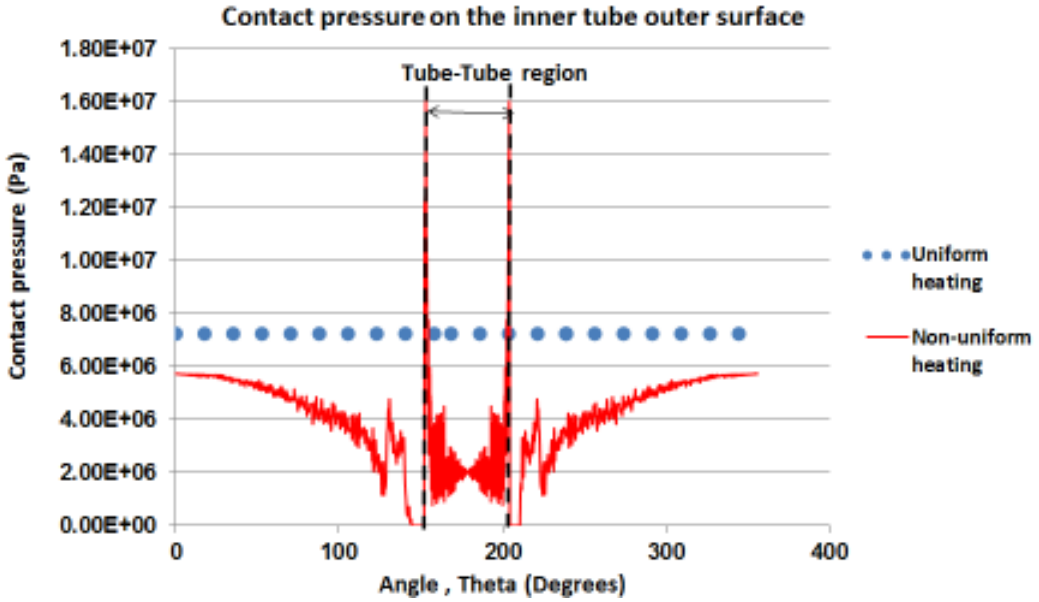

Figure 43. Comparison of contact pressure on the inner tube outer surface for uniform and non-uniform heating.

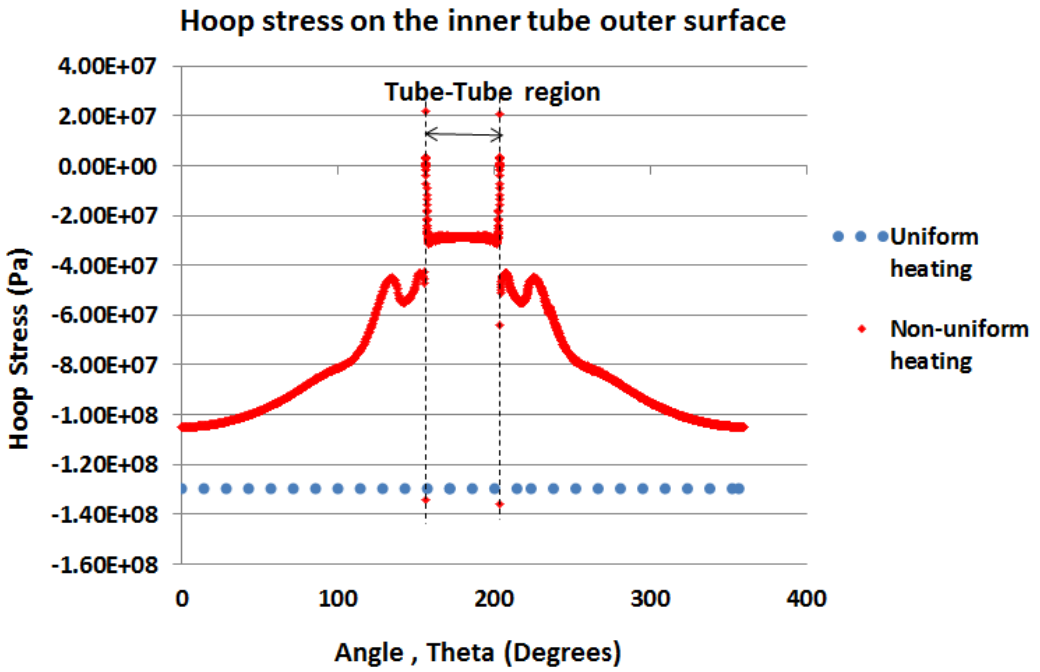

Figure 44. Hoop stress on the inner tube outer surface for uniform and non-uniform heating conditions.

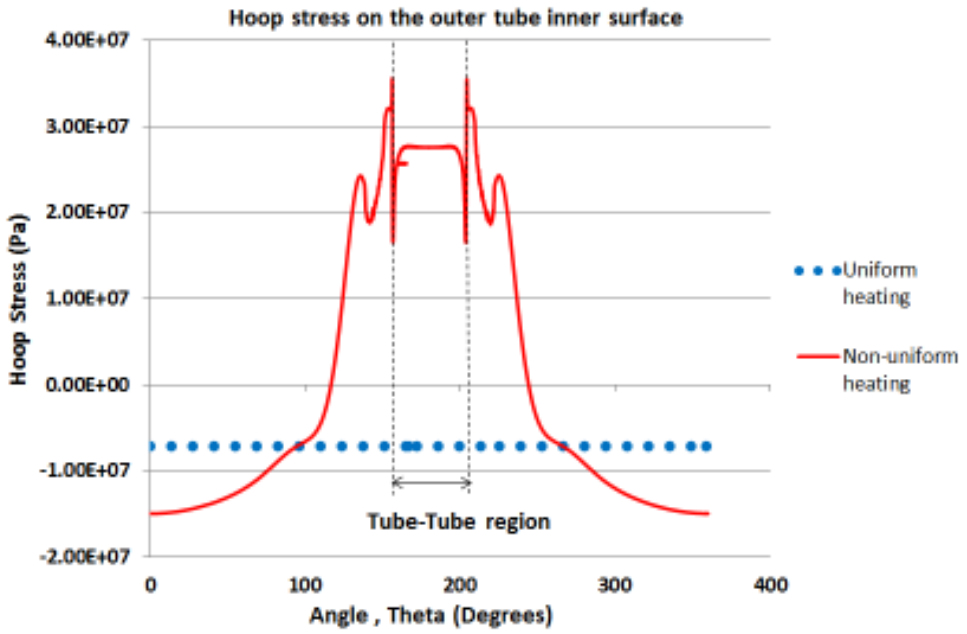

Figure 45. Comparison of hoop stresses on the inner surface of the outer tube for uniform and non-uniform heating conditions.

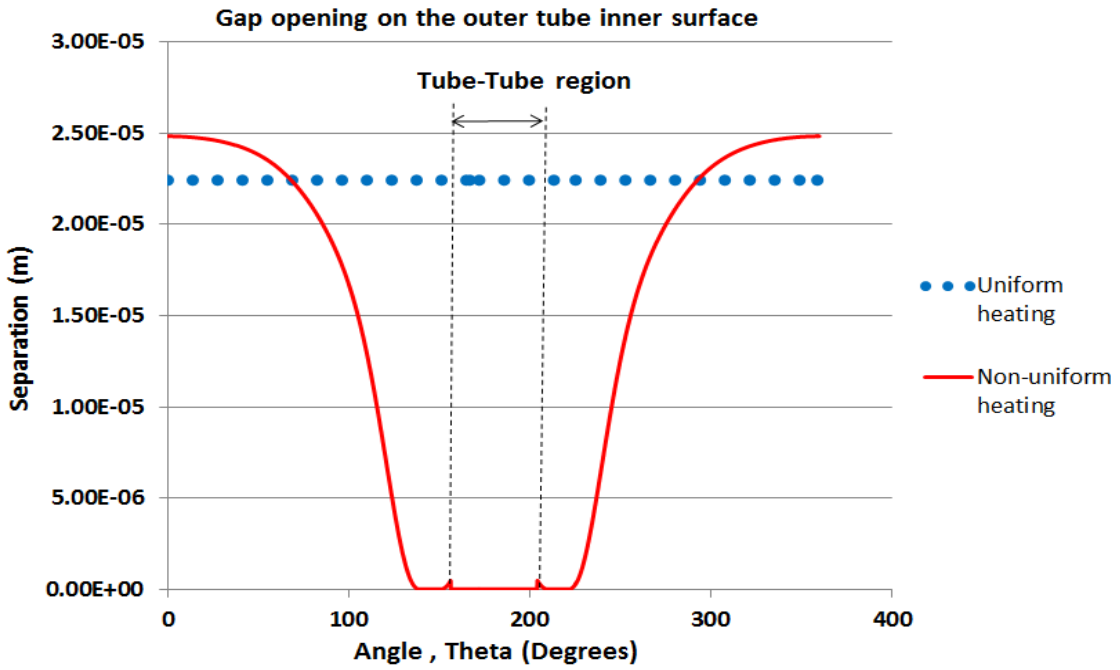

Figure 46. Comparison of the magnitude of separation between the foil and the outer tube for the uniform and non-uniform heating conditions.

Figures 39-46 provides a comparative study between the uniform and non-uniform heating conditions. The temperature distribution across the radius of the assembly at 270° is illustrated in Fig 39. In Fig 40, the uniform heating model under predicts the circumferential temperature on the outer surface of the inner tube by 0.02 % while in Fig 41 the uniform heating model under predicts the circumferential temperature on the inner surface of the outer tube by 0.21 %. The error is within 1% and there exists good agreement between the circumferential temperatures of the uniform and non-uniform heating models.

Figure 42 illustrates the comparison of the assembly radial stresses for the uniform and non-uniform heating cases at 270°. The uniform heating numerical model over predicts the compressive radial stress in the inner tube while it under predicts the compressive radial stress in the outer tube. The maximum error on the inner tube is 40 % and on the outer tube is 60 %. In

the uniformly heated region of the non-uniform heating model, the radial stresses across the target assembly are of the same order of magnitude as that of the uniform heating model.

The contact pressure comparison is illustrated in Fig 43. The uniform heating numerical model over predicts the contact pressure by 20 % when compared to the uniformly heated region of the non-uniform heating model. Also, the contact pressure in the uniformly heated region of the non-uniform heating model is of the same order of magnitude as the contact pressure from the uniform heating model.

The hoop stresses on the outer surface of the inner tube and on the inner surface of the outer tube are illustrated in Fig 44 and Fig 45 respectively. For the outer surface of the inner tube (Fig 44), the uniform heating model over predicts the compressive hoop stresses by 20 % as compared to the hoop stresses in the uniformly heated region of the non-uniform heating model. However, the uniform heating model under predicts the compressive hoop stresses on the inner surface of the outer tube by 40 %. In Figs 44 and 45 the compressive hoop stresses in the uniformly heated region of the non-uniform heating model is of the same order of magnitude as the compressive hoop stresses from the uniform heating model. Thus the temperature distribution in the circumferential and radial directions for the uniform and non-uniform heating cases are in good agreement with each other (in the uniformly heated region).The radial, hoop stresses on the inner and outer tubes ,the contact pressure and magnitude of separation between the foil and the outer tube are within the same order of magnitude as expected earlier. Hence the uniform heating model with a simple analytic solution can be used effectively for design and to evaluate the risk of target failure.

Chapter 7: Parametric Studies Using the Uniform Heating Model

Having shown in the previous section that the uniform heating model can be used for design and evaluation of target behavior, parametric studies were performed on the annular target using the uniform heating analytic model. The first section of this chapter will analyze the target behavior with the inner surface of the inner tube and the outer surface of the outer tube kept at 373 K throughout the analysis while the second section will present the target behavior with no restriction on wall temperature. The various operating conditions are: varying heat generation rates, varying heat transfer coefficient ratios and varying tube thickness ratios.

7.1 Reactor specific annular target parametric studies (T_{wall} at 373 K)

In the parametric studies presented in this section the inner surface of the inner tube and the outer surface of the outer tube are maintained at 373 K throughout the analysis. The first parameter to be varied was the LEU heat generation rate over a range of values presented in the Table 5.

Table 5. LEU heat generation rate parametric study

Dimensions of the 20g LEU Foil	LEU Heat Generation (x 10^{10} W/m^3)	Mass of Uranium (W/g)
Length: 0.100 m	1.6	762
Width : 0.0762 m	4.0	1905
Thickness : 125 µm	6.4	3048

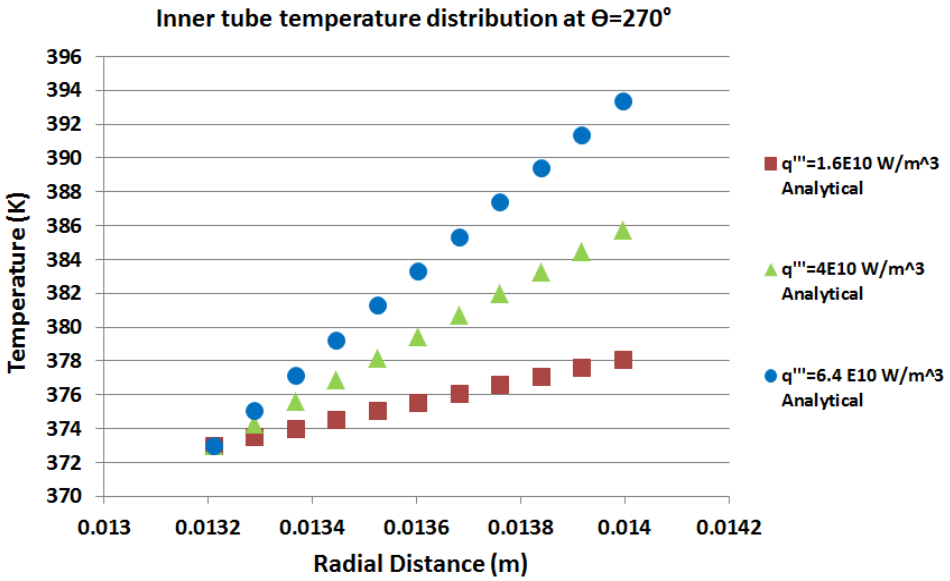

Figure 47. Inner tube temperature distribution for various LEU heat generation rates with T_{wall} at 373 K for uniform heating.

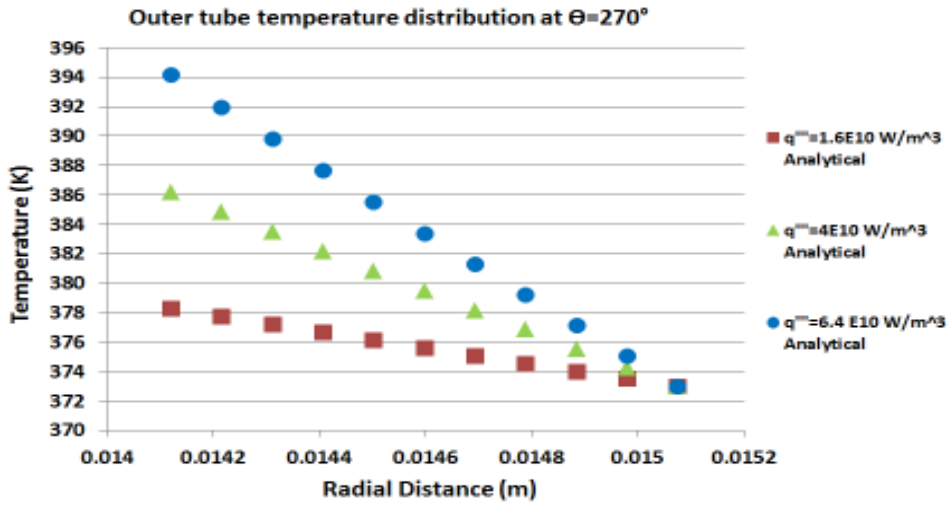

Figure 48. Outer tube temperature distribution for various LEU heat generation rates with T_{wall} at 373 K for uniform heating.

Figures 47 and 48 illustrate the temperature distribution, for various heat generation rates of the LEU, across the radius of the inner tube and outer tube respectively. An increase in heat generation rate will result in an increase in heat flux and a corresponding rise in temperature as

well. This behavior is well represented in Fig 47 and Fig 48. The temperatures originate at a common point (Fig 47) and converge at a common point in Fig 48. This is because the inner wall of the inner tube and the outer wall of the outer tube are maintained at 373 K.

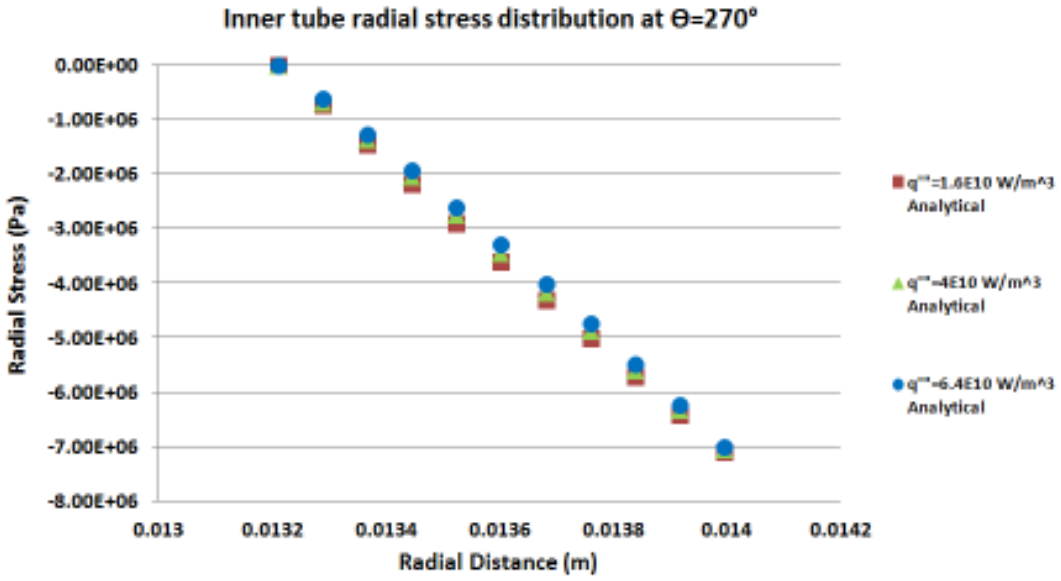

Figure 49. Radial stress distribution on the inner tube cladding for various LEU heat generation rates with T_{wall} at 373 K for uniform heating.

Figure 49 illustrates the radial stress distribution on the inner tube for varying heat generation rates of the LEU while Fig 50 illustrates the radial stress distribution on the outer tube cladding. Figure 49 shows that the radial stress at each nodal location decreases with increasing LEU heat generation rates. In reality one would expect the stresses to increase with increasing heat generation rates. The analytic model that was developed to predict the stresses in the inner tube can be used to explain this behavior. Basically the analytical model in Eqs (25-31) take into account the foil temperature to determine the thermal stresses in the inner tube. These foil temperatures are linked to the radial and hoop stresses through the constants C1 and C2. The

magnitude of these constants will dictate the contribution of the second term on the right hand side of Eq. (25). For a higher heat generation of the LEU, due to a greater temperature gradient, the negative magnitude of the second term in Eq. (25) is greater than for a comparatively lower heat generation rate. Hence this results in comparatively lower compressive radial stresses at higher heat generation rates. In the outer tube (Fig 50) the magnitude of stresses increases with increasing heat generation rates. This is because the stresses are driven primarily by the temperature gradients and a higher heat generation rate would imply higher temperature gradients in the target tubes.

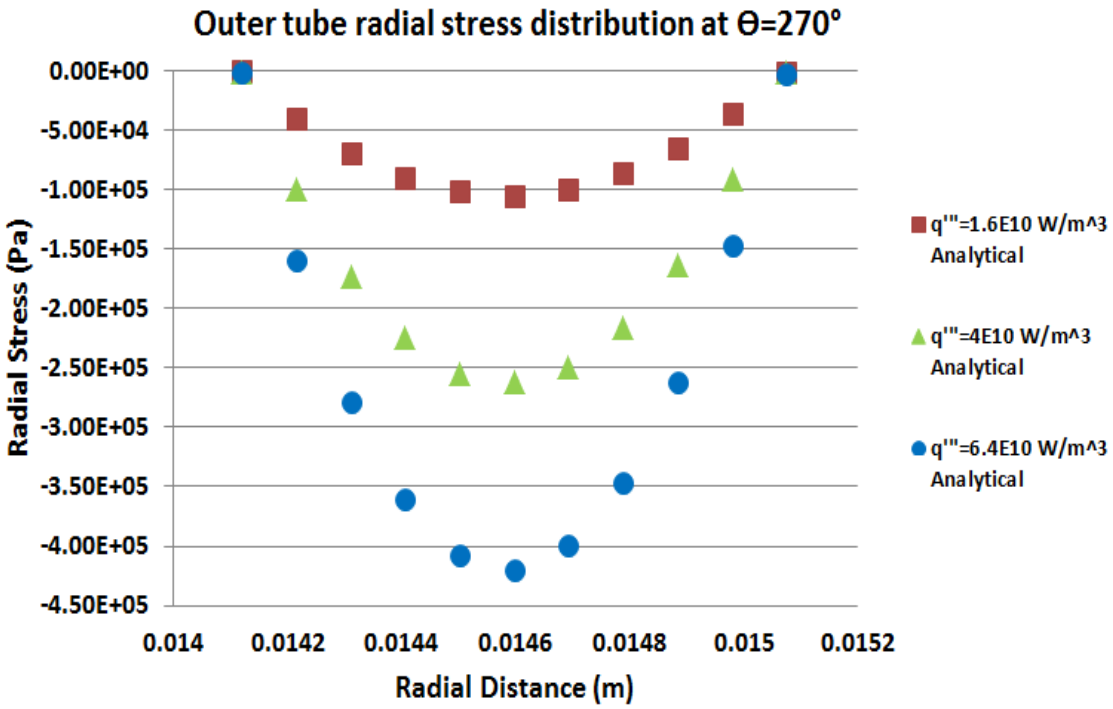

Figure 50. Radial stress distribution on the outer tube cladding for various LEU heat generation rates with T_{wall} at 373 K for uniform heating.

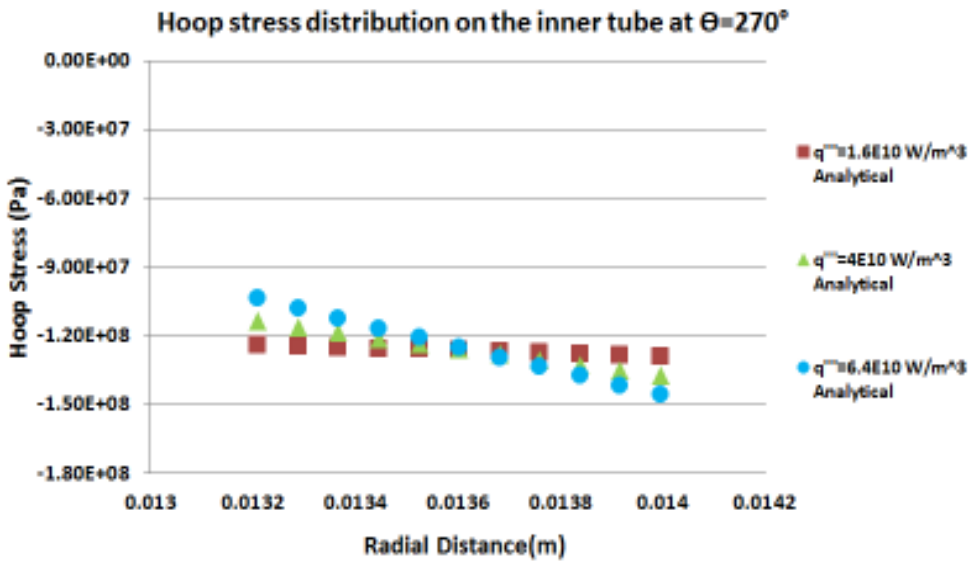

Figure 51.Hoop stress distribution on the inner tube cladding for various LEU heat generation rates with T_{wall} at 373 K for uniform heating.

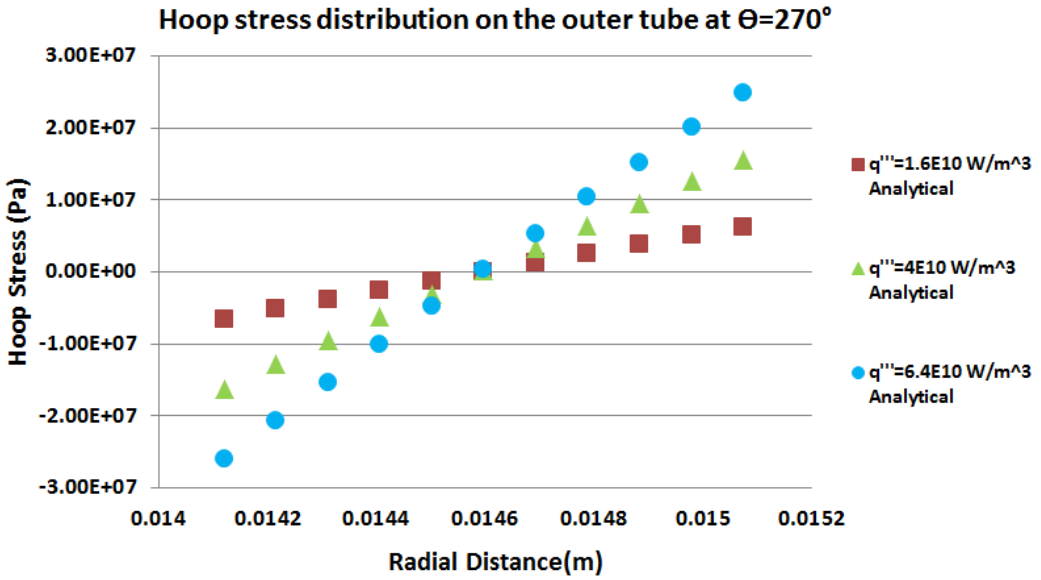

Figure 52. Hoop stress distribution on the outer tube cladding for various LEU heat generation rates with T_{wall} at 373 K for uniform heating.

Figures 51 and 52 illustrate the hoop stress distribution on the inner tube and outer tube respectively. In Fig 51 the magnitude of compressive stresses increases across the inner tube as there is an increase in temperature across the radius of the inner tube. Since the stresses in the inner tube are compressive in nature, a higher temperature will result in a higher compressive stress state. An increase in the LEU heat generation rate will increase the magnitude of temperature gradients (Fig 47) and results in a higher compressive stress. This is the behavior represented by Fig 51. Figure 52 shows that the maximum compressive hoop stress is induced on the inner surface of the outer tube. This is because the inner surface of the outer tube is the surface closer to the heat generating LEU and the temperature of the outer tube will be the highest at this point as illustrated in Fig 48.

The second parameter of interest is the heat transfer coefficient ratio. The rate of heat convection from the inner and outer surfaces of the inner and outer tubes respectively will depend on the dissipation of heat from these surfaces to the reactor coolant pool. Moreover the surface heat transfer coefficient will influence the wall temperature of the cladding as well. As it is a requirement that the cladding wall temperature should be within 373 K it was decided to look into the heat transfer coefficient ratios of the inner and the outer tubes that would maintain the wall temperatures at 373 K.

Applying newton's law of cooling to the inner surface of the inner tube, by keeping the wall temperature fixed at 373 K and the coolant temperature at 323 K, the heat transfer coefficient was found for the inner surface of the inner tube as 22122.60 W/m^2K. This is the heat transfer coefficient that would maintain the inner surface of the inner tube at 373 K. The outer heat transfer coefficient was determined based on the 'H' value presented in Table 6. Next the heat transfer coefficient of the outer wall of the outer tube was determined using the same

method and was found to be 17863.98 W/m^2K. This is the heat transfer coefficient of the outer wall that would maintain the surface at 373 K. The inner surface heat transfer coefficient was then determined based on the 'H' value presented in Table 6. Based on the above discussion the value of 'H' required to maintain the inner and outer wall at 373 K at the same time is found to be 1.24.

Table 7 shows the range of heat transfer coefficients used to perform a parametric study at a higher heat generation rate of the LEU. It is interesting to note here that the ratio of the heat transfer coefficient required to keep the inner wall at 373 K to that of the heat transfer coefficient required to keep the outer wall at 373 K is 1.24.

Table 6. Heat transfer coefficient ratio parametric study for $q'''=1.6 \times 10^{10}$ W/m^3

h_{in} (W/m^2K)	h_{out} (W/m^2K)	$H = h_{in} / h_{out}$
22122.60	44245.20	0.5
22122.60	29496.80	0.75
22122.60	22122.60	1
23759.09	17863.98	1.33
35727.96	17863.98	2

Table 7. Heat transfer coefficient ratio parametric study for $q'''=6.4 \times 10^{10}$ W/m^3

h_{in} (W/m^{2}K)	h_{out} (W/m^{2}K)	$H = h_{in} / h_{out}$
88524.40	177048.80	0.5
88524.40	118032.53	0.75
88524.40	88524.40	1
95073.72	71484	1.33
142968	71484	2

Figure 53 shows the variation of temperature at the outer and inner surfaces of the tubes for various heat transfer coefficient ratios while Fig 54 illustrates the same behavior at a higher heat generation rate of the LEU. A heat transfer coefficient ratio of below 1 implies that the outer surface heat transfer coefficient is greater than that of the inner surface while a heat transfer coefficient ratio greater than 1 implies a higher inner surface heat transfer coefficient.

In Fig 53 (based on Table 6) for a heat transfer coefficient ratio of 0.5 the outer surface of the inner tube is at a higher temperature than the inner surface of the outer tube. This is because the inner tube inner surface is at a comparatively lower heat transfer coefficient than the outer tube. Hence the temperature on the inner tube is higher. With increasing 'H' the difference gradually decreases and at H=2 the outer tube inner surface is at a higher temperature than the inner tube outer surface. This is because for H=2, the outer heat transfer coefficient is lesser than the inner heat transfer coefficient. This also explains why the inner tube inner surface is at a

lower temperature at H=2 than for H < 1. Figure 54 (based on H ratios in Table 7) illustrates the same behavior as Fig 53 at a higher LEU heat generation rate.

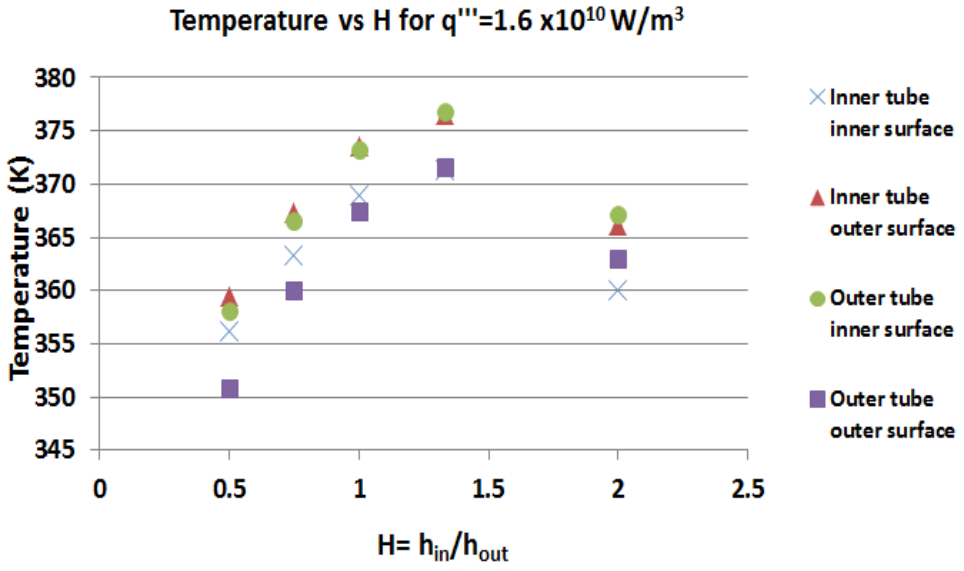

Figure 53. Variation of temperature at the inner and outer surfaces of the tubes with varying heat transfer coefficient ratios and T_{wall} at 373 K for uniform heating.

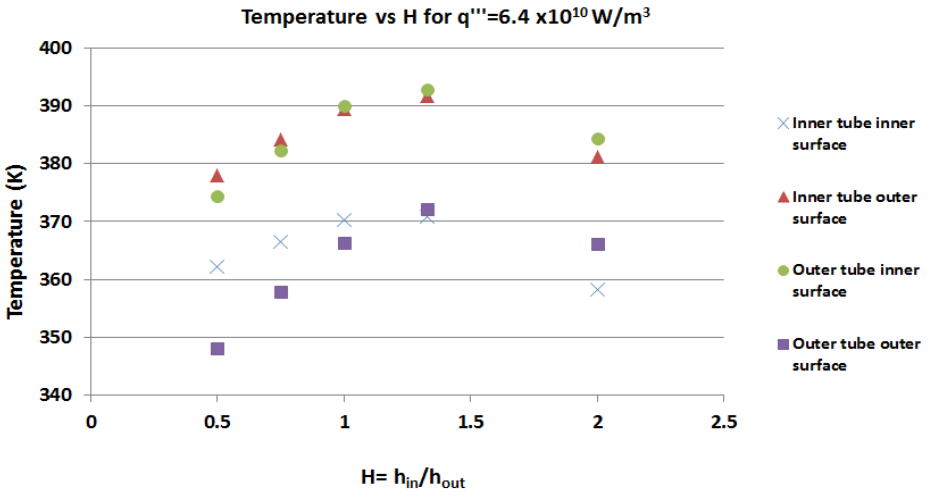

Figure 54. Variation of temperature at the inner and outer surfaces of the tubes at a higher LEU heat generation rate with varying heat transfer coefficient ratios. T_{wall} at 373 K for uniform heating.

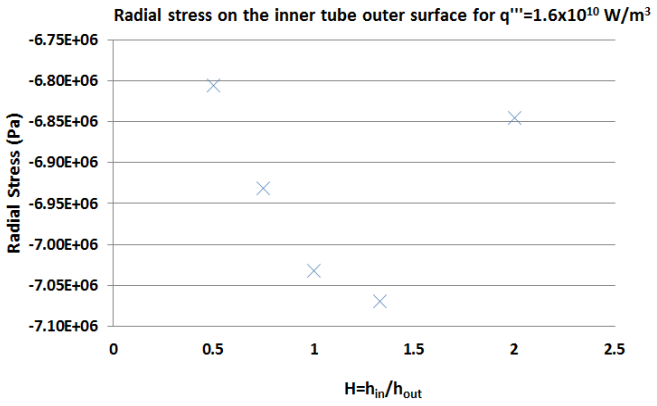

Figure 55. Radial stress on the inner tube outer surface with varying heat transfer coefficients and T_{wall} at 373 K for uniform heating

The radial stress behavior on the inner tube outer surface is illustrated in Fig 55. This behavior can be explained based on the radial temperature distribution on the inner tube outer surface as illustrated in Fig 53. The radial stress increases will increasing H ratios due to an increase in temperature. The maximum temperature on the inner tube outer surface occurs for a H ratio between 1 and 1.50. Since the temperatures drive the stresses, the maximum compressive radial stress occurs between H ratios of 1 and 1.50 as well. The same behavior at a higher heat generation rate of the LEU is illustrated in Fig 56.

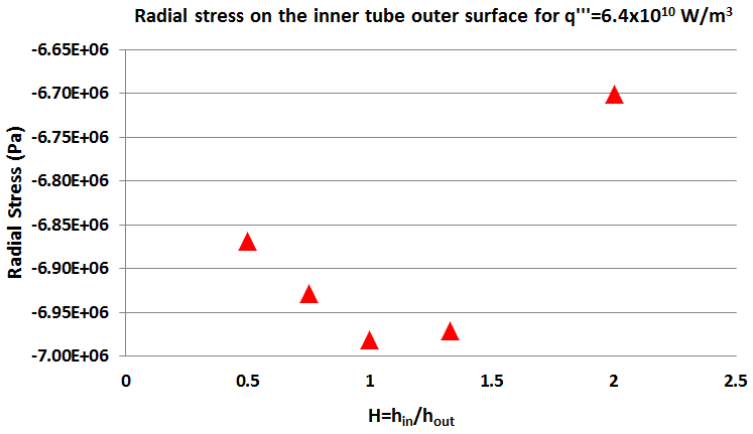

Figure 56. Radial stress on the inner tube outer surface at a higher LEU heat generation rate with varying heat transfer coefficients. T_{wall} at 373 K for uniform heating

The hoop stresses in the tubes for a lower and a higher LEU generation rate are illustrated in Figs 57 and 58 respectively. Similar to Fig 55 where the radial stress distribution is influenced by the temperature, the variation of hoop stresses with varying heat transfer coefficient ratios is dependent on the temperatures as well. The magnitude of compressive stresses will be the highest on the surface with higher temperature. From Fig 53 the maximum temperature on the inner tube outer surface occurs for a H ratio between 1 and 1.50 and also the temperatures on the inner tube outer surface are higher than on the inner surface of the inner tube (due to closer proximity to the heat generating LEU). Hence the magnitude of compressive hoop stresses on the inner tube will be maximum between H=1 and H=1.50 as illustrated in Figs 57 and 58.

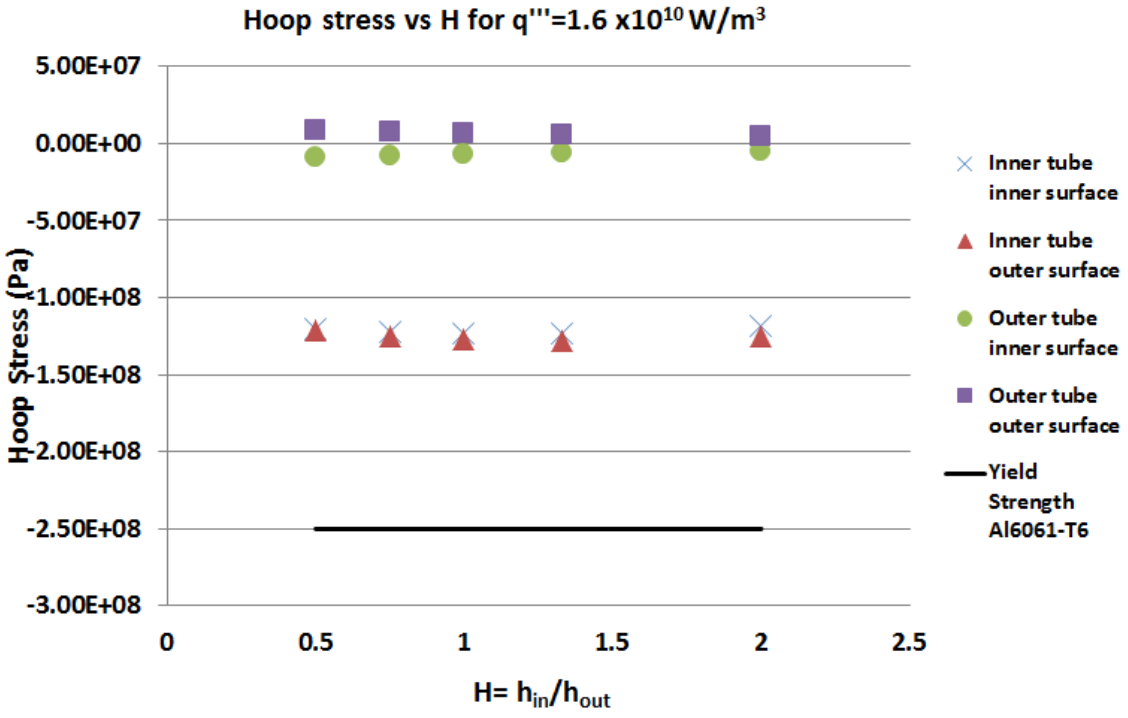

Figure 57. Hoop stress distribution in the tubes with varying heat transfer coefficient ratios and T_{wall} at 373 K for uniform heating

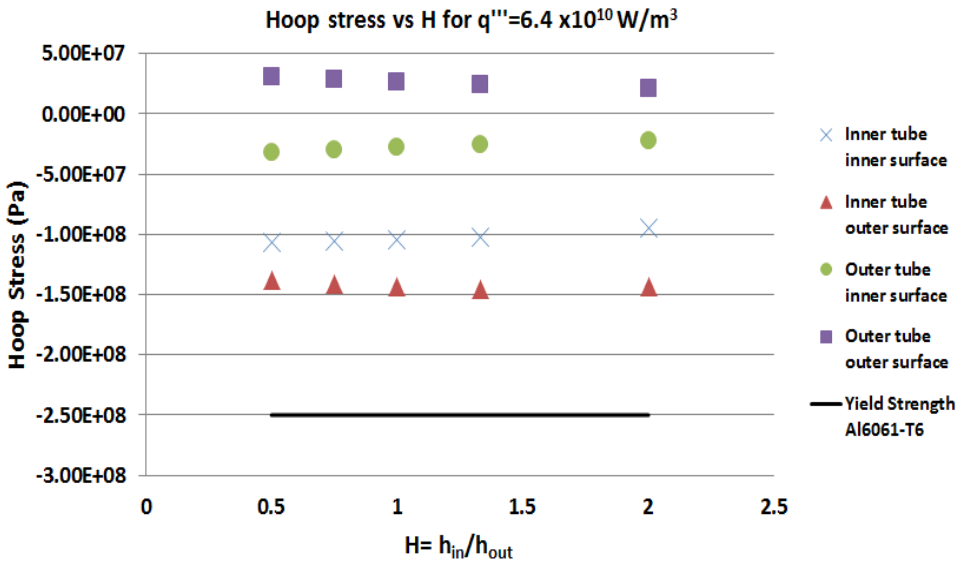

Figure 58. Hoop stress distribution in the tubes at a higher LEU heat generation rate with varying heat transfer coefficient ratios and T_{wall} at 373 K for uniform heating

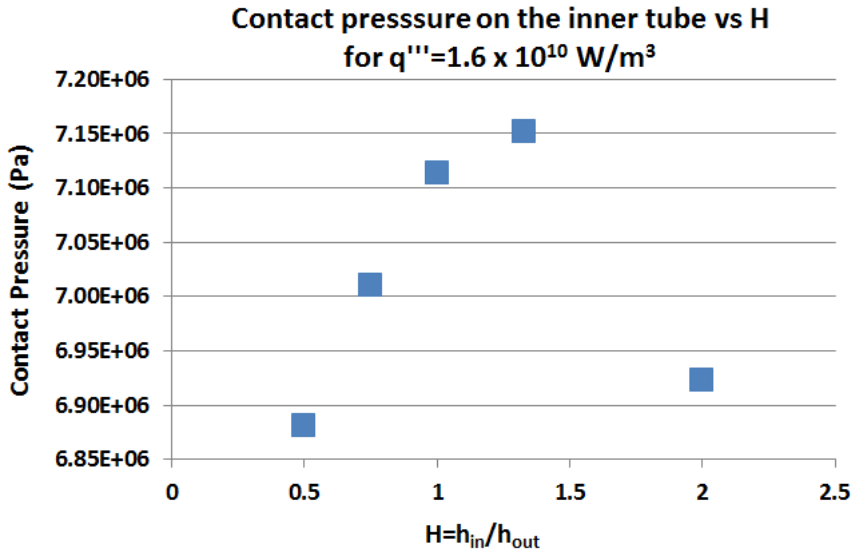

Figure 59. Effect of varying the heat transfer coefficient ratio on the contact pressure on the inner tube for the case of uniform heating with T_{wall} at 373 K

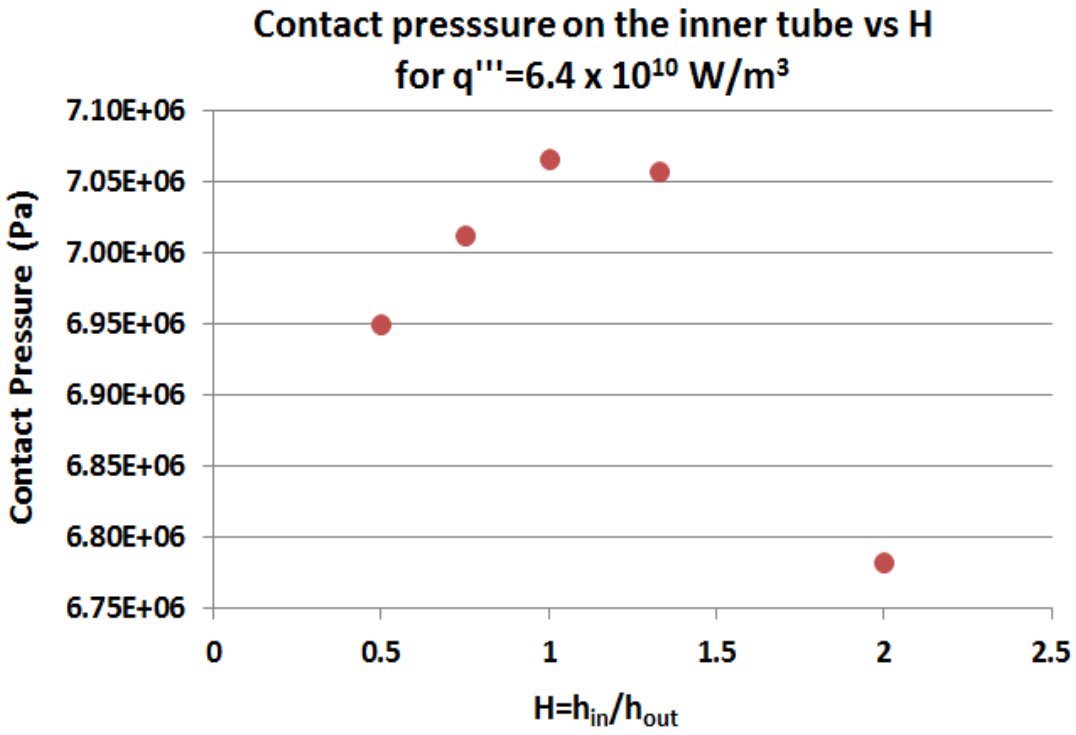

Figure 60. Effect of varying the heat transfer coefficient ratio on the contact pressure on the inner tube for the case of uniform heating with T_{wall} at 373 K for a higher LEU heat generation rate

Figures 59 and 60 illustrate the effect of varying heat transfer coefficient ratios on the contact pressure at the interface of the LEU and the inner tube cladding. The contact pressure increases with increasing H , due to an increase in temperature (Fig 53). For a heat transfer coefficient ratio of H=2, the contact pressure is lower. This is because of a higher inner heat transfer coefficient which causes more heat to be dissipated from the surface to the coolant pool. Figure 59 is based on the heat transfer coefficient ratios in Table 6 while Fig 60 is based on the heat transfer coefficient ratios in Table 7. Hence the magnitude of contact pressures cannot be compared between these plots.

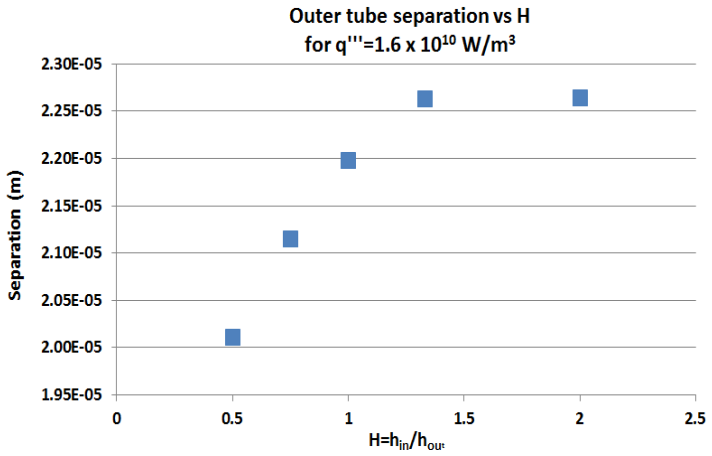

Figure 61. Effect of varying the heat transfer coefficient ratio on the gap opening between the LEU and outer tube for the case of uniform heating with T_{wall} at 373 K

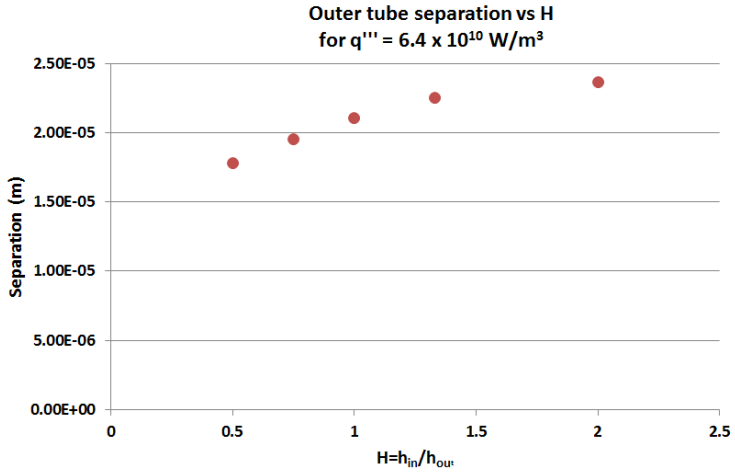

Figure 62. Effect of varying the heat transfer coefficient ratio on the gap opening between the LEU and outer tube for the case of uniform heating with T_{wall} at 373 K for a higher LEU heat generation rate

Figures 61 and 62 illustrate that the separation between the LEU foil and the outer tube cladding can be controlled by varying the heat transfer coefficient ratio. Greater separation will occur for H > 1. This implies that the inner heat transfer coefficient ratio is greater than the outer tube.

The final parameter of interest is the ratio of thickness of the inner tube to the outer tube. From Fig 52, the maximum compressive stress generated in the outer tube is about 30 MPa and this is within the yield strength of Aluminum 6061-T6. A comparison between Fig 52 and 53 shows that the magnitude of compressive hoop stress on the inner tube is higher than the compressive hoop stresses on the outer tube by an order of magnitude. Hence failure of the inner tube will dictate the failure of the target. Due to this it was decided to analyze the hoop stresses on the inner and outer surfaces of the inner tube. This tube thickness ratio study was carried out with the inner surface of the inner tube and the outer surface of the outer tube kept at 373 K. The thickness ratios were varied according to Table 8

Table 8. Tube thickness ratio study with T_{wall}=373 K

t_{in} x 10^{-4} (m)	t_{out} x 10^{-4} (m)	t_{in}/t_{out}
7.85	8.30	0.96
7.85	9.55	0.82
4.85	9.55	0.51
2.85	9.55	0.30
0.85	9.55	0.09

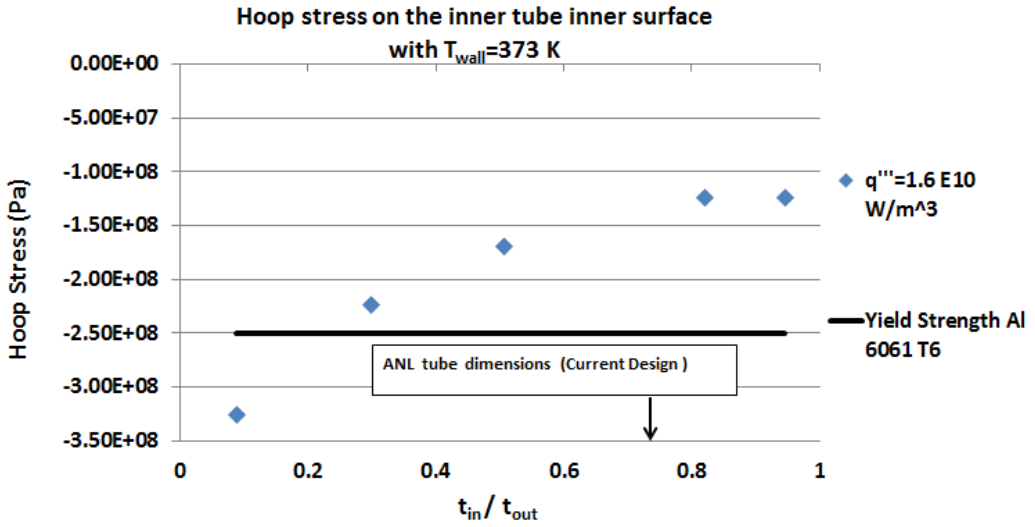

Figure 63. Variation of hoop stresses on the inner surface of the inner tube for the case of uniform heating with T_{wall} at 373 K

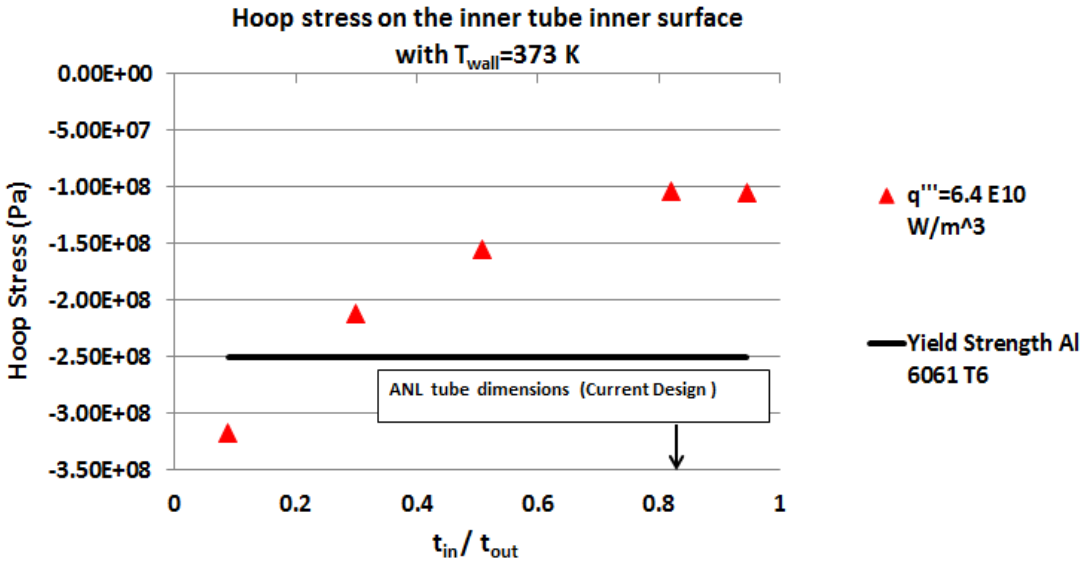

Figure 64. Variation of hoop stresses on the inner surface of the inner tube for the case of uniform heating with T_{wall} at 373 K for a higher LEU heat generation rate.

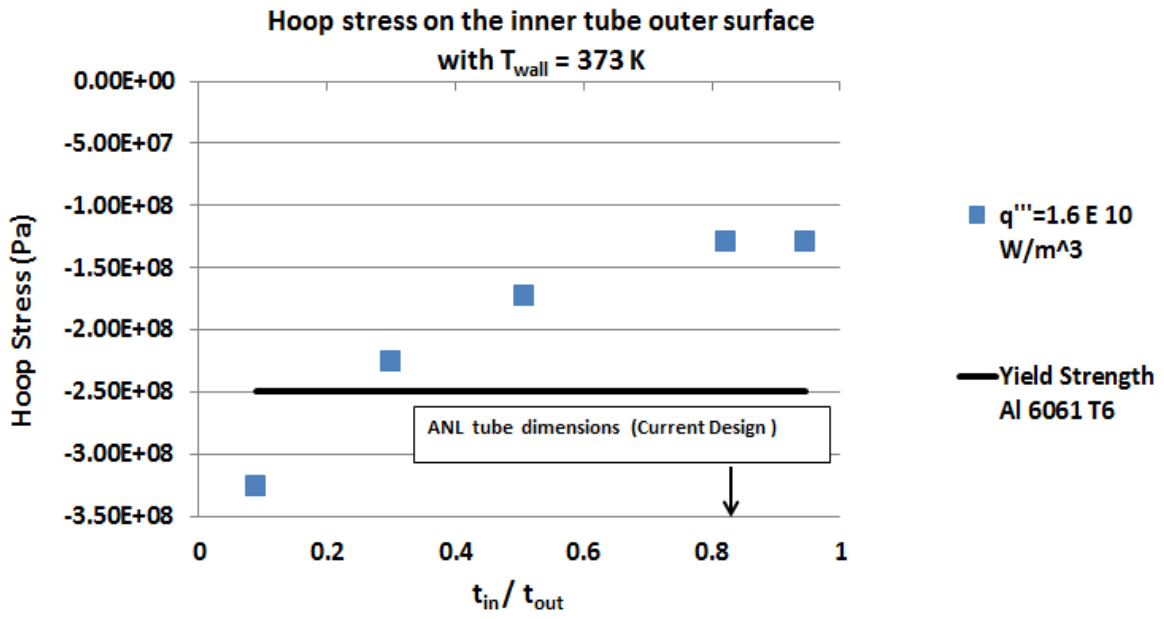

Figure 65.Variation of hoop stresses on the outer surface of the inner tube for the case of uniform heating with T_{wall} at 373 K

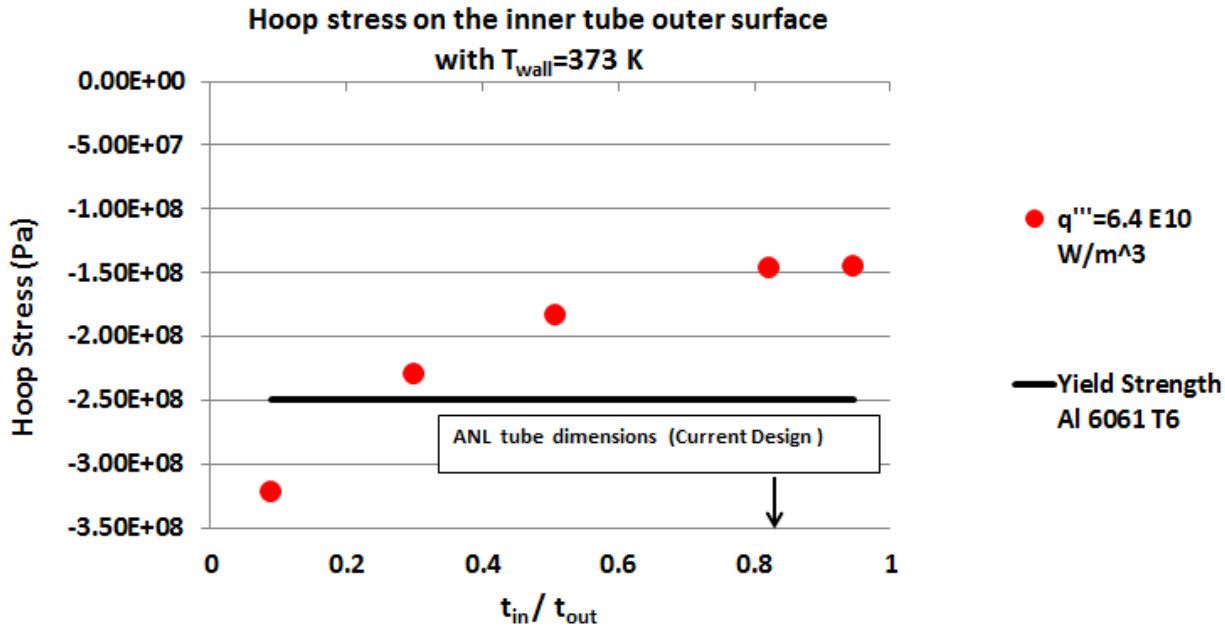

Figure 66. Variation of hoop stresses on the outer surface of the inner tube for the case of uniform heating with T_{wall} at 373 K for a higher LEU heat generation rate

Figures 63-66 illustrate the variation of hoop stresses with tube thickness ratio. For a given heat generation rate of the LEU the magnitude of compressive hoop stresses is greater for lower thickness ratios. This is because the thickness of the inner tube is much smaller than that of the outer tube. Hence for a given heat generation rate the magnitude of compressive hoop stresses will be greater. The tube thickness study plots also confirm that the annular target design of Argonne National Lab falls in the safe operating zone with a thickness ratio of 0.82.

7.2 General annular target studies (No restriction on wall temperature)

This section will focus on the general parametric studies with no restriction on wall temperature. Hence at high heat generation rates the surface temperature of the tubes might exceed 373 K resulting in boiling. Since the temperature gradients control the stresses in the tubes, the first parametric study involved varying the heat generation rate of the foil. The results are presented in terms of the LEU heat generation rates.

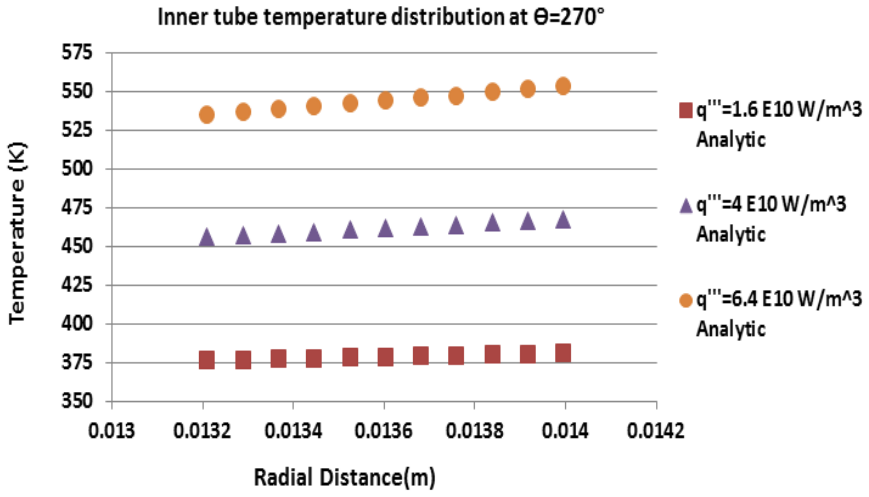

Figure 67. Inner tube temperature distribution for various LEU heat generation rates with $h_{in} = h_{out} = 19000$ W/m^{2}K for uniform heating.

The inner tube (Fig 67) and outer tube (Fig 68) temperature distribution plots shows that as the heat flux increases the temperature increases as well. This is in accordance with Fourier's law which provides a direct relation between the heat flux vector and the temperature gradient. The numerical results from Abaqus FEA are in good agreement with the analytical results obtained using a simple one dimensional thermal resistance network.

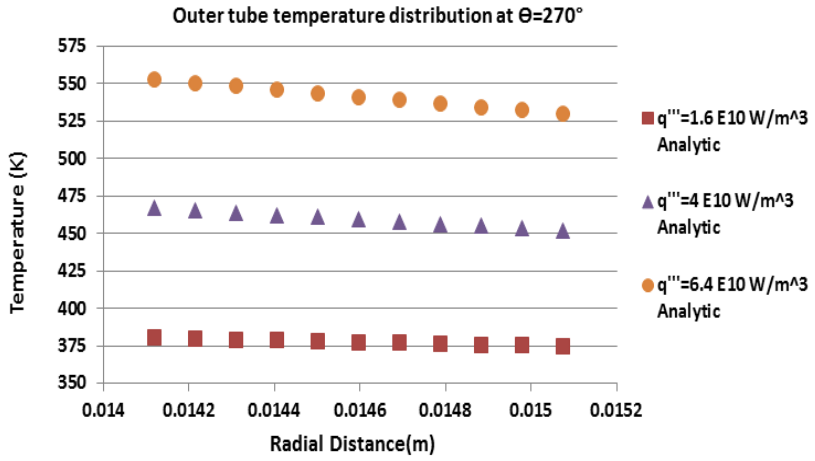

Figure 68. Outer tube temperature distribution for various LEU heat generation rates with $h_{in} = h_{out}$ =19000 W/m^{2}Kfor uniform heating.

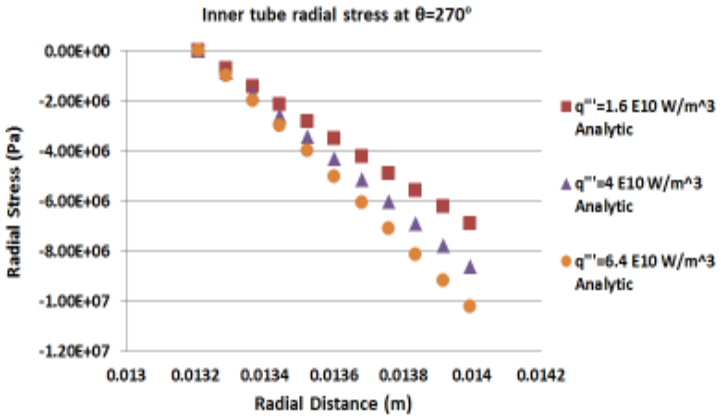

Figure 69. Radial stress distribution on the inner tube cladding for various LEU heat generation rates with $h_{in} = h_{out}$ =19000 W/m^{2}Kfor uniform heating.

Figure 69 shows the radial stress distribution on the inner tube for various heat generation rates of LEU while Fig 70 illustrates the radial stresses on the outer tube cladding. A common trend noticed here is that the magnitude of stresses increases with increasing heat generation rates. This is because the stresses are driven primarily by the temperature gradients and a higher heat flux would imply comparatively higher temperature gradients in the inner and the outer aluminum cladding.

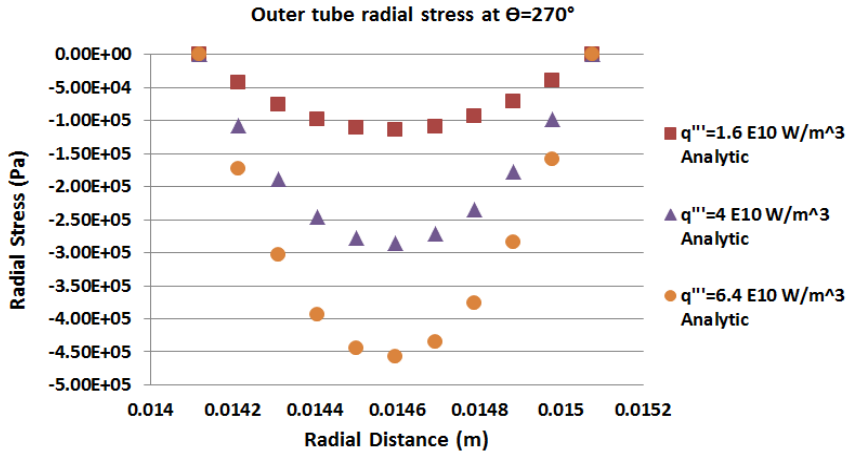

Figure 70. Radial stress distribution on the outer tube cladding for various LEU heat generation rates with $h_{in} = h_{out}$ =19000 W/m^{2}Kfor uniform heating.

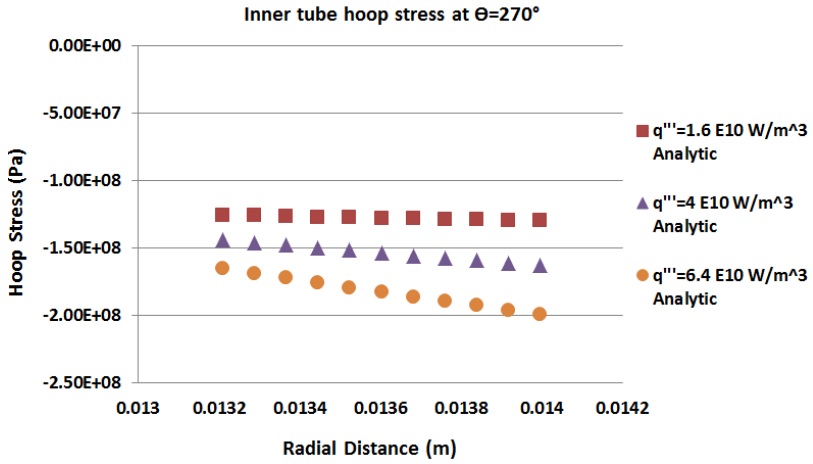

Figure 71. Radial hoop stress distribution on the inner tube for various LEU heat generation rates with $h_{in} = h_{out}$ =19000 W/m^{2}Kfor uniform heating.

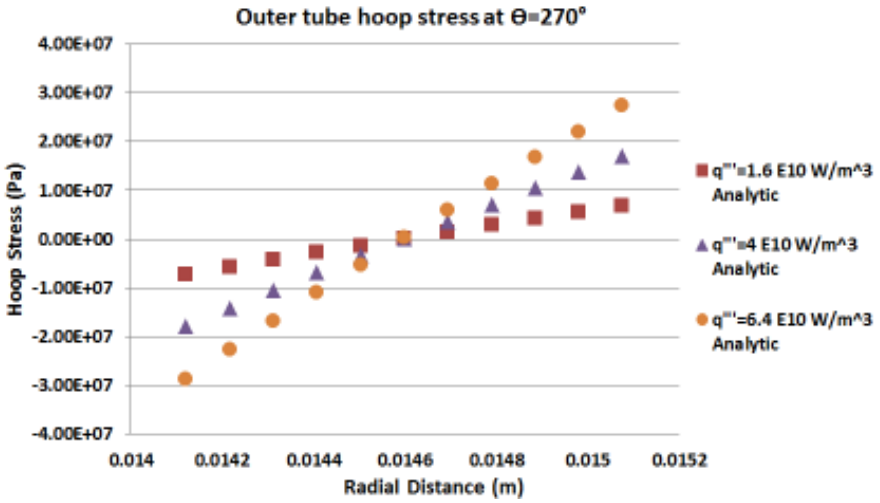

Figure 72. Radial hoop stress distribution on the outer tube for various LEU heat generation rates with $h_{in} = h_{out}$ =19000 W/m^{2}Kfor uniform heating.

Figures 71 and 72 illustrate the hoop stresses across the radius of the inner tube and outer tube respectively. As explained earlier the hoop stresses across the radius of the outer tube change from being compressive to tensile due to the expansion of the inner surface being resisted by the outer surface and in expanding the inner surface tries to push the outer surface thus generating tensile stresses. The stresses are compressive on the inner tube due to the direction of heat flow which influences the way in which the inner and outer surfaces of the inner tube expands.

The second parameter of interest is the heat transfer coefficient. Since coolant flows through the inner tube and along the outer tube, the heat is transferred from the outer surfaces by Newton's law of cooling which directly relates the heat flux to the surface heat transfer coefficient. Hence, for a given heat flux if the heat transfer coefficient varies, the temperature gradient varies as well. Since the thermal expansion of the tubes and stresses are controlled by the temperature gradients it was decided to analyze the effect of varying the ratio of heat transfer

coefficients and determine its effect on the stresses , temperature and the contact pressure on the inner tube. A parametric study was carried out based on Table 9.

Table 9. Heat transfer coefficient parametric study

h_{in} (W/m^2K)	h_{out} (W/m^2K)	$H=h_{in}/h_{out}$
9500	19000	0.50
14250	19000	0.75
19000	19000	1
19000	14250	1.33
19000	9500	2.0

Figure 73 shows the variation of temperature at the outer and inner surfaces of the tubes for various heat transfer coefficient ratios while Fig 74 illustrates the same behavior at a higher heat generation rate of LEU. A heat transfer coefficient ratio below 1 implies that the outer surface heat transfer coefficient is greater than that of the inner surface while a heat transfer coefficient ratio greater than 1 implies a higher inner surface heat transfer coefficient. Figures 73 and 74 shows that as the heat generation rate increases, for a given heat transfer coefficient ratio, the magnitude of temperature at a given location is comparatively larger. Also, when the inner surface of the inner tube is at a lower heat transfer coefficient than the other tube, then the outer surface of the outer tube is at a higher temperature than the inner surface of the inner tube. This is due to an inverse relationship that exists between the heat transfer coefficient and the temperature gradient. For a given heat flux, a lower heat transfer coefficient will result in a higher temperature gradient as compared to when a higher heat transfer coefficient exists. At a heat transfer coefficient ratio of 1 (H=1) the inner tube inner surface is at a higher temperature

than the outer tube outer surface. This is because the surface area of the inner tube is smaller compared to that of the outer tube. Hence for a given heat flux and heat transfer coefficient, a smaller area will result in a larger temperature gradient.

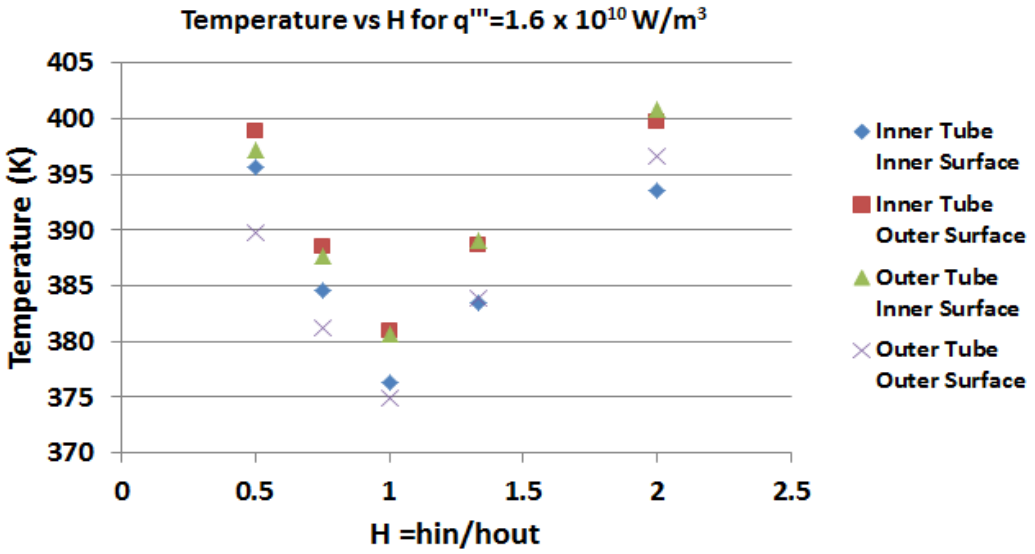

Figure 73. Variation of temperature at the inner and outer surfaces of the tubes with varying heat transfer coefficient ratio for uniform heating.

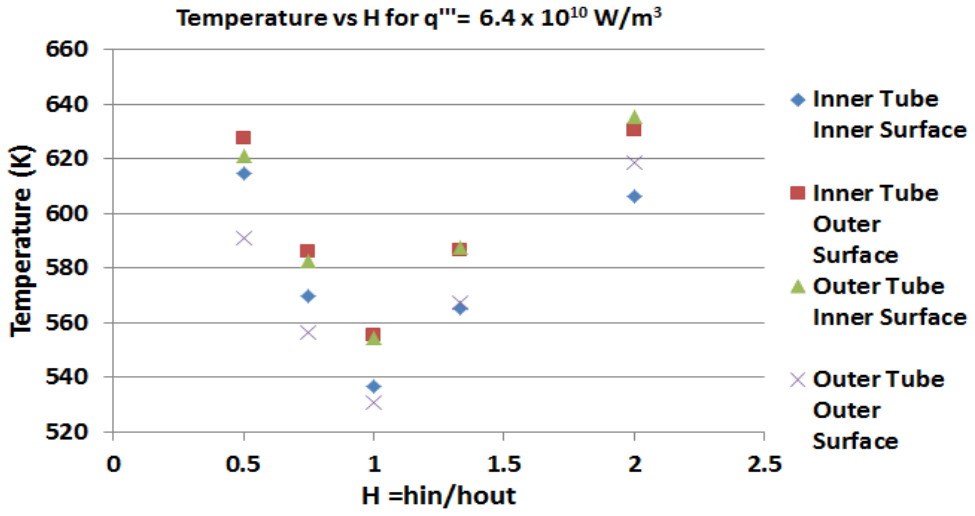

Figure 74. Variation of temperature at the inner and outer surfaces of the tubes at a higher LEU heat generation rate with varying heat transfer coefficient for the case of uniform heating.

Figures 75 and 76 illustrate the effect of varying the heat transfer coefficient ratio, on the radial stresses on the outer surfaces of the inner tube. The inner surface of the inner tube is free from any loading and hence the radial stress on this surface is zero. Similarly the inner and outer surfaces of the outer tube are free from external loading as the outer tube separates from the foil. As a result the radial stresses on these surfaces are zero as well. On comparing Figs 75 and 76 it is evident that the radial stresses are comparatively higher at a higher heat flux, due to higher temperature gradients for the same heat transfer coefficient ratio. Also, the outer surface of the inner tube experiences a higher compressive stress when the inner tube heat transfer coefficient is lower than that of the outer tube. This is because a lower heat transfer coefficient will increase the temperature gradient at that point as seen in Figs 73 and 74. A heat transfer coefficient ratio of 1 (H=1) provides the least compressive stress.

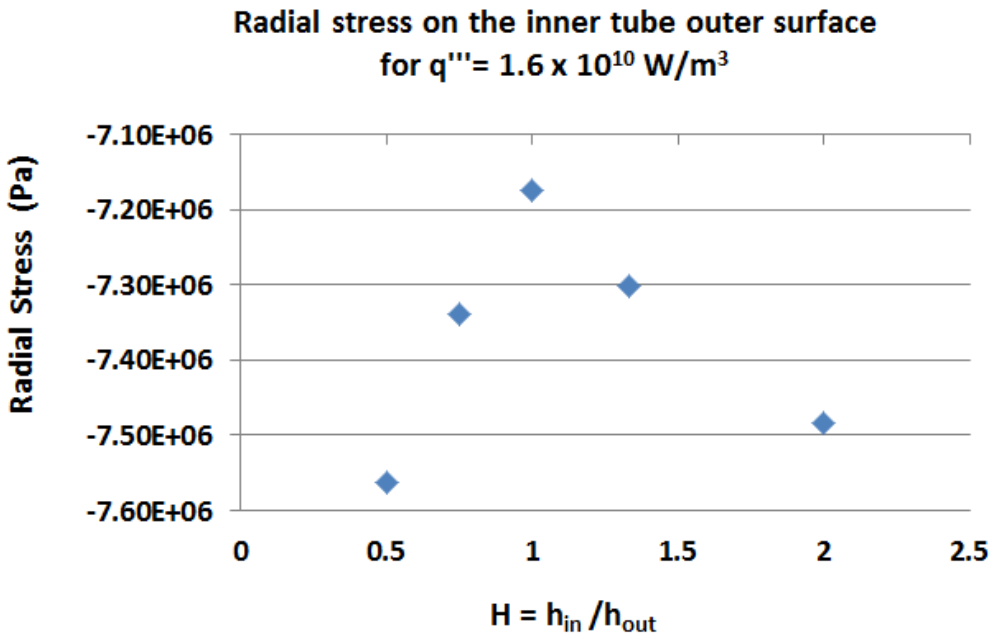

Figure 75. Radial stress on the inner tube outer surface with varying heat transfer coefficients for uniform heating.

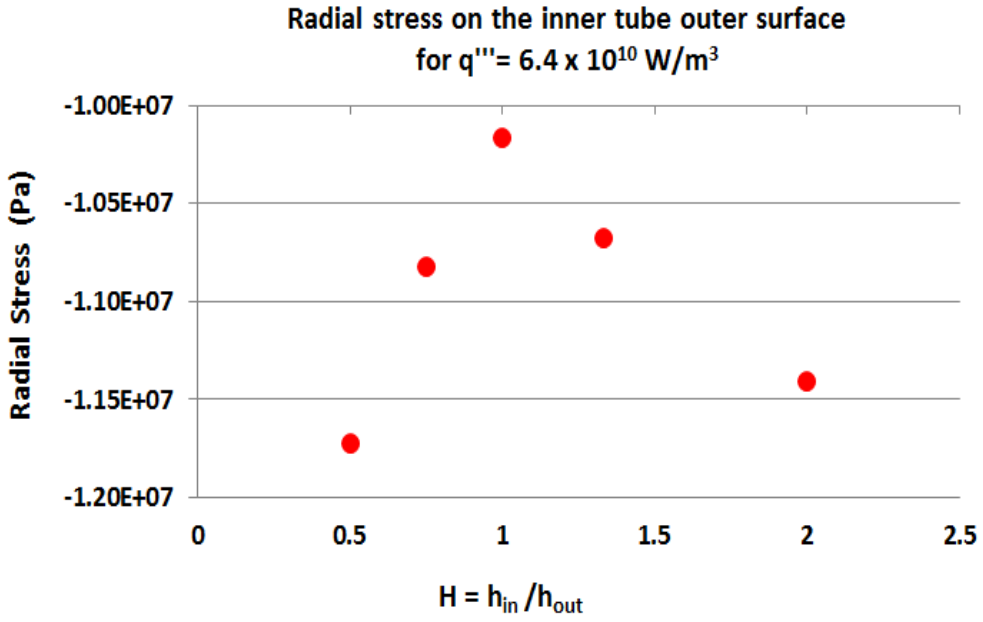

Figure 76. Radial stress on the inner tube outer surface for a higher LEU heat generation rate with varying heat transfer coefficients (uniform heating)

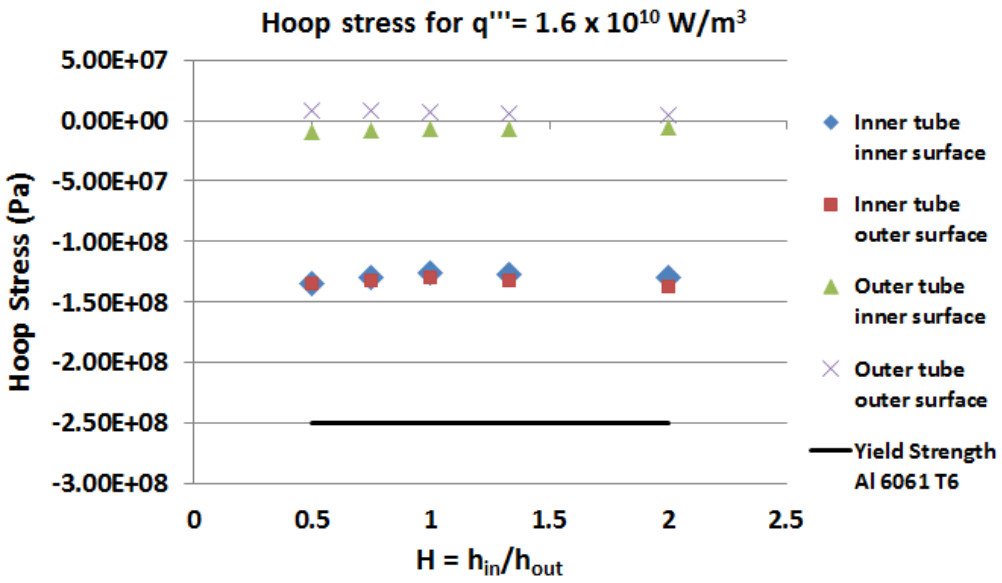

Figure 77. Hoop stress distribution in the tubes with varying heat transfer coefficient ratios for uniform heating.

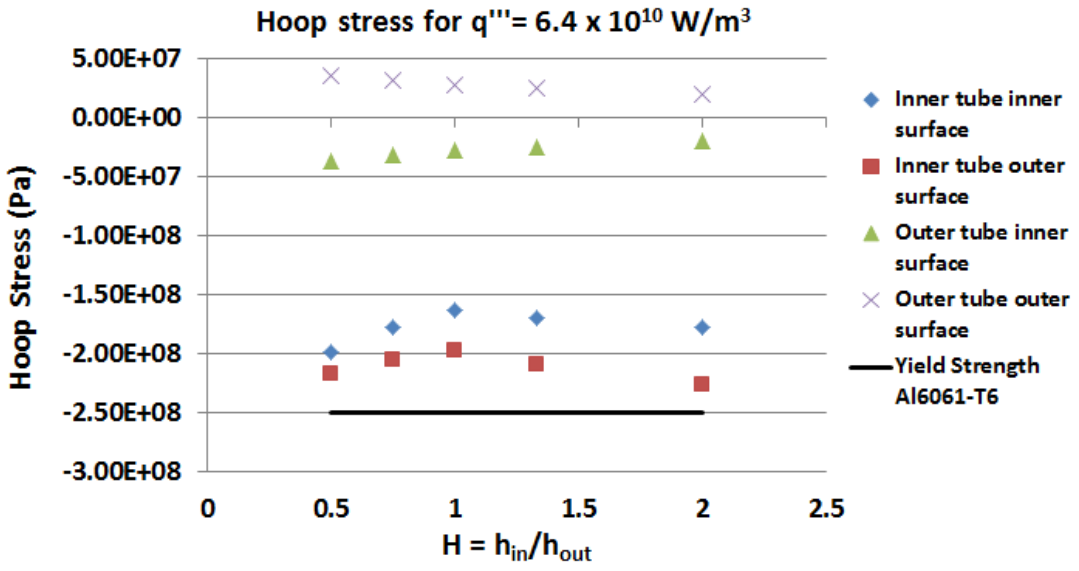

Figure 78. Hoop stress distribution in the tubes for varying heat transfer coefficients at a higher LEU heat generation rate (uniform heating)

The hoop stress distribution in the tubes for a lower and a higher heat generation of LEU are provided in Figs 77 and 78. Figures 73 and 74 illustrate that the temperature increases on either side of H=1. Since the hoop stresses are driven by the temperature gradients , the magnitude of compressive hoop stresses will correspondingly increase on either side of H=1.At a higher heat generation rate (Fig 78) the magnitude of compressive hoop stresses are larger than at a comparatively lower heat generation rate due to higher temperature gradients for the same heat transfer coefficient ratio. The inner surface of the inner tube is at a lower temperature compared to the outer surface of the inner tube, hence the magnitude of compressive stresses are lower. An interesting aspect as illustrated in Figs 64 and 65 is the separation that occurs between the foil and the outer tube due to radially outward heat flow and the difference in thermal expansion coefficients of the materials. Figures 79 and 80 show that the separation that occurs between the foil and the outer tube can be controlled by varying the heat transfer coefficient

ratio. It is observed that at higher heat generation rates, the magnitude of separation increases as the surfaces expand more due to comparatively higher temperature gradients. It is also shown that, for a given heat generation rate, greater separation occurs when the inner tube heat transfer coefficient is twice that of the outer tube. In Fig 79 for H<1 the separation is approximately a constant. Hence a cooling scheme can be designed in such a way that there is more outer cooling if there is a coolant imbalance.

Figure 81 illustrates the effect of varying the heat transfer coefficient on the contact pressure. Basically, a higher contact pressure will exist when the inner tube thermally expands a lot more due to a higher temperature gradient. This is why at H=0.5 in Fig 81, the contact pressure is the highest as the inner tube heat transfer coefficient takes its lowest value at this ratio. The numerical data was validated using Madhusudhana's model (Madhusudhana ,1998) and was found to be in good agreement.

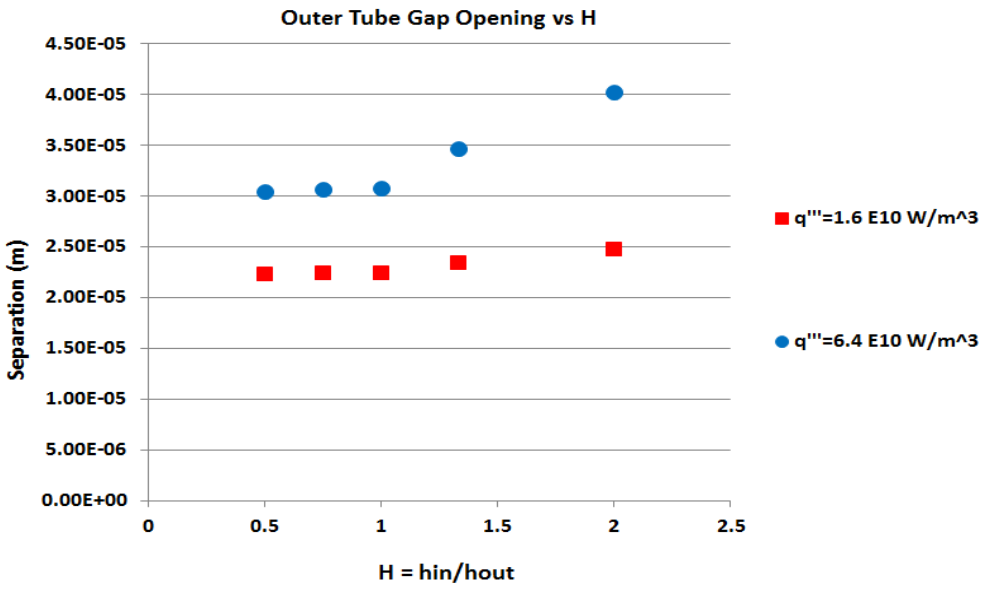

Figure 79.Effect of varying the heat transfer coefficient on the separation between the foil and the outer tube (uniform heating).

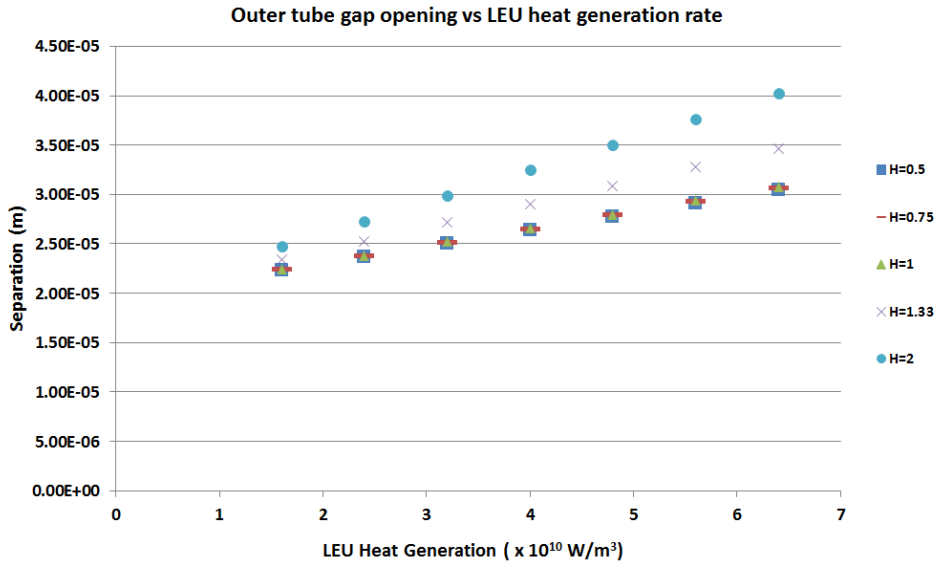

Figure 80.Effect of varying the LEU heat generation on the separation between the foil and the outer tube for the case of uniform heating.

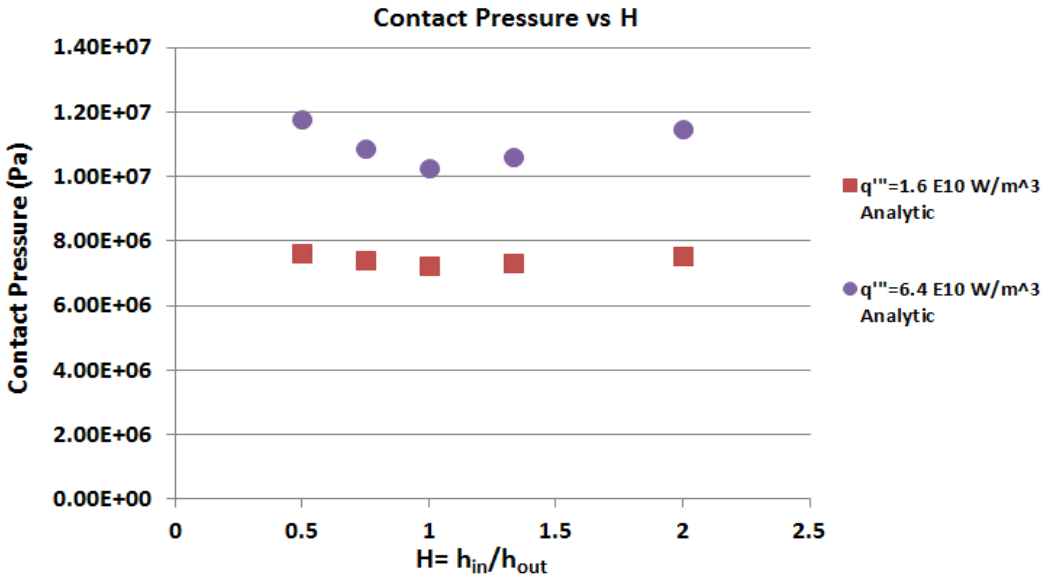

Figure 81.Effect of varying the heat transfer coefficient ratio on the contact pressure on the inner tube for the case of uniform heating.

The final parameter of interest is the ratio of thickness of the inner tube to the outer tube. The previous analysis in Fig 82 showed that the maximum compressive stress generated in the outer tube is about 30 MPa, which is well below the yield strength of Aluminum 6061-T6. Hence it was decided to look into the hoop stress values on the inner and outer surfaces of the inner tube alone as the hoop stresses on the inner tube are much greater than on the outer tube. The thickness ratio was selected based on Table 10.

Table 10. Parametric study on tube thickness ratios

t_{in} x 10^{-4} (m)	t_{out} x 10^{-4} (m)	t_{in}/t_{out}
7.85	8.30	0.96
7.85	9.55	0.82
4.85	9.55	0.51
2.85	9.55	0.30
0.85	9.55	0.09

Figure 82 illustrates the hoop stress distribution as a function of the ratio of thickness of the tubes. The values are plotted for varying heat transfer coefficient ratios. The plots show that for thickness ratios lesser than 0.3, the target is likely to fail as the hoop stresses overshoot the yield stress of the aluminum cladding. Figures 82 and 83 also show that the current target design with a thickness ratio of 0.82 falls in the safe zone.

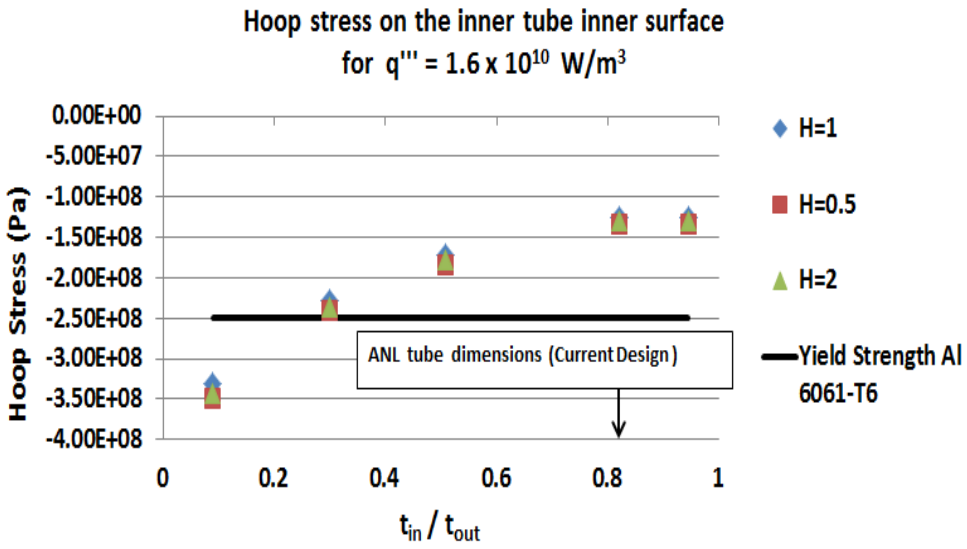

Figure 82. Hoop stress distribution with varying thickness on the inner surface of the inner tube for the case of uniform heating.

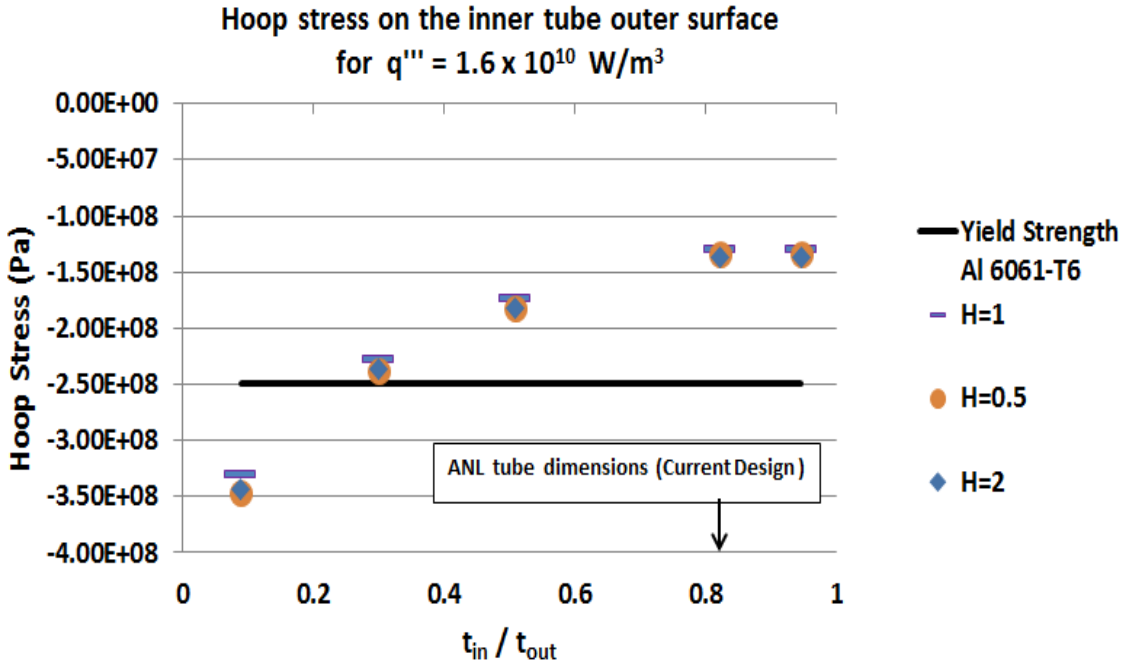

Figure 83. Hoop stress distribution with varying thickness on the outer surface of the inner tube for the case of uniform heating.

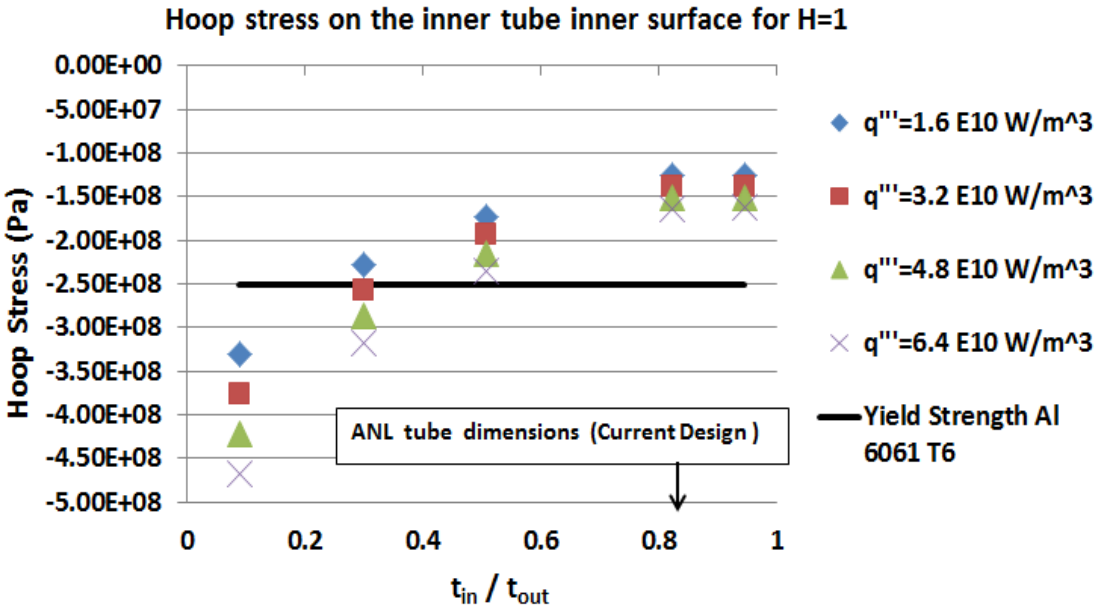

Figure 84. Variation of hoop stresses on the inner surface of the inner tube at different LEU heat generation rates for the case of uniform heating.

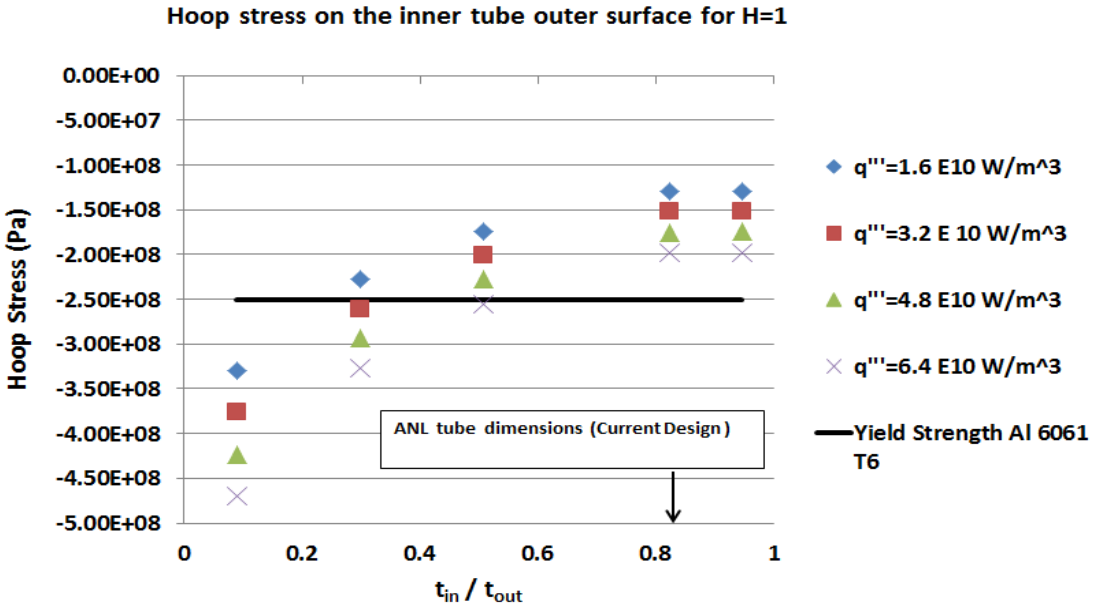

Figure 85. Variation of hoop stresses on the outer surface of the inner tube at different LEU heat generation rates for the case of uniform heating.

Figure 84 shows the variation of hoop stresses on the inner surface of the inner tube over a range of LEU heat generation rates. A thickness ratio of 0.5 seems to be the safe zone for all the heating conditions in Fig 84, though the highest heat generation rate seems to result in hoop stresses close to the yield strength of the aluminum cladding. A thickness ratio of 0.3 seems to be satisfactory ratio for a heat generation of1.6 x10^{10} W/m^3 but the target will fail at higher heat fluxes as the hoop stresses on the inner surface of the inner tube exceed the yield stress of the aluminum cladding**.**

From Fig 85, it is observed that the safe operating zone for the outer surface of the inner tube shifts from a thickness ratio of 0.5 to the current design ratio. The tube thickness ratio of 0.5 will result in failure of the target as the hoop stresses on the outer surface of the inner tube exceeds the yield stress of the aluminum cladding. From Figs 84 and 85, a thickness ratio of 0.82 will help the inner and outer surfaces of the inner tube withstand LEU heat generation as high as 6.4 x 10^{10} W/m^3. This analysis also proves that the current target design, which is based on the dimensions of the ANL annular target design (Solbrekken,2008) is safe.

Chapter 8: Proposed Experimental Test Plan

Though the previous chapter (section 6.3) showed that the uniform heating numerical model can be used to validate the non-uniform heating model by comparing the relative order of magnitudes, the use of experimental data can be used to accurately validate the non-uniform heating model and also help in the thermal contact resistance prediction which is incomplete at the moment.

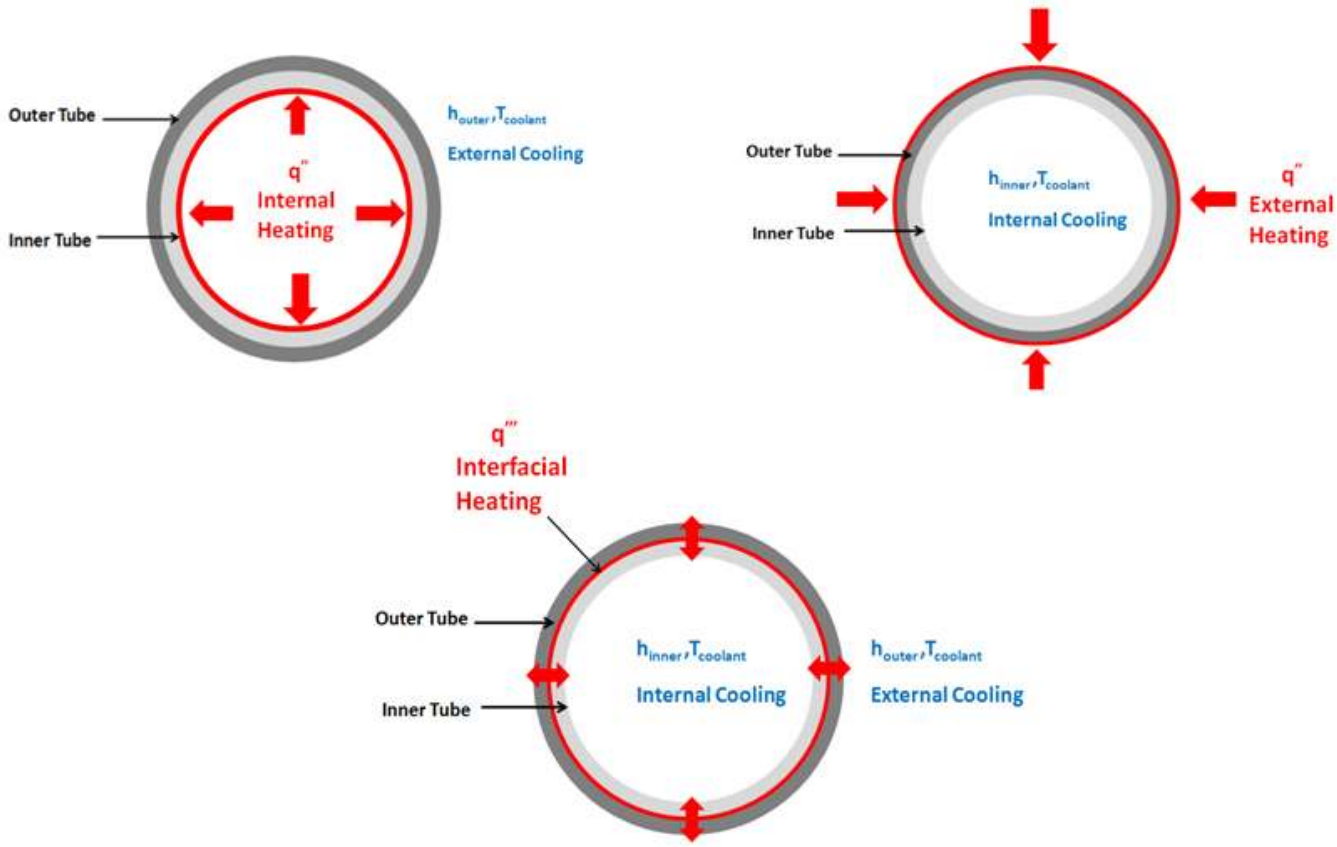

Figure 86. Graphic showing the internal, external and interfacial heating configurations.

The interfacial heating as illustrated in Fig 86 results in radially inward heat flow into the inner tube and radially outward heat flow into the outer tube. This can be thought of as the inner tube being externally heated and the outer tube being internally heated. Turner et.al (Turner, 2009) showed that the state of the interface can be controlled based on the direction of heat flow into the tubes. For internal heating compressive stresses are induced in the tubes and for external heating tensile stresses are induced in the tubes. These findings need to be validated experimentally and to verify these with interfacial heating. For the interfacial heating case, it is proposed that a heater will be placed between the aluminum tubes to simulate the LEU heat source. Once the heater is placed between the tubes, it is required to place the thermocouples at suitable locations to obtain the surface temperatures.

The use of strain gages will be required to determine the thermal strain and use it to indirectly determine the thermal stresses induced in the tubes due to the flow of heat and thermal expansion. At this point, the exact locations of the thermocouples and strain gages on the tube surfaces have not been identified. However, the current numerical model for non-uniform heating can be used to visualize the areas of maximum and minimum stresses, temperatures and deflections. The decision on the locations of the thermocouples and strain gages can be made based on these observations.

Figure 87 shows the test chamber for the external heating of the tubes. The chamber is made of 0.5 inch acrylic material while the inner railings are of Aluminum 6061 material. A ‘U’ bolt, attached to the railing, will be used to hold the annular target. A rope heater, Fig 88, will be used to simulate external heating. The use of a rope heater is advantageous as it can easily adhere onto a surface with thermal grease and also easily conforms to a curved surface. The rope heater will be wrapped around the aluminum tube as shown in Fig 88.

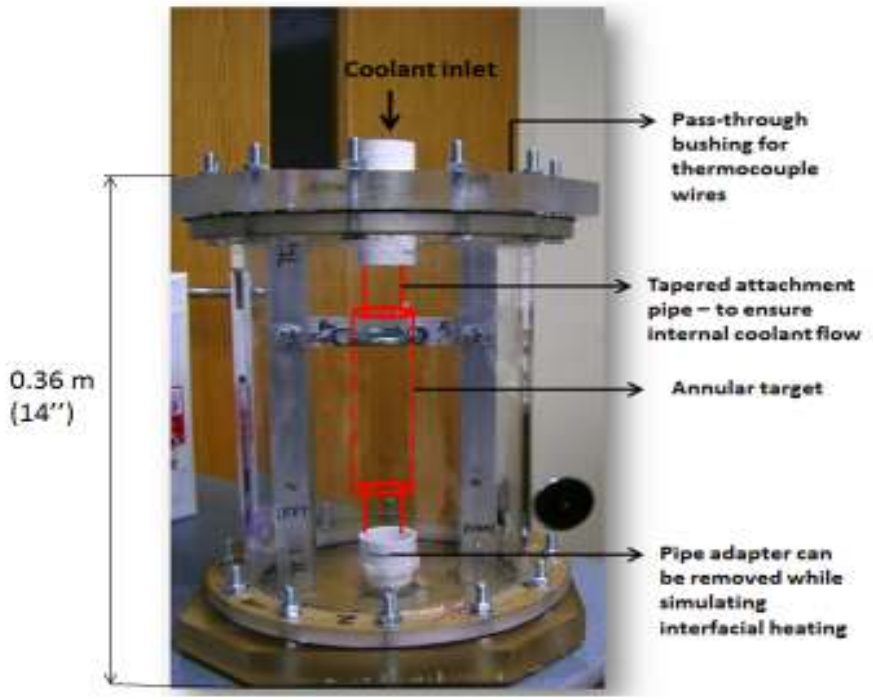

Figure 87. Test chamber to simulate external heating of the annular target.

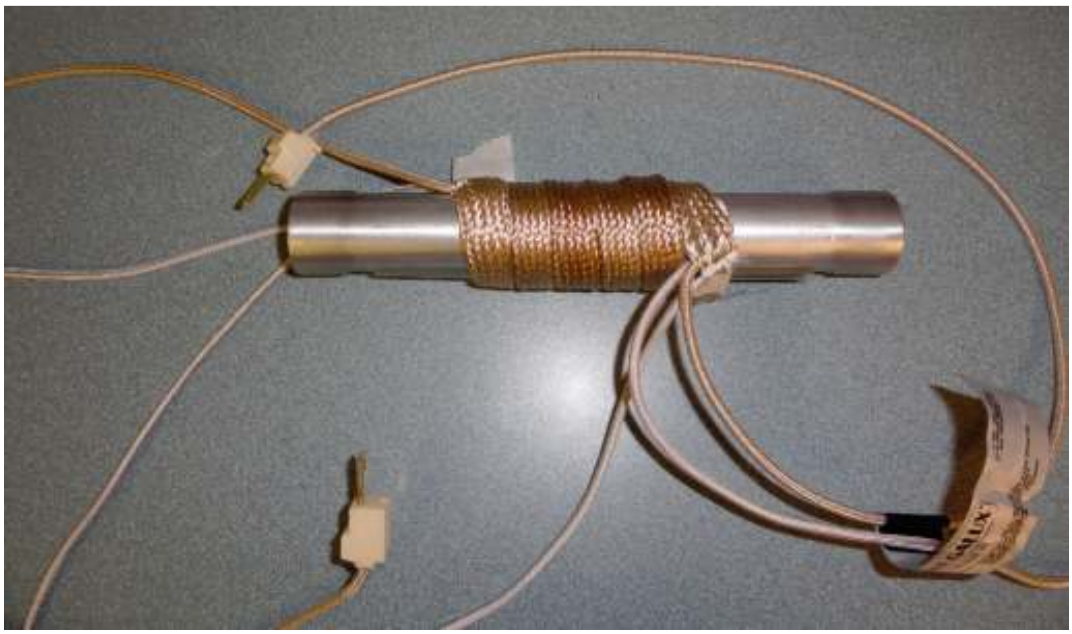

Figure 88. A rope heater wrapped around a sample annular target.

One of the difficulties was to find a suitable heater to cover the entire length of the tube for both the external and internal heating configurations. Hence it was decided to heat only a portion of the tube, resulting in non-uniform heating. This could be advantageous as these experiments can be directly used to validate the non-uniform heating numerical data from Abaqus FEA. The test chamber to be used for internal heating is shown in Fig 89 and a kapton heater will be placed on the inner surface of the inner tube. The difficulty involved in mounting the heater on the inner surface of the tube and the inability to find a heater to cover the entire length of the tube, prompted the choice of a flexible kapton heater that will heat only a portion of the tube. This heater is shown in Fig. 90.

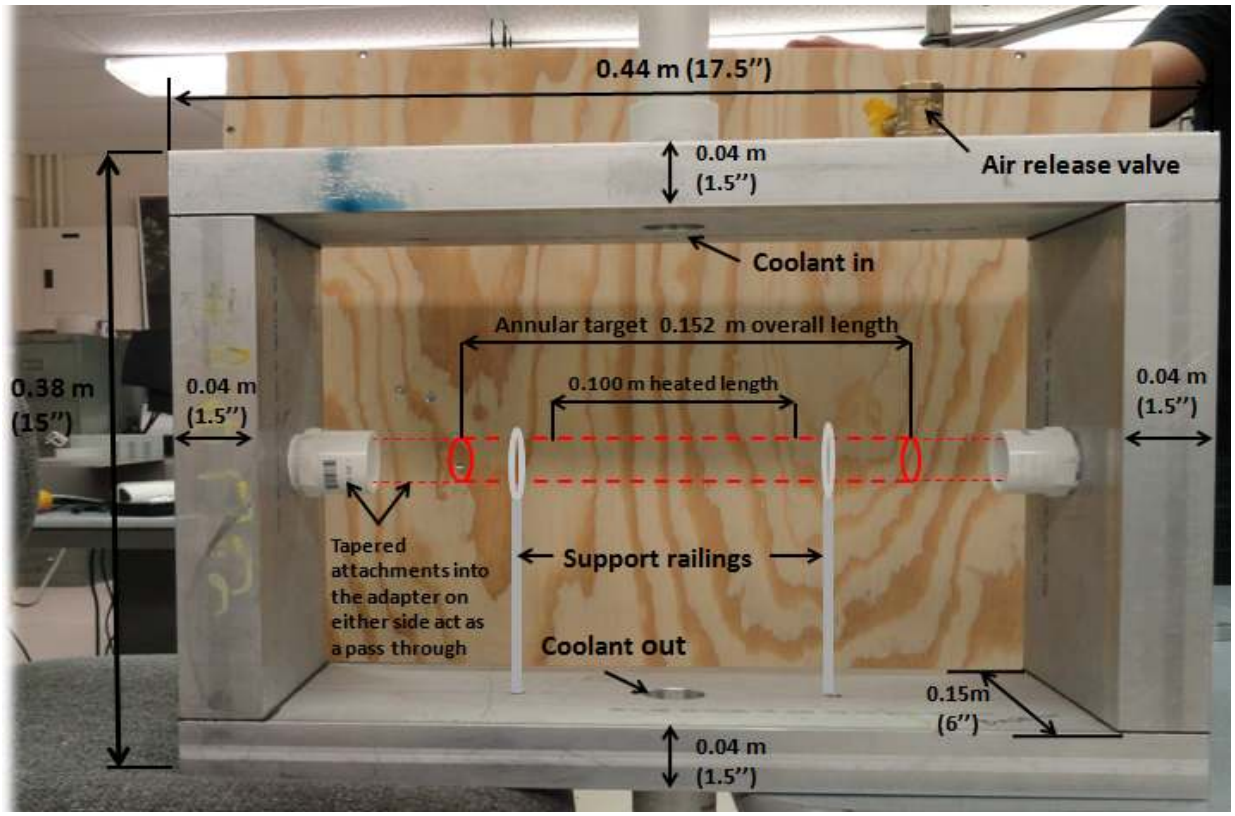

Figure 89. Test chamber to simulate internal and interfacial heating.

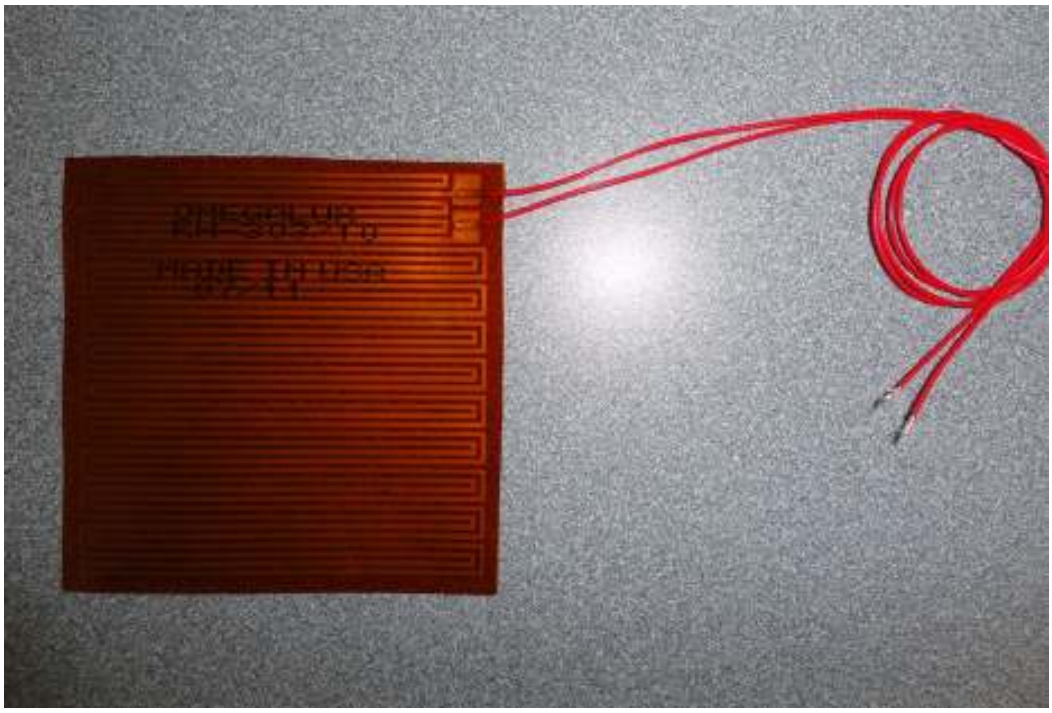

Figure 90.Flexible kapton heater to simulate internal heating.

The test chambers shown in Fig 87and Fig 89 can be used to simulate interfacial heating as well if the tapered pipe attachments are removed. At this point, the search is on for a suitable heater to simulate the interfacial heating condition. Though experiments have not been performed as yet, the tools required to simulate the same have been built and identified.

Chapter 8: Conclusions and Recommendations

The goal of this research was to develop modeling tools to analyze the thermal-mechanical behavior of the LEU foil based annular target and identify the potential conditions under which target would fail. The current analysis did not consider the pre-stresses induced in the tubes during the assembly procedure. The commercial finite element code Abaqus FEA was used to perform the numerical analysis on the annular target with a recess. A uniform heating numerical model was developed and it was validated using analytical expressions. This uniform heating model was used to validate the non-uniform heating Abaqus model. Also, an analytic model to predict the thermal stresses in a composite structure subject to radially inward heat flow was developed.

The current analysis provided an insight into the behavior of the target under various operating conditions and it was found that the current design which is based on the annular target design of Argonne National Lab, is reliable even at high heat fluxes and the magnitude of separation between the foil and the outer tube can be controlled by adjusting the heat transfer split between the inner and outer surfaces. The results from this analysis demonstrate that the LEU foil based annular target can be safely irradiated without compromising on reactor safety. It also provides a basis for the operating safety limits of the annular target which can be used a useful reference tool for future analysis.

Experimental data is required to accurately validate the non-uniform heating results and to predict the thermal contact resistance at the interface of the LEU foil and the aluminum tube cladding. The prediction of thermal contact resistance will require macroscopic and/or

microscopic surface characterization. Hence a study into the surface characteristics of the foil is also recommended.

Since a gap opens up between the LEU foil and the outer tube, it is worth looking into the internal pressure required to close this gap and the resulting contact pressure. Future work includes the extension of the current analysis to a 3-D modeling environment. Also, if an analytic model can be developed for the non-uniform heating condition, then the uniform heating case can be completely ignored and the non-uniform heating analytic model can be directly used to validate the numerical data from Abaqus FEA.

APPENDIX

Appendix 1 : Mathematica Code

A. Mathematica Notebook To Determine the Heat Flux Entering the Tubes

```
Clear[r1,r2,r3,r4,Tinf,Kal,h1,h4,L,Rconvout,Rcondout,Rcondin,Rconvin,Reffout,Reffin,REFF,q
uranium,qinward,qoutward,qfluxinward,qfluxoutward]

(*Rcondout,Rconvout,Reffout : conduction resistance through the outer aluminum tube ,
convective resistance on the outer tube outer surface and effective series resistance in the
radially outward direction *)

(*Rcondin,Rconvin,Reffin : conduction resistance through the inner aluminum tube , convective
resistance on the inner tube inner surface and effective series resistance in the radially inward
direction *)

(* Dimensions and other definitions *)

r1=0.01321;    (*meters*)  (*Inner tube inner radius *)
r2= 0.013995;(*meters*) (* Inner tube outer radius = Foil Inner radius *)
r3= 0.01412; (*meters*)(* Foil outer radius =Outer tube Inner radius *)
r4=0.015075;(*meters*) (* Outer tube outer radius *)
foilthickness=125*10^-6;(*meters*)
rcenter=(r2+((r3-r2)/2)); (*meters*) (* Uranium foil center line radius *)

Tinf=323;(*Kelvin*)(* Coolant temperature *)
Kal=167; (*W/mK*)(* Thermal conductivity of Aluminum *)
Ku =27.5; (*W/mK*)(* Thermal conductivity of Uranium *)
h1 = 19000; (*W/m^2K*)(*Inner tube heat transfer coefficient *)
h4 = 19000;(*W/m^2K*)(*Outer tube heat transfer coefficient *)
L=0.100; (*meters*) (* length of the heated section which will be the length of the foil *)


(* Determination of uranium temperature *)

Rcondout= Log[r4/r3] / (2*Pi*Kal*L);(*Kelvin/Watt*) (* Conduction resistance in the outer
tube *)

Rconvout = 1/ (h4*2*Pi*r4*L);(*Kelvin/Watt*)(* Convective resistance outer coolant *)

Reffout=Rcondout+Rconvout;(*Kelvin/Watt*) (* Effective resistance of the outer tube *)
```

Rcondin= Log[r2/r1] / (2*Pi*Kal*L);*(*Kelvin/Watt*)(* Conduction resistance in the inner tube *)*

Rconvin = 1/ (h1*2*Pi*r1*L);*(*Kelvin/Watt*) (* Convective resistance inner coolant *)*

Ruraniumin=Log[rcenter/r2]/(2*Pi*Ku*L);

Reffin =Rcondin+Rconvin(*+ Ruraniumin *);*(*Kelvin/Watt*)*

REFF = (Reffout*Reffin)/(Reffout+Reffin);*(*Kelvin/Watt*) (* resistance in parallel *)*

(*deltaT=Turanium-Tinf; (*Kelvin*) *)

quranium=17665.17 ; (*Watts*) *(* obtain quranium from qgen =1.6*10^10 as follows : quranium=qgen*2*Pi*rcenter*L*foilthickness *)*

Turanium = Tinf + (REFF * quranium); *(* Temperature of uranium *)*

(Now that the uranium temperature has been determined it can be used to calculate the heat fluxes in the radially inward and outward directions *)*

(* quranium = qoutward + qinward *)

qoutward = (Turanium-Tinf)/(Reffout) ;*(*Watts*)*

qfluxoutward=qoutward/(2*Pi*r3*L*) ; (*W/m^2*)(* Radially outward heat flux *)*

qinward=(Turanium-Tinf)/(Reffin) ; (*Watts*)

qfluxinward=qinward/(2*Pi*r2*L)(*W/m^2*) ; *(* Radially inward heat flux *)*

*(*The heat fluxes obtained here are used to determine the analytical radial stress, hoop stress , displacements and temperature*)*

B. Mathematica Notebook to Calculate the Stresses , Displacement and Temperature on the Outer Tube

(* This notebook calculates the stresses , displacement and temperature across the radius of the outer tube *)
(* Plane Strain Formulation Used *)

```
 Clear[r,Tinf,qflux,hb,a,b,Tdist,alpha1,alpha,EAl1,EAl,vAl,k]
Clear[sigmaRplanestrain,R,sigmaTHETAplanestrain,uRplanestrain]

Tinf=323;(* Coolant temperature *)
qflux=1.04972*10^6; (* Obtained based on mathematica notebook in appendix A *)
h=19000;(* outer heat transfer coefficient *)
a=0.01412;(* Outer tube inner radius *)
b=0.015075;(* Outer tube outer radius *)
Tdist= Tinf + ( ((qflux*a)/k)* (Log[b/r] + (k/(b*h))));
Tdistribution=Tinf + ( ((qflux*a)/k)* (Log[b/R] + (k/(b*h))));

alphaAl =2.34*10^-5;(* Used for Plane Stress *)
EAl=69*10^9; (* Used for Plane Stress *)
alphaAl1 = 2.34*10^-5;(* Thermal expansion coefficient .Used for Plane Strain *)
 EAl1=69*10^9; (* Young's modulus.Used for Plane Strain *)
```

(* For the plane strain case alpha*EAl is replaced by (alpha1*EAl1/(1-vAl)) . See Theory of thermal stresses ,circular disc or cylinder, by BOLEY page 290-291 *)

```
vAl=0.33;(* Poisson's ratio of Aluminum *)
k=167; (* Thermal conductivity of Aluminum *)

R=0.01412; (* Change this value to determine the stresses , displacement and temperature at
each nodal location across the radius *)

Tinteg1=Integrate[Tdist*r ,{r,a,b}];
Tinteg2 =Integrate[Tdist*r,{r,a,R}];

Tdistribution=Tinf + ( ((qflux*a)/k)* (Log[b/R] + (k/(b*h))));

sigmaRplanestrain= ((alphaAl1*EAl1)/((1-vAl)*R^2)) * ( ( ((R^2 -a^2)/(b^2-a^2)) * Tinteg1 ) -
Tinteg2);

sigmaTHETAplanestrain = ((alphaAl1*EAl1)/((1-vAl)*R^2)) * (( ( ((R^2 +a^2)/(b^2-a^2)) *
Tinteg1 ) + Tinteg2)-(Tdistribution*R^2));

 uRplanestrain=(alphaAl/(R*(1-vAl))) * (  ((1+vAl) * Tinteg2) +  (((((1- 3*vAl)*R^2) + (
(1+vAl)*a^2))/(b^2-a^2))*Tinteg1));
```

C.Mathematica Notebook to Calculate the Stresses , Displacement and Temperature on the Inner Tube.

```
Clear[m,rhs1,rhs2,rhs3,rhs4,c1,c2,c3,c4,m1,m2,sigmaR,sigmaT,uR,R,deltaTa,Taluminum,Turani
um,Tdist,Tdist1,deltaTa,EAl,Efoil,alphaAl,alphafoil,vAl,vfoil,a,b,c,m1,m2,Tu,Tu1,Tinfinner,qfl
ux,kAl,kfoil]

(*    Boundary Conditions Used in the Model *)
(*   BC 1 - SigmaR at a=0 *)
 (*  BC 2 - SigmaR at c=0 *)
 (*  compatibility boundary condition 1 - SigmaR Al at r=b  =   SigmaR U at r=b *)
(*  compatibility boundary condition 2 - U Al at r=b  =  U U at r=b *)
(*  Inner tube - Aluminum and Outer Tube- Uranium *)

a=0.01321;(* Inner tube inner radius in 'm'*)
b=0.013995;(* Inner tube outer radius = Foil inner radius in 'm' *)
c=0.0140575;(* Foil outer radius in 'm'*)

EAl=69*10^9;(* Young's modulus of aluminum in 'Pa' *)
Efoil=208*10^9;(* Young's modulus of uranium in 'Pa' *)
vAl=0.33;(* Poisson's ratio of aluminum *)
vfoil=0.23; (* Poisson's ratio of uranium *)
alphaAl=2.34*10^(-5);(* Thermal expansion coefficient of aluminum in 'K^-1' *)
alphafoil=1.39*10^(-5);(* Thermal expansion coefficient of uranium in 'K^-1' *)

kAl=167;(* Thermal conductivity of aluminum in W/mK*)
kfoil=27.5;(* Thermal conductivity of uranium in W/mK *)
qflux=949836;(*  Heat flux entering the inner tube in W/m^2K. Obtained based on mathematica
notebook in appendix A *)
Tinfinner=323;(* Coolant temperature in Kelvin *)
ha=19000;(*Inner tube heat transfer coefficient  W/m^2K *)

Tdist1=Tinfinner +  ( (qflux*c)* ( ( Log[r/a]/kAl ) + (1/(a*ha))));

Tb=Tinfinner +  ( (qflux*c)* ( ( Log[b/a]/kAl ) + (1/(a*ha))));

Tur = Tinfinner+((qflux*c)*(  (Log[r/b]/kfoil) + (Log[b/a]/kAl)+(1/(a*ha))));

(* Right side of the matrix *)

m = { { (EAl/((1+vAl)*(1-(2*vAl)))) , (-EAl/((1+vAl)*a^2)) , 0,0} , { 0,0, (1/(1-(2*vfoil))) , (-
1/(c^2)) } , { (EAl/((1+vAl)*(1-(2*vAl)))) , (-EAl/((1+vAl)*b^2)), (-Efoil/((1+vfoil)*(1-
(2*vfoil)))), (Efoil/((1+vfoil)*b^2))} , { b , (1/b) , -b , (-1/b) }};

rhs1=0;(* RHS from BC 1 - SigmaR at a=0 *)
```

```
rhs2= ((alphafoil*(1+vfoil)) /((1-vfoil)* (c^2)))*Integrate[Tur*r,{r,a,c}];(* RHS from BC 2 - SigmaR at c=0 *)

rhs3= ((-alphafoil*Efoil / ((1-vfoil)*(b^2)))*Integrate[Tdist1*r,{r,a,b}])+((alphaAl*EAl / ((1-vAl)*(b^2)))*Integrate[Tb*r,{r,a,b}]); (* RHS from compatibility condition 1 - SigmaR Al at r=b = SigmaR U at r=b *)

rhs4= (((1+vfoil)*alphafoil / ((1-vfoil)*(b)))*Integrate[Tdist1*r,{r,a,b}])+((-(1+vAl)*alphaAl / ((1-vAl)*(b)))*Integrate[Tb*r,{r,a,b}]);(* RHS from compatibility condition 2 - U Al at r=b=U U at r=b *)

(* Solving the matrix to determine the four constants *)

 Solve[m.{c1,c2,c3,c4}□{rhs1,rhs2,rhs3,rhs4},{c1,c2,c3,c4}]

m1=c1; (* replace c1 with m1 just for convenience*)
m2=c2;  (* replace c2 with m2 just for convenience*)

 Clear[sigmaR,sigmaT,Tdist,R]

R=0.0132885;(* Change R to determine the stresses and temperature at any nodal location across the radius of the tube *)

 Tdist=Tinfinner +  ( (qflux*c)* ( ( Log[R/a]/kAl ) + (1/(a*ha))))

sigmaR = -(((alphaAl*EAl)/((1-vAl)*R^2))*Integrate[Tdist1*r ,{r,a,R}] )+ ( (EAl/(1+vAl))*( (m1/(1-(2*vAl)))-(m2/R^2)))

sigmaT = (((alphaAl*EAl)/((1-vAl)*R^2))*Integrate[ Tdist1*r,{r,a,R}])-((alphaAl*EAl*Tdist)/(1-vAl))+ ( (EAl/(1+vAl))*( (m1/(1-(2*vAl)))+(m2/R^2)))

 uRplanestrain = (( ((1+vAl)*alphaAl)/((1-vAl)*R))*Integrate[Tdist1*r,{r,a,R}]) + (m11*R)+(m22/R)
```

D. Mathematica Notebook to Calculate the Contact Pressure on the Inner Tube Using Madhusudhana's Model (Madhusudhana , 1999)

```
(* This mathematica notebook is to compare the pressure obtained using Abaqus to that
obtained using Madhusudhana's formulation *)
(* The  obtained pressure will be in MPa *)

Clear[delTi,p,Ta]

a=13.21*10^(-3); (* Inner tube inner radius in 'm'*)
b=13.995*10^(-3);  (* Inner tube outer radius = Foil inner radius in 'm' *)
c=14.12*10^(-3); (* Foil outer radius in 'm'*)

kAl=167; (* Thermal conductivity of aluminum in 'W/mK ' *)
alphaAl1=2.34*10^(-5);(* Thermal expansion coefficient of aluminum in ' W/mK ' *)
EAl1=70*10^9;(* Young's modulus of aluminum in 'Pa' *)
vAl1=0.33; (* Poisson's ratio of aluminum *)
kU=27.5; (* Thermal conductivity of uranium in 'W/mK ' *)
alphaU1=1.39*10^(-5);(* Thermal expansion coefficient of uranium in ' W/mK ' *)
EU1=208*10^9;(* Young's modulus of uranium in 'Pa' *)
vU1=0.23;(* Poisson's ratio of uranium *)

(* Writing E,v and alpha in terms of plane strain *)

Ei1=EAl1/(1-(vAl1^2));vi1=vAl1/(1-vAl1);alphai1=alphaAl1*(1+vAl1);ki=kAl;
E01=EU1/(1-(vU1^2));v01=vU1/(1-vU1);alpha01=alphaU1*(1+vU1);k0=kU;

uC=0.0;  (* Initial interference in 'm' *)

h=10^9; (* Total contact conductance in 'W/m^2K '. A high value implies infinite conductance
and perfect contact *)

(*Ta- Temp at the inner surface of the inner tube *)
(*T1-Temp at the outer surface of the inner tube *)

delTi=Ta-T1; (* Temp rise in the inner tube *)

DELTAT = (ki*delTi )/((b*Log[b/a])*h); (* ie DELTAT= q/h where q=Q/A *)
c1=Ei1/E01;
c2=(c^2+b^2)/(c^2-b^2);
c3=(b^2+a^2)/(b^2-a^2);

(*delT0=(ki/k0)*delTi*(Log[c/b]/Log[b/a]);*)
```

```
uAi = (b*alphai1*delTi)* (1-(  (2*a^2)/(b^2-a^2))*Log[b/a])/(2*Log[b/a]);
uA0 =  (b*alphai1*delTi)*  ((alpha01*ki)/(alphai1*k0))*( Log[c/b]/Log[b/a])* ( 1-(
(2*c^2)/(c^2-b^2))*Log[c/b]) / (2*Log[c/b]);

uA=uAi-uA0; (* Interference due to heat flux in 'm' *)


uB = b*(T1*(alphai1-alpha01) + (alphai1*DELTAT)); (* Interference due to contact resistance
in 'm'*)

u=uA+uB+uC;(* Total interference in 'm' *)

(* Solving to obtain the contact pressure in MPa *)

Solve[u == ((b*p)/(Ei1))*(c1*(c2+v01)+(c3-vi1)),p]
```

Appendix 2 : Fully Coupled Thermal Stress Analysis Procedure in Abaqus FEA

Before a model can be created and analyzed in Abaqus FEA , a sequence of steps have to be carried out to setup the model and mesh it. The procedure to setup a fully coupled thermal stress analysis of the LEU foil based annular target with a recess will be explained here.

1. The first step after opening Abaqus , is to create the parts involved in the simulation. Click on ‘Parts’ , name the part as ‘inner tube’, select 2-D planar , deformable shell and click on ‘Ok’ (Fig 2.a). Now the screen where the geometry has to be sketched opens up. Sketch the geometry of the inner tube with the appropriate dimensions and click on ‘Done’ at the bottom of the sketcher window. Repeat this procedure to create the foil and the outer tube. Totally 3 parts should have been created. It is usually a practice to partition the parts to facilitate easy meshing using a structured mesh. However this is optional and upto the user.

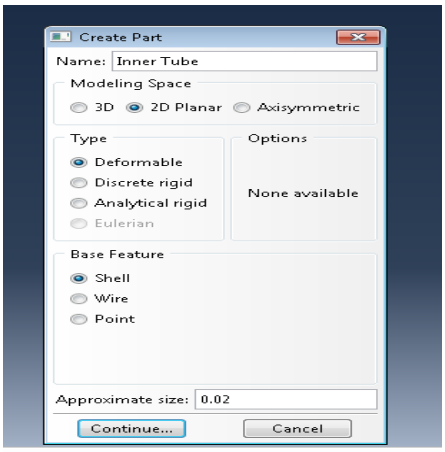

Figure 2.a Creating a part dialog box

2. Next , in the model window , click on ‘Materials’ and enter the material properties and click on ‘OK’ (Fig 2.b). If the analysis involves more than one material repeat the procedure.

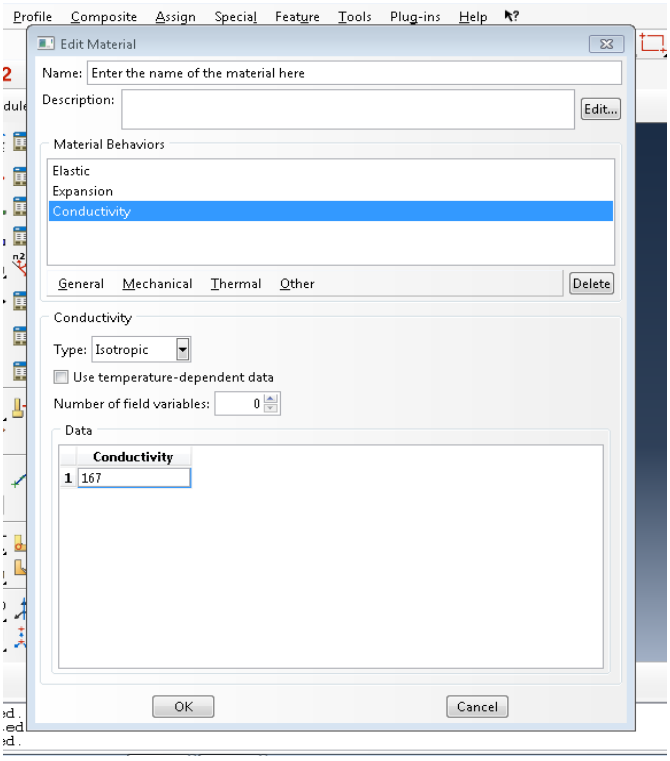

Figure 2.b Material creation dialog box

3. The next step is to create a section for each part. The number of sections in a model depends on the number of parts and materials that make up the parts. Click on ‘sections’ in the model window and enter the name of section as illustrated in Fig 2.c. Create a section each for the inner tube , foil and the outer tube and with the appropriate material.

4. Once the sections have been created , click on the small ‘+’ sign next to the part and select sectional assignment as in Fig 2.d. Now assign the appropriate section create in step 3 to this part.

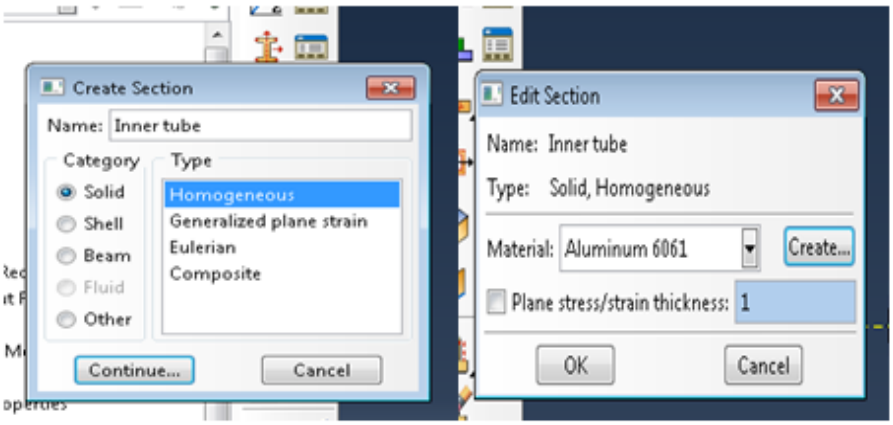

Figure 2.c Section creation dialog box

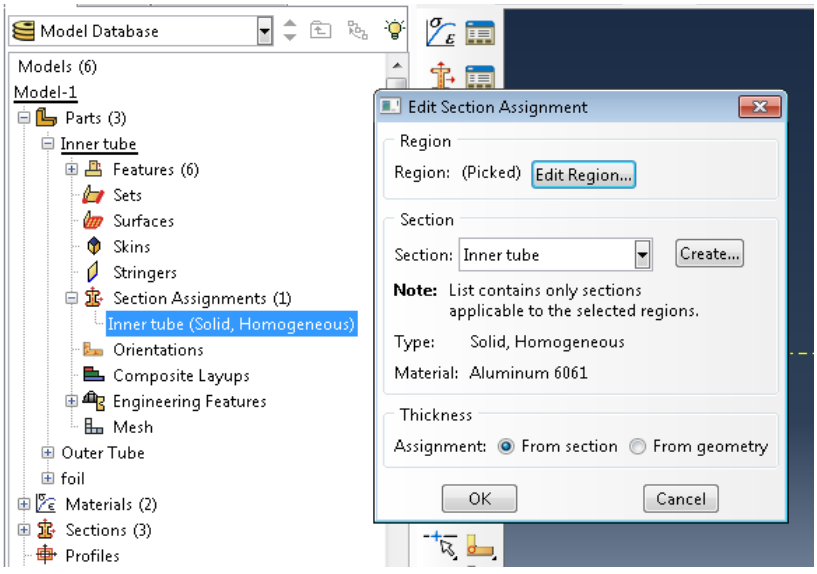

Figure 2.d Creating sectional assignments

5. Now the parts have to be assembled together. Click on ‘Assembly’ in the model window and create an ‘Instance’ of each available part as in Fig 2.e. While selecting the second and third instances , make sure that the ‘Auto-offset from other instances’ option is turned on. This will ensure that the part are offset from each other and gives the user greater control over the assembly procedure. From the main menu select ‘Instance -Translate’ and manually translate the parts by selecting their start and end point. The assembled target should look like Fig 2.f.

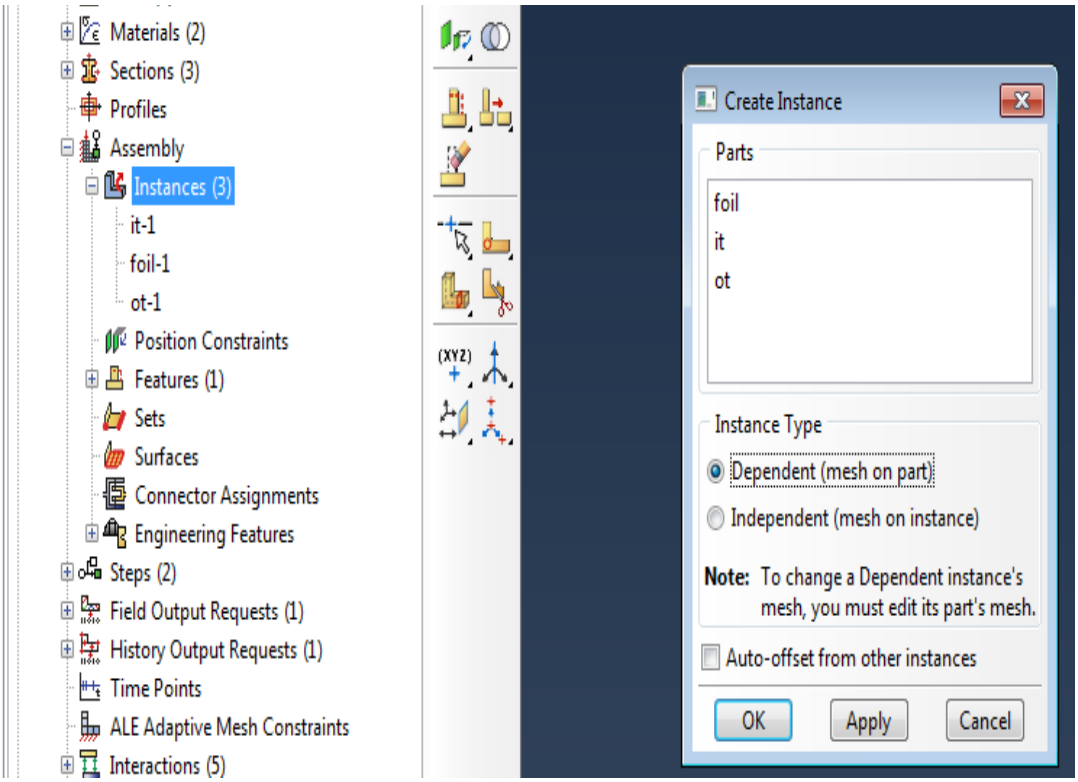

Figure 2.e. Creating an instance

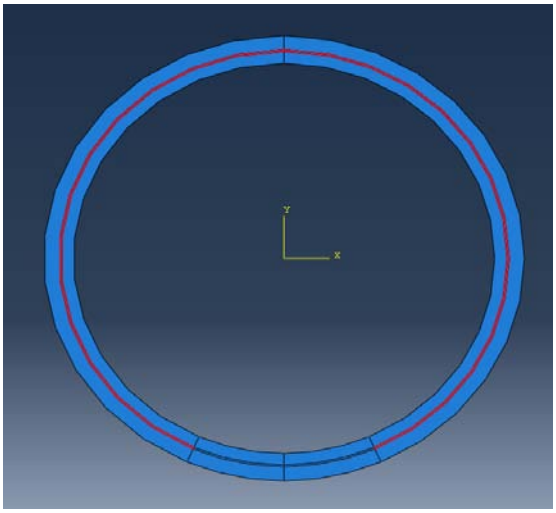

Figure 2.f The model after assembly

6. Next , create an analysis step by clicking on ‘Steps’ from the model window. Let the procedure type be ‘general’ and select ‘Coupled temp-displacement’ and click on ‘Continue’. In the ‘Edit Step’ dialog box , change the ‘Response’ type to ‘Steady-state’ and turn ON ‘NLGEOM’. This option will include any non-linearity in the analysis. Turning this option ON only increases the computational time and does not affect the analysis if any non-linearity isn’t present.
7. Next create a field output request by clicking on ‘Field Output Requests’ from the model window. This is where we select the output parameters of interest. Based on the type on Analysis step created , Abaqus automatically selects the available parameters. This is shown in Fig 2.g.

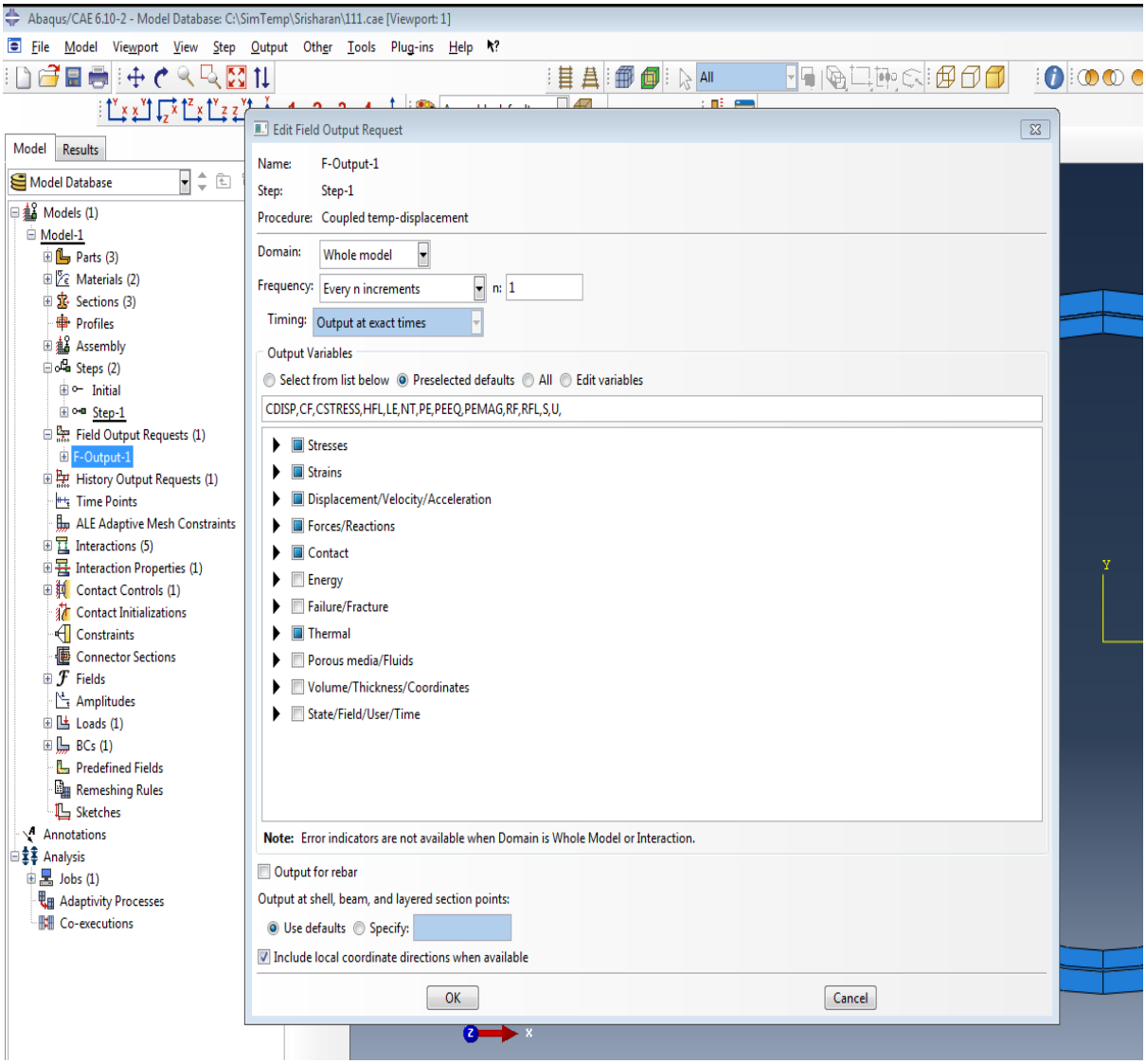

Figure 2.g. Specifying field output requests.

8. Specify the interaction properties. Double click on ‘Interaction Properties’ from the model window. Click on ‘Mechanical’ and select ‘Tangential Behavior’ and select ‘Frictionless’ under ‘Friction Formulation’ as shown in Fig 2.h.

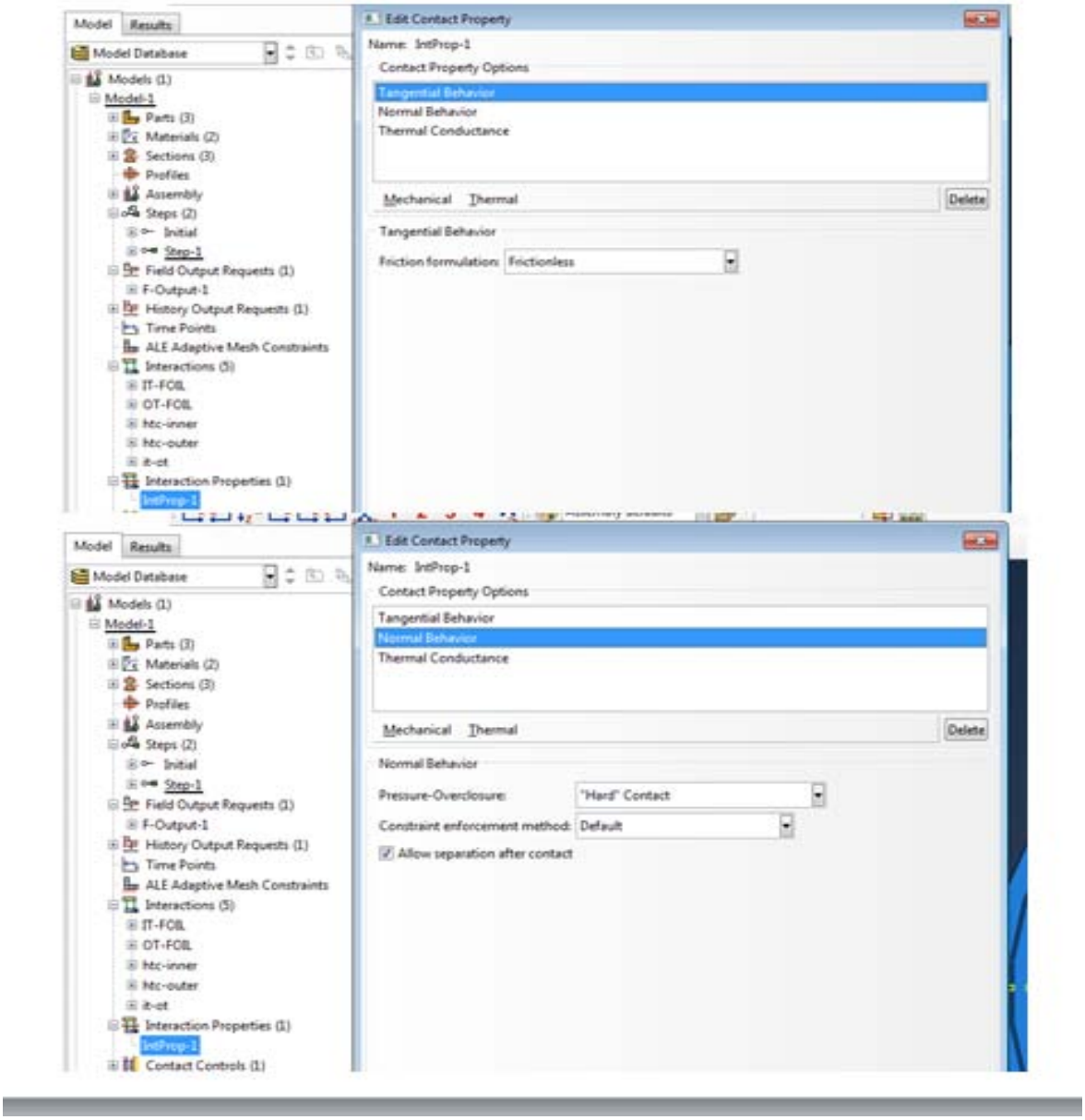

Figure 2.h. Specifying mechanical interaction properties

9. Next click on ‘Normal Behavior’ under the ‘Mechanical’ tab. Use the ‘Hard contact’ Pressure-overclosure relation and use the default constraint enforcement method. Click on ‘Allow separation after contact’ (Fig 2.h.) , since the contact maybe reinforced and relaxed in this analysis.

10. Click on the ‘Thermal’ tab and select ‘Thermal Conductance’ as shown in Fig 2.i. Specify the conductance at zero clearance and the clearance at zero conductance. For perfect contact specify a high value of conductance.

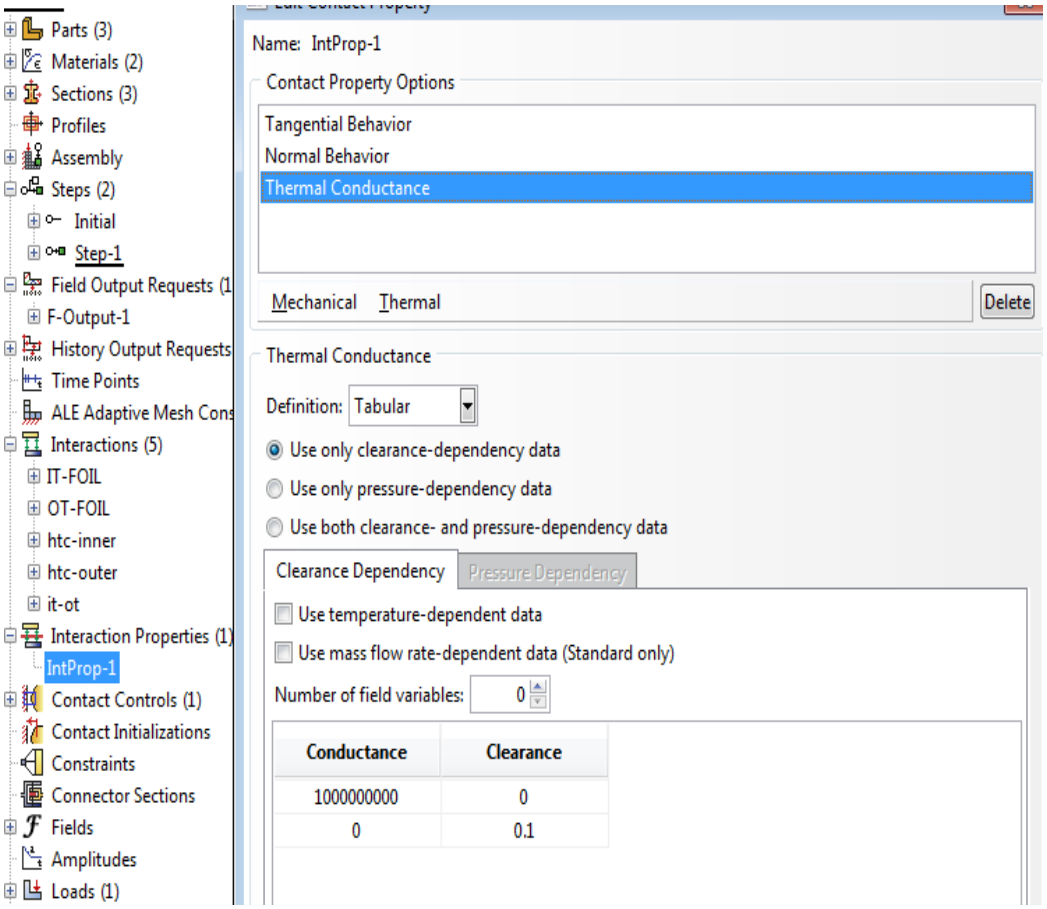

Figure 2.i. Thermal interaction properties

11. After the interaction properties have been created , the interactions can be specified. The contact interactions, specific of film conditions can be done in the interactions module. Click on contact controls in the main module and click on the ‘Stabilization ‘ tab and select ‘Automatic stabilization’ as in Fig 2.j..

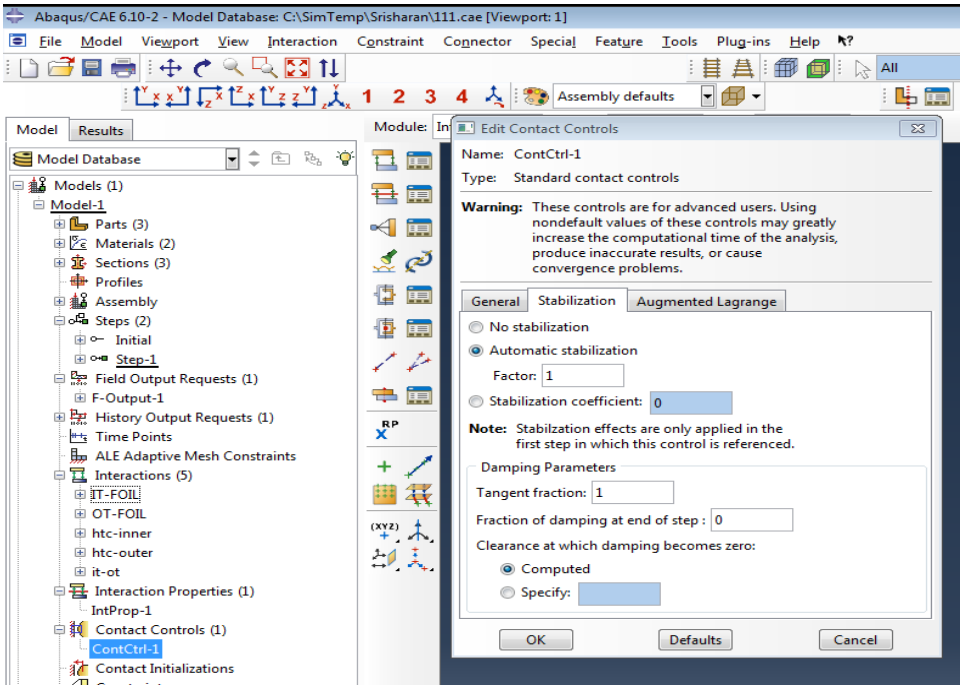

Figure 2.j. Specifying automatic contact controls

12. Now , click on ‘Interactions’ , name it ‘inner tube – foil ‘ and select ‘Surface-Surface contact’. Now select the master surface and the slave surface. The foil will be the master surface and the inner tube will be the slave surface. Select the ‘Finite sliding’ formulation and ‘Surface to Surface’ as the discretization method. Select the contact interaction property created in steps

    8-10 and the contact controls created earlier in this step. The advantage of using the automatic stabilization contact controls option is that it eases out any chattering issues resulting from contact. Another tip to ease out chattering issues and facilitate faster convergence is to use a ‘matched’ mesh. Repeat the same procedure to create another surface to surface interaction between the outer tube and the foil. The foil will be the master surface and the outer tube will be the slave surface. For the non-uniform

heating case another interaction will exist between the inner tube and the outer tube. The choice of the master and slave surface doesn't matter here. Use the same sliding formulation, discretization method, interaction property and contact controls as mentioned before. Thesesteps as illustrated in Fig 2.k will create the necessary contact between the foil and the tubes.

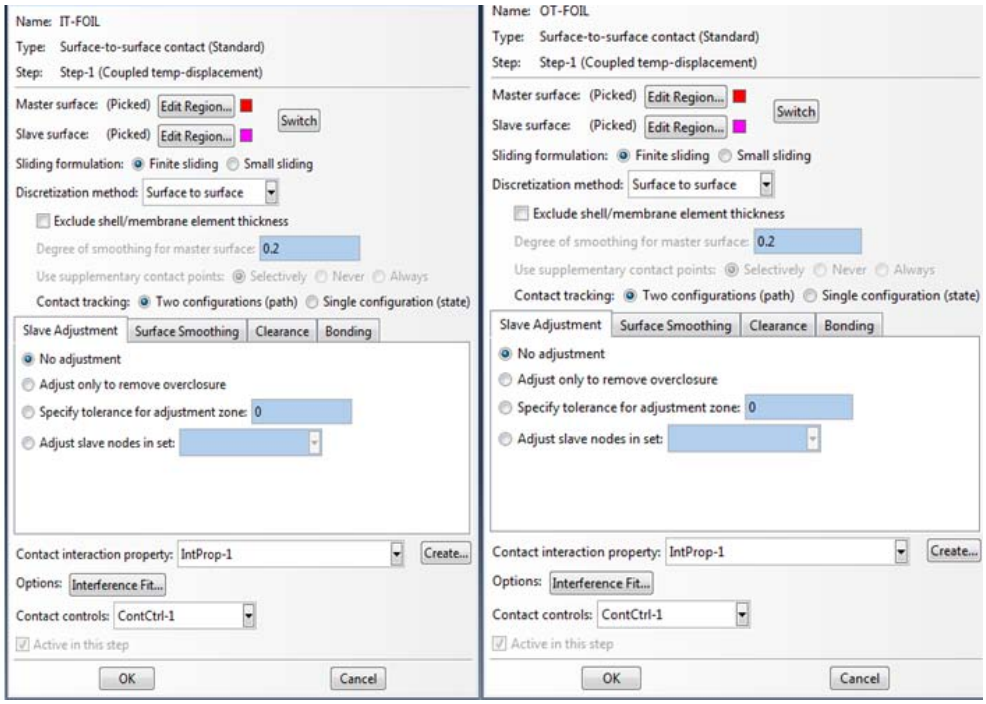

Figure 2.k. Specifying surface to surface contact interactions.

13. Next , specify the heat transfer coefficient by creating a 'Surface film condition interaction'. Do this once for the inner surface of the inner tube and outer surface of the outer tube. Enter the heat transfer coefficient of the surface and the coolant temperature . Steps 11 and 12 complete the specifications of the contact interactions.
14. Double click on 'Loads' and create a 'Body Heat Flux' 'Thermal Load' under the 'coupled temp displacement step'. Select the foil when asked to select the 'body' for

the load and specify the magnitude of heat generation and make sure the distribution is set to ‘Uniform’ and Amplitude to ‘Ramp’ as in Fig 2.l.

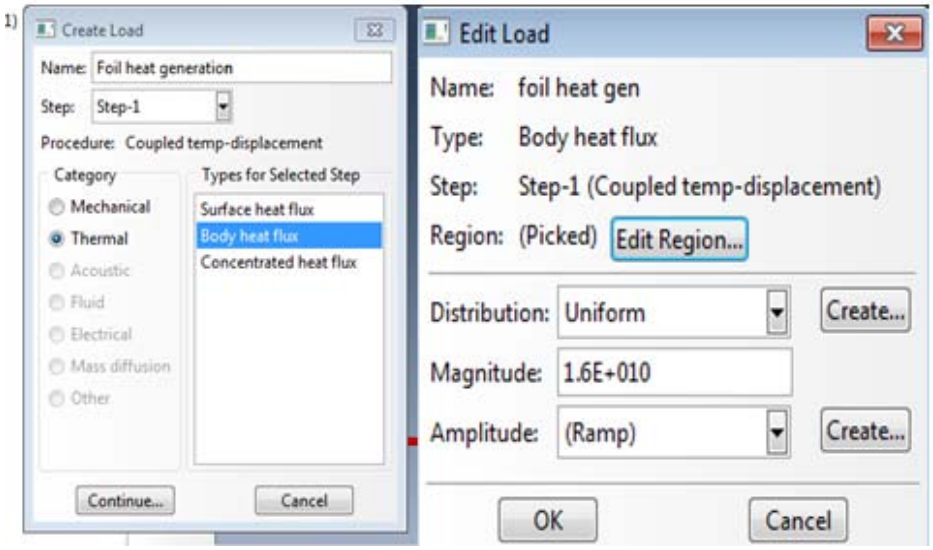

Figure 2.l. Creating the loads.

15. Specify an X-symmetric boundary condition, since the annular target with a recess is symmetric about the X-axis. Click on boundary conditions under the current analysis step and select ‘Symmetry/Antisymmetry/Encastre’ under the ‘Mechanical’ category. Now select ‘X-symm’ and select the nodes as highlighted in Fig 2.m. The X-symmetric boundary conditions restricts the translation of the nodes in the horizontal direction and prevents any rotation in the tangential direction. For the case of uniform selection an additional Y-symmetric boundary condition can be used by making a horizontal partition and selecting those nodes.

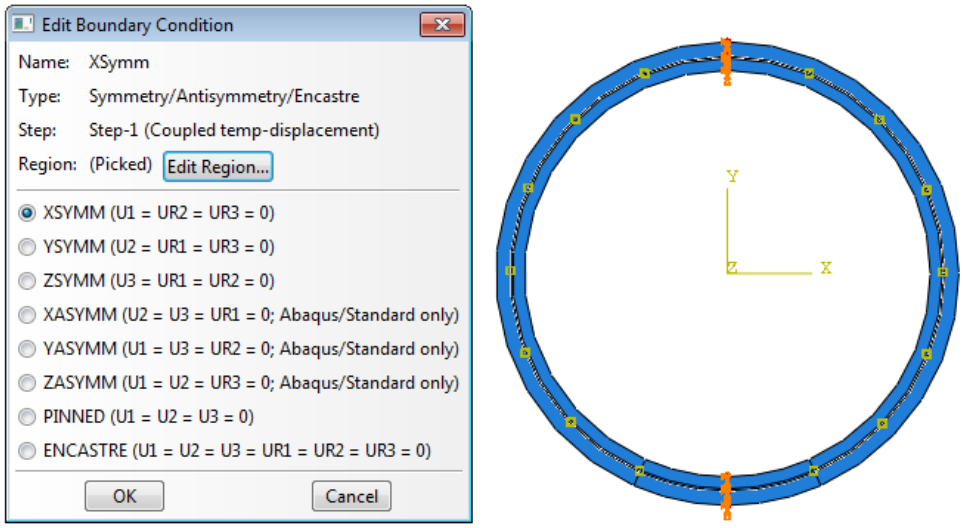

Figure 2.m. Creating the boundary conditions

16. Now the parts can be meshed. Click on one of the parts ,double click on ‘Mesh’. Now, click on ‘Seed’ in the main menu and click on edges and seed the edges by ‘number’ and click ‘Ok’. Now click on Mesh/Element Type. Select ‘standard’ under ‘Element Library’ and ‘Coupled Temperature Displacement’ under ‘Family’. Select a ‘quadratic’ geometric order and select ‘Reduced Integration ‘ and ‘Plan strain’ as the analysis type as shown in Fig 2.n. Click on OK. Repeat the same procedure for the other parts and to create a ‘matched’ mesh , ensure that the edge seeds are equal on all the parts. A matched mesh will improve the accuracy of the analysis , make radial data extraction across the assembly an easier task and facilitate faster convergence.

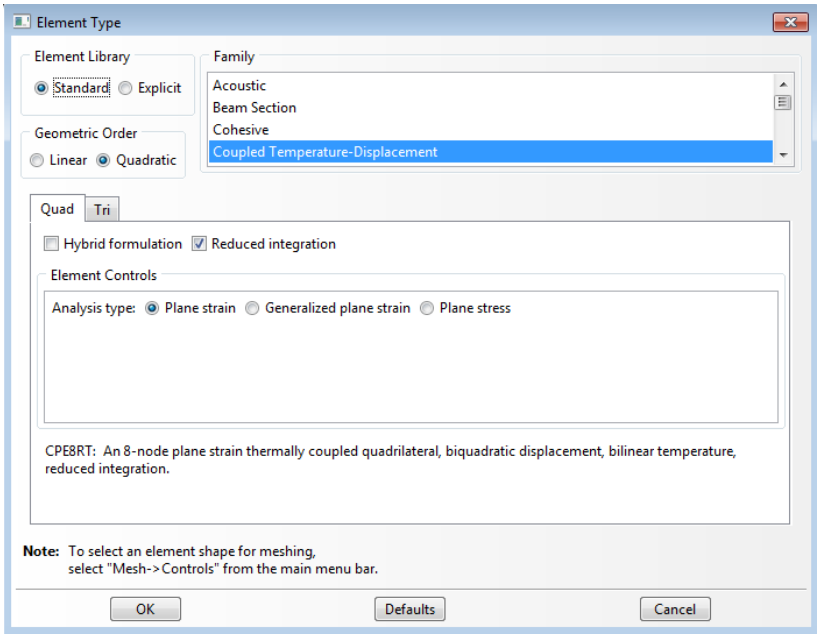

Figure 2.n Specifying the element type for meshing

17. The last step is to create the job for analysis. Click on the 'Analysis' tab in the model window and double click on 'Jobs'. Name the job and in the 'Edit Job' dialog box click on the 'Parallelization' tab to use multiple processors to run the analysis. Click on 'OK'. Now right click on the created job and select 'submit'. This submits the created job for analysis.

REFERENCES

Allen, C.W., Butler, R.A., Jarousse, C.A., Falgoux, J.L., 2007, "Feasibility Development Program, LEU Foil Plate Target for the Production of Molybdenum-99", *RERTR 2007 International Meeting, Prague, Czech Republic.*

Barber, J.R., Dundurs, J., Comninou, M., 1980, "Stability Considerations in Thermoelastic Contact ", *J.Appl.Mech* , Vol.47 , pp. 871-874 .

Boley, B.A., Weiner, J.H., 1960 , *Theory of Thermal Stresses* ,Dover Publications Inc., New York , NY , pp. 272-281.

Comninou, M., Dundurs, J., 1980 , "On Lack of Uniqueness in Heat Conduction through a Solid to Solid Contact " , *Journal of Heat Transfer*, Vol.102, pp. 319-323.

C. Conner, E. F. Lewandowski, J. L. Snelgrove, M. W. Liberatore, D. E. Walker, T. C. Wiencek, D. J. McGann, G. L. Hofman, and G. F. Vandegrift, "Development of annular targets for {sup 99}MO production.," *Proceedings of 1999 International Meeting on Reduced Enrichment for Research and Test Reactors*, Budapest, Hungary, 30 September 1999.

Fletcher, L.S., Miller, R.G., 1973 , " Thermal Conductance of Gasket Material for Spacecraft Joints", *AIAA Aerospace Sciences Meeting*, 11th, Washington, D.C .

Hsu, T.R., and Tam, W.K., 1979, "On Thermal Contact Resistance of Compound Cylinders ", *AIAA 14th Thermophysics Conf. Paper 79-1069.* American Institute of Aeronautics and Astronautics, New York.

Jane, K.C., Lee, Z.Y., 1999, “Thermoelasticity of Multilayered Cylinders” , *Journal of Thermal Stresses*, Vol.22, pp. 57-74.

Lemczyk, T.F., Yovanovich, M.M., 1987 , “New Models and Methodology for Predicting Thermal Contact Resistance in Compound Cylinders and Finned Tubes” , *Heat Transfer Engineering*, Vol.8, pp. 35-42.

Madhusudhana, C.V., Fletcher, L.S., 1981, “Thermal Conductance of Cylindrical Contacts” , *Proceedings of the eighth Canadian congress on applied mechanics* , New Brunswick , Canada. pp. 755-756.

Madhusudhana, C.V., Fletcher, L.S., 1981, “Solid Spot Thermal Conductance of Zircaloy-2/Uranium Dioxide Interfaces “ , *J.Nucl Sci Eng*, Vol 83 , pp. 327-332.

Madhusudhana, C.V., 1996, *Thermal Contact Conductance*, Springer , New York , NY , pp. 115-123.

Madhusudhana, C.V., 1999, “ Thermal Conductance of Cylindrical Joints” , *International Journal of Heat and Mass Transfer* , Vol 42 , pp. 1273-1287.

Matsumura, T.,Kogakuhakushi, M.E., “A Contribution to the Theory of Thermal Stresses in a Long Hollow Cylinder” , *Japan Society of Mechanical Engineers*.

Mikesell, R.P., and Scott, R.B., 1956, “Heat Conduction Through Insulating Supports in Very Low Temperature Equipment “, *J Res, US Natl Bureau Standards*, Vol.57, pp. 371-378.

Mikic , B.B., 1974 , “Thermal Contact Conductance : Theoretical Considerations “, *International Journal of Heat and Mass Transfer* , Vol. 17 , pp. 205-214.

Milosevic, N., Raynaud, M., Maglic, K., 2002, “Estimation of Thermal Contact Resistance Between the Materials of a Double Layer Sample Using the Laser Flash Method” , *Inverse Problems in Engineering* , Vol. 10 , pp. 85-103.

Mushtaq, A., Iqbal, M., Bokhari, I.H., Mahmood, T.,Mahmood, T., Ahmad, Z., Zaman, Q., 2008, “Neutronic and Thermal Hydraulic Analysis for Production of Fission Molybdenum-99 at Pakistan Research Reactor-1”, *Annals of Nuclear Energy*, Vol.35, pp. 345-352.

Mushtaq, A., Iqbal, M., Bokhari, I.H., Mahmood, T.,Mahmood, T., 2009, “Low Enriched Uranium Foil Plate Target for the Production of Fission Molybdenum-99 in Pakistan Research Reactor-1”, *Nuclear Instruments and Methods in Physics Research B*, Vol.267, pp. 1109-1114.

Mutalib, A., Purwadi, B., Adang, H.G., Hotman, L., Kadarisman, M., Sukmana, A., Sriyono., Suripto, A., Nasution,H., Amin, D.L., Basiran, A., Gogo, A., Sunaryadi, D., Taryo, T., Vendegrift, G.F., Hofman, G., Conner, C., Sedlet, J., Walker, D., Leonard, R.A., Wood, E.L., Wiencek, T.C., Snelgrove, J.L., “Full Scale Demonstration of the Cintichem Process for the Production of Molybdenum-99 using a Low Enriched Uranium Target “ , *International Meeting on Reduced Enrichment for Research and Test Reactors,* Sao Paulo, Brazil, 18-23 October 1998.

Novikov, I.I., Kokorev, L.S., Del’vin, N.N., 1972 ,”Experimental Heat Exchange Between Co-axial Cylinders in Vacuum” , *Atomnaya Energiya* , Vol.32 , pp. 474-475.

Poritsky, H., 1934 , “Analysis of Thermal Stresses in Sealed Cylinders and the Effect of Viscous Flow During Annealing” , *Physics,* Vol. 5 , pp. 406-411.

Ross, A.M. and Stoute, R.L., 1962, “Heat Transfer Coefficient Between UO2 and Zircaloy-2” ,*Atomic Energy of Canada, Ltd., Report CRFD-1075*, Ottawa, Ontario,Canada.

Seidlin, S.M., Marinelli, L.D., Oshry, E., 1946 , “Radioactive Iodine Therapy : Effect on Functioning Metastases of Adenocarcinoma of Thyroid” , *JAMA* , Vol.132 , pp. 838-847.

Scott, J., 2009, “Thermal Hydraulic Optimization for High Production of Low-Enriched Uranium Based Molybdenum-99”, *Master’s Thesis*, University of Missouri.

Solbrekken , G.L., Associate Professor of Mechanical Engineering , University of Missouri , Columbia , MO , “*Personal Communication”* , 2011.

Solbrekken, G. L., El-Gizawy, S., Allen, C., “Engineering design of LEU Foil Based Target for High Volume Production of Moly-99,” *International Meeting on Reduced Enrichment for Research and Test Reactors*, October 2008.

Srinivasan, M.G., France, D.M., 1985 , “Non-uniqueness in Steady-State Heat Transfer in prestressed Duplex Tubes-Analysis and Case History “, *J.Appl.Mech* , Vol.52 , pp. 257-262.

Swindeman, R.M, “Thermal Stresses in Hollow Cylinders of Beryllium Oxide “, *Oak Ridge National Lab Report* , ORNL-TM-24 , pp. 1-24.

Timoshenko, S., Goodier, J.N., 1951 , *Theory of Elasticity* , McGraw Hill Book Company , pp. 410-413.

Turner, KK., Solbrekken, G.L., Allen , C.W., “ Thermal-Mechanical Analysis of Annular Target Design For High Volume Production of Molybdenum-99 Using Low Enriched Uranium “, *Proceedings of the ASME International Mechanical Engineering Congress and Exposition* , IMECE 2009 , Lake Buena Vista , Florida , Nov 13-19 , 2009.

Turner, KK., Solbrekken, G.L., Allen , C.W., “ Thermal-Mechanical Analysis of Varying Boundary Conditions on a LEU Foil based Molybdenum-99 Plate Processing Target “,

Proceedings of the ASME International Mechanical Engineering Congress and Exposition , IMECE 2010, Vancouver, British Columbia, Canada, Nov 12-18 , 2010.

Turner, KK., Makarewicz, P.F., Govindarajan, S.G., Solbrekken, G.L., Allen, C.W., " Thermal Mechanical Development of an LEU Foil Based Target for the Production of MO-99 " , *European Research Reactor Conference*, RRFM, Rome, Italy, 20-24 March , 2011.

Ugural, A.C., Fenster, S.K., *Advanced Strength and Applied Elasticity*, Elsevier, New York, 1975 , pp. 255-256.

Xue, M., Zhang, X., Hu , N., 2006 , " Thermal Stress Analysis of Sandwich Structures " , *Journal of Thermal Stresses*, Vol.29 , pp. 229-244.

Yang, Y.C., Lee, H.L., 2001 , "Coupled Thermo-elasticity of an Infinitely Long Triple Layer Annular Cylinder ", *Journal of Thermal Stresses* , Vol.24 , pp. 779-798.

Yeoh, G., 2004, "*Consideration of U-foil/Aluminium wall gap of 30μm for engineering specification purposes*".

Zimmerman, R.W., Lutz, M.P., 1999, "Thermal Stresses and Thermal Expansion in a Uniformly Heated Functionally Graded Cylinder " , *Journal of Thermal Stresses* , Vol.22 , pp. 177-188.